Titre: Title:	In-Rim Antenna Systems for Portable Wireless Handsets
Auteur: Author:	Farhad Bin Ashraf
Date:	2022
Type:	Mémoire ou thèse / Dissertation or Thesis
Référence: Citation:	Ashraf, F. B. (2022). In-Rim Antenna Systems for Portable Wireless Handsets [Mémoire de maîtrise, Polytechnique Montréal]. PolyPublie. https://publications.polymtl.ca/10292/

URL de PolyPublie: PolyPublie URL:	https://publications.polymtl.ca/10292/
Directeurs de recherche: Advisors:	Mohammad S. Sharawi
Programme: Program:	Génie électrique

POLYTECHNIQUE MONTRÉAL

affiliée à l'Université de Montréal

In-rim antenna systems for portable wireless handsets

FARHAD BIN ASHRAF

Département de génie électrique

Mémoire présenté en vue de l'obtention du diplôme de *Maîtrise ès sciences appliquées*

Génie électrique

Avril 2022

POLYTECHNIQUE MONTRÉAL

affiliée à l'Université de Montréal

Ce mémoire intitulé :

In-rim antenna systems for portable wireless handsets

présenté par **Farhad Bin ASHRAF**

en vue de l'obtention du diplôme de *Maîtrise ès sciences appliquées*

a été dûment accepté par le jury d'examen constitué de :

Chahé NERGUIZIAN, président
Mohammad S. SHARAWI, membre et directeur de recherche
Jean-Jacques LAURIN, membre

DEDICATION

To my family

For their endless love, support, and encouragement

ACKNOWLEDGEMENTS

In the name of Allah, the most Beneficent and the most Merciful, Who has granted me the life and gave me the determination and opportunity to complete this research study.

I would like to express my sincere gratitude and indebtedness to my supervisor Professor Dr. Mohammad S. Sharawi for his excellent ideas, invaluable guidance, and constant support in making this research possible over the years. I would be delighted to thank him for his endless inspiration, kindness, friendly availability in spite of his busy schedule and allocation of his precious time for advising me during my research. I am deeply indebted to the Poly-Grames and Department of Electrical Engineering for providing the facilaties and working environment.

I would like to thank all my co-researchers and staffs of the Poly-Grames and Department of Electrical Engineering, Polytechnique Montreal, who helped me in many ways especially during my research work. My special appreciation is extended to all my friends and colleagues.

RÉSUMÉ

Dans les normes de communication sans fil modernes, les antennes à rebord métallique sont adoptées en raison de leur résistance mécanique et de leur aspect esthétique améliorés. Depuis qu'un grand écran avec un cadre étroit est devenu le courant dominant des smartphones, l'espace pour les antennes est très limité. Les réseaux d'antennes connectées (CAA) devraient fournir des bandes passantes plus larges, des niveaux de polarisation croisée plus faibles, de meilleurs gains et des tailles plus petites sur les jantes métalliques. CAA occupe également moins d'espace par rapport aux autres types d'antennes, permettant ainsi une plus grande intégration et des densités de réseau plus élevées. Un défi majeur dans de tels systèmes consiste à couvrir les bandes micro-ondes et mmWave introduites pour les normes sans fil de cinquième génération (5G) qui vont de 2 GHz à 38 GHz. La conception de systèmes d'antennes connectées dans la jante pour couvrir les fréquences inférieures à 6 GHz à 28 GHz est une tâche difficile en raison de la taille limitée des appareils portables sans fil. Par conséquent, une solution viable consiste à concevoir deux antennes pour deux bandes dans le même espace. Un concept d'antenne dans l'antenne (AiA) est mis en œuvre pour résoudre la limitation de taille et également couvrir les deux bandes dans la même structure d'antenne.

Dans ce travail, la conception d'un système d'antenne dans la jante utilisant CAA couvrant à la fois les bandes sous-6 GHz et mmWave avec une taille compacte avec quatre éléments est proposée. Le système d'antenne est une intégration entre une structure hyperfréquence et un réseau d'antennes à fentes connectées à ondes millimétriques mettant en œuvre le concept AiA. Des structures CAA à fente unique et en forme de cactus sont conçues pour couvrir les bandes de sous-6 GHz et 26~30 GHz et permettent les capacités de direction de faisceau. La structure d'antenne CAA unique présente une bande passante (S_{ij} < −10 dB) de 4,23 GHz (26,23–30,46 GHz) avec une efficacité totale de 86,1% et un gain réalisé de 8,94 dBi où les résultats de mesure présentent une bande passante (S_{ij} < −7,5 dB) de 6,42 GHz (25–31,42 GHz). Le faisceau peut être dirigé jusqu'à ±30o dans cette conception. La structure d'antenne cactus CSAA présente une bande passante (S_{ij} < -10 dB) de 3,27 GHz (26,64–29,91 GHz) avec une efficacité totale de 75,17% et un gain réalisé de 7,76 dBi à 28 GHz. En raison de la tolérance de fabrication, la réponse à deux ports est décalée vers une fréquence plus basse. Le faisceau peut être dirigé jusqu'à ±30o dans cette conception. Pour la bande micro-ondes, la bande passante (S_{11} < -10 dB) de 110 MHz (3,45–3,56 GHz) avec 4,69 dBi de gain

réalisé est atteinte. Après le réglage du prototype, il présente 350 GHz de bande passante résonnant à 3,69 GHz.

ABSTRACT

In modern wireless communication standards, metal rimmed antennas are adopted because of their enhanced mechanical strength and esthetic appearance. Since a large display with a narrow frame has become the mainstream of the smartphones, the space for antennas is very limited. Connected antenna arrays (CAA) are expected to provide wider bandwidths, lower cross-polarization levels, better gains, and smaller sizes on metal rims. CAA also occupy less space as compared to other antenna types, thus allowing for more integration and higher array densities. A major challenge in such systems is covering the microwave and mmWave bands introduced for fifth generation (5G) wireless standards that goes as low as 2 GHz to as high as 38 GHz. The design of in-rim connected antenna systems to cover sub-6 GHz to 28 GHz is a challenging task because of the limited size of wireless handheld devices. Therefore, a viable solution is to design two antennas for two bands in the same space. An antenna-in-antenna (AiA) concept is implemented to solve the size limitation and also cover both bands within the same antenna structure.

In this work, the design of an in-rim antenna system using CAA covering both the sub-6 GHz and mmWave bands with compact size along with four elements is proposed. The antenna system is an integration between a microwave structure and a mmWave connected slot antenna array implementing the AiA concept. A single and cactus shaped slot CAA structures are designed to cover the bands from sub-6 GHz and 26∼30 GHz and allow the beamsteering capabilities. The single CAA antenna structure exhibits bandwidth ($S_{ij} < -10$ dB) of 4.23 GHz (26.23–30.46 GHz) with a total efficiency of 86.1% and realized gain of 8.94 dBi where the measure results exhibit bandwidth (Sij < −7.5 dB) of 6.42 GHz (25–31.42 GHz). The beam can be steered up to ±30^o in this design. The cactus CSAA antenna structure exhibits bandwidth ($S_{ij} < -10$ dB) of 3.27 GHz (26.64–29.91 GHz) with total efficiency of 75.17% and the realized gain of 7.76 dBi at 28 GHz. Due to the fabrication tolerance two ports response is shifted to lower frequency. The beam can be steered up to ±30^o in this design. For the microwave band, the bandwidth ($S_{11} < -10$ dB) of 110 MHz (3.45–3.56 GHz) with 4.69 dBi of realized gain is achieved. After the tuning of the prototype, it exhibits 350 GHz of bandwidth resonating at 3.69 GHz.

TABLE OF CONTENTS

LIST OF TABLES

LIST OF FIGURES

LIST OF SYMBOLS AND ABBREVIATIONS

Ω	Ohm
1G	First Generation
2D	Two Dimensional
2G	Second Generation
3D	Three Dimensional
3G	Third Generation
3GPP	3rd Generation Partnership Project
4G	Fourth Generation
5G	Fifth Generation
AiA	Antenna-in-Antenna
BR	Backing Reflector
BW	Bandwidth
RFIC	Radio Frequency Integrated Circuit
CAA	Connected Antenna Array
CST	Computer Simulation Technology
CSAA	Connected Slot Antenna Array
CTIA	Cellular Telecommunications and Internet Association
DC	Direct Current
DCS	Digital Cellular System
ECC	Envelope Correlation Coefficient
et al.	(et alia): and Others
FCC	Federal Communication Committee
FDD	Frequency Division Duplexing

FET	Field-Effect Transistor
FM	Floquet Mode
FR	Frequency Range
FR4	Flame Resistant 4
GF	Green Function
GSM	Global System for Mobile
IC	Integrated Circuit
IEEE	Institute of Electrical and Electronics Engineers
IFA	Inverted-F Antenna
LCD	Liquid-Crystal Display
LTE	Long-Term Evolution
MEG	Mean Effective Gain
MEMS	Microelectromechanical Systems
MIMO	Multi-Input Multi-Output
NR	New Radio
PCS	Personal Communications Service
PCB	Printed Circuit Board
PEC	Perfect Electric Conductor
PIFA	Planar Inverted-F Antenna
PIN	Positive-Intrinsic-Negative
PMC	Perfect Magnetic Conductor
PNA	Performance Network Analyzer
RF	Radio Frequency
SAR	Specific Absorption Rate

SIW	Substrate-Integrated-Waveguide
SLL	Side Lobe Level
SNR	Signal-To-Noise Ratio
SPDT	Single Pole Double Throw
TEM	Transverse Electromagnetic
TDD	Time-Division Duplexing
UHB	Ultra-High Band
UMTS	Universal Mobile Telecommunication Systems
USB	Universal Serial Bus
Wi-Fi	Wireless Fidelity
WiMAX	Worldwide interoperability for Microwave Access
WLAN	Wireless Local Area Network

CHAPTER 1 INTRODUCTION

Due to the rapid development in wireless communication technologies and applications, there is growing demand for high-end mobile devices with many flagship features. Advanced mobile communication technology is urgently demanded to offer a higher throughput rate, shorter latency, and lower energy consumption for fifth generation (5G) mobile communications. 5G offers a new network architecture to help significantly boost overall performance compared to its fourth generation (4G) predecessor. 5G will deliver over 10 Gbps data rate, millisecond-level latency, and ultra-high-dense connections. Besides the ability to cover multi operations, there is now a general agreement that smartphone designs in the near future should include the sub-6 GHz and mm wave spectrum (such as those at 24–80 GHz) specifically designated for 5G new radio specification. The abundant spectrum available at these high frequencies supports higher data rates and capacity that will reshape the mobile experience. However, increased propagation loss, susceptibility to blockage (e.g., hand, head, body), and radio-frequency integrated circuit (RFIC) complexity and power-efficiency, has historically made these high-bands not feasible for mobile communications. Particularly, the volume reserved for all the antennas in a mobile device is very limited and the new mmWave antennas will require additional volume, which will make the mobile phone larger, bulkier, and thus less attractive to customers. The new mmWave antennas will be placed in the same volume, require significant changes in the design of the 4G sub-6 GHz antennas to avoid a major performance degradation. The integration of 5G multi-input multi-output (MIMO) antenna arrays into the smartphone can lead to superior capacity, high gain, and high data-rate transmission [1]. It is well known that the mobile users are now more concerned about the physical appearance of the mobile devices. Therefore, metal-rimmed smartphone designs have attracted much attention in recent years, because of their enhanced mechanical strength and aesthetic appearance without any additional volume for antennas.

Smartphone researchers and manufacturers face continuous challenges to support new RF standards and bands. The expanding requirements for multi-band coexistence and the smartphone design trends makes it more difficult. A standard 4G smartphone may need 4 to 8 antennas but the new 5G smartphones will need even more antennas to support all the frequency bands. Meanwhile, manufacturers cram new features like bigger batteries, additional cameras, facial recognition, and motion sensing into smartphones, which is eventually shrinking the space available for antennas in

5G smartphones. Design evolution like folding smartphones also reduce the space available for antennas since antennas cannot be placed in the hinge area.

To support the increasing higher data rates and capacity, 5G New Radio (NR) enables new higher-frequency, wide operational bandwidths of the order of GHz cellular spectrum. This spectrum is allocated into two frequency ranges by 3GPP [2]:

• Frequency Range 1 (FR1): These new ultra-high bands (UHB) (n77, n78, n79) use spectrum between 3.3 GHz and 5 GHz. n77 (3300-4200 MHz), n78 (3300-3800 MHz), and n79 (4400-5000 MHz).

• Frequency Range 2 (FR2): The first use of mmWave spectrum for commercial cellular communication. FR2 consist of several bands n257 (26.5–29.5 GHz), n258 GHz (24.25–27.5 GHz), n260 (37.0–40.0 GHz), and n261 (27.5–28.35 GHz).

The signal propagation is much more challenging at FR2 frequencies compared to FR1 frequencies. 5G smartphones with MIMO capability relatively use large antenna arrays to increase signal strength and beamforming. For FR1, the capacity enhancement is more essential due to the more interference limited environment. But for FR2 higher band, high gain antennas are more essential due to the more challenging propagation and path loss conditions.

In the 1980s, the wireless revolution increased the popularity of wireless device across the globe. 1G had no official requirements and the antenna specifications were simple. Phones typically had poor battery life and poor voice quality, large antenna size becoming the norm. Printed circuit antennas were commercially viable and implemented during the era of 2G mobile phones. During this time, large ground planes, variations of meandered printed lines with parasitic leads to dual band operation. As wireless standards evolved to 3G in early 2000s, the international committee laid out data rates to be supported by manufacturers and service providers. Printed multi-band antennas where the norm since carrier operating frequencies were geography dependent. On the edge of 2010, 4G experienced phenomenal data growth and huge market success because of features like video streaming, video calling, and online gaming services. MIMO was developed and implemented in this phase with multiple printed multiband antennas were integrated into the mobile device. Their design challenges increase as these antennas had to coexist with other tightly spaced antennas for Bluetooth, Wi-Fi. Future 5G antennas can be phased arrays, Slot antenna arrays

at 28 GHz and higher along with MIMO configurations. MmWave 5G antenna design is still an active research area with much potential for design improvements. Table 1.1 is an overview of the cellular evolution from an antenna perspective [3].

Table 1.1 Cellular Technologies and Their Antennas

Generation	Carrier Frequency	Type of Antenna
1G	800 MHz	Helical/Telescopic
2G	900 MHz/1800 MHz	Printed Dual Band
3G	2100 MHz	Printed Multi-Band
4G	850 MHz/1800 MHz	Printed Multi-Band with MIMO
5G	Sub-6 GHz, 28 GHz	Phased Array, Slot arrays with MIMO

Connected antenna arrays (CAAs) can also be a potential candidate for 5G smartphone antenna design. CAAs are expected to provide wider bandwidths, lower cross-polarization levels, better gains, and smaller sizes on metal rim. In CAA, the array of dipoles and/or slots are connected electrically so that they will act like a single antenna rather than multiple antenna elements. They provide wideband characteristics as the connections between adjacent elements yields constant currents [4]. CAA will also occupy less space as compared to other antenna types, thus allowing for more integration and higher array densities. The metal-rimmed CAA based MIMO antenna arrays will be the first approach without any vertical cut on meta-rim and expected to cover the 28 GHz mm-wave bandwidths.

1.1 Motivation

Historically, we observe wireless standards evolve every decade. With the changing trends and exponentially increasing mobile users this transition may or may not continue in the future. The uncertainty of 5G and its large demands force both manufacturers and researchers to redesign the hardware and network structural design, where previous generations had similar carrier frequencies. The migrations for the early generations were minimal compared to the proposed

migration from 4G to 5G. The use of wireless smartphone devices has increased tremendously in recent years. According to Cisco's projections [5], over 70 percent of the global population will have mobile connectivity. By 2023, the total number of global mobile subscribers will grow from 5.1 billion (66 percent of population) in 2018 to 5.7 billion (71 percent of population). 5G devices and connections will be over 10 percent of global mobile devices and connections, global mobile devices will grow to 13.1 billion where 1.4 billion of those will be 5G capable. The average 5G connection speed will reach 575 Mbps. It is predicted that North America will have 329 million mobile users (88 percent of regional population by 2023. It is forecasted that 5G will enable $13.2 trillion of global economic output in 2035 The global 5G value chain will generate $3.6 trillion in economic output and support 22.3 million jobs in 2035, which is a significant share compared to other sectors [6].

Most smartphone users nowadays use applications like video streaming, online gaming and video calling which are bandwidth hungry. To meet the needs of this massive explosion of data consumption, innovative antenna designs are essential in the hardware design and cellular network layout. Leading companies such as Samsung, Qualcomm, Ericsson, Verizon, Nokia Siemens networks, NTT Docomo, IBM and Huawei have established dedicated 5G research groups to develop the 5G standardization process. Qualcomm announced their QTM527, a fully-integrated high-power mmWave antenna module with 800 MHz bandwidth and 2x2 MIMO. With the mobile screen becoming more and more large, it is a great challenge for researchers to design a multi-band or broadband antenna in a small space. Moreover, foldable smartphones are nowadays become more popular because of its appearance and will lead the market in near future. Thus, the design of an antenna system that support both sub-6 GHz and mmWave GHz along with space as well as efficient band utilization are becoming a necessity within mobile phones according to the 5G wireless standards. This work will come up with multi-band in-rim based slot antennas for 5G mobile terminals.

1.2 Objectives

The proposed work is aimed to achieve three main objectives.

1. To design slot antenna arrays based on the concept of CAA on a smartphone metal rim that can provide frequency coverage in the bands between 2-6 GHz (microwave) and 26-31 GHz (mm-wave) frequency bands.

2. To design and investigate the concept of Antenna-in-Antenna (AiA) where the microwave antenna (larger size) can be embedded with the mmWave antenna (smaller size) for more efficient and smaller size structures.

3. To investigate the beam steering capability of the metal-rimmed CAA based antenna system with better connectivity at mm-wave bands.

1.3 Methodology

To accomplish the objectives, the project started with a survey of state-of-the-art methods for metal-rimmed antenna, connected antenna array (CAA) concept, actual impacts on real-time measurement system. The theoretical aspects of CAA are conquered through the re-derivation of the governing equations utilizing the spectral Green's function for both infinite and finite array cases. Then the solution is applied on finite connected slot-based arrays, the slots are placed along the metal-rim to make it unbroken. Efficient numerical procedures and models are used and devised to characterize the edge effects in the array due to its finite size.

Two antennas are incorporated in the same space by exploring the Antenna in Antenna (AiA) concept. The solution is covering the sub-6 GHz frequency bands as well as the mm-wave bands (26-31 GHz). The design is based on a slot-based CAA for sub-6GHz and mm-wave array.

In the next stage, several numerical tools in addition to electromagnetic modelling software's are used. A comparative analysis of the array is conducted for finding the best-integrated array solution in the cases of meta-rimmed scenarios for various locations. The analytical results are verified by modelling the arrays in full-wave simulators like CST Microwave Studio in terms of input impedance, current distribution, efficiency, and radiation patterns.

A beam-forming method is integrated with the feeding network that can tilt the beam directions based on the phases of the feeding lines. An active based feed network solution utilizing mm-wave programmable phase shifters is used for the investigation. The Cactus structure is used to minimize the physical size of such a 5G antenna system. The combined CAA, with its AiA concept will bring a novel practical solution to all future wireless device antenna systems with its beam steering capability.

The final prototypes are fabricated and measured at the facilities of Poly-Grames Laboratories. Finally, with the best metal-rimmed CAA configuration for a dual band scenario is investigated and devised via simulations and prototyping to devise the first-ever endeavor metal-rimmed CAA antenna array for the microwave and mm-wave bands.

The flow chart in Figure 1.1 shows the overall steps that will be conducted during the research.

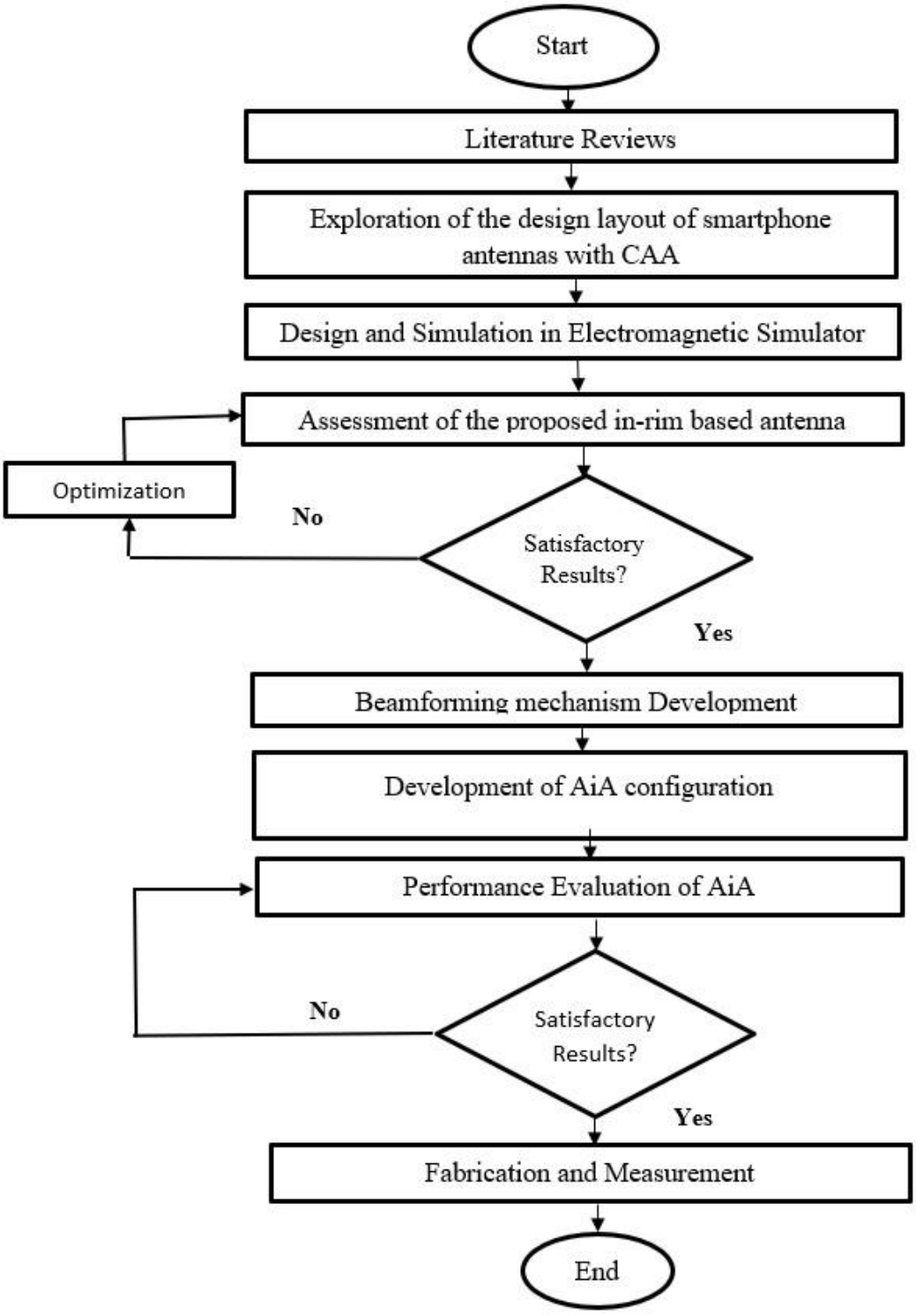

Figure 1.1 Flow chart of work methodology

CHAPTER 2 BACKGROUND

This chapter presents the theoretical formulation of antenna arrays. The formulation of linear and planar arrays, whereas only final equations are given. The amplitude tapering for array scenario are also discussed. The background of connected antenna arrays (CAAs) and the generalization of the infinite periodic array of connected slots is then discussed and leads to analytical formulas for the active input impedance of a single long slot array element. After that, the 2-D long slot array in free space and with backing reflector is discussed. Then the scanning properties of connected array are investigated. The scan performance of this arrays is governed by the array sampling, and the distance from the ground plane. Finally, the finite array considerations and series feeding are discussed.

2.1 Antenna Arrays

The radiation pattern of a single element is relatively wide and provides low values of directivity (gain). In mobile communication, it is necessary to design antennas with very directive characteristics i.e., very high gains, in mmWave where penetration and path losses is very high. An antenna array is a group of similar elements that are spaced in a regular manner. To provide very directive patterns, it turns out that the fields from each element of the array added constructively. To shape the overall pattern of the antenna, we have several things to adjust:

1. The number of antennas
2. The placement of the antennas
3. The amplitude of the signal applied to each antenna
4. The phase of the signal applied to each antenna

If we consider two infinitesimal horizontal dipoles positioned along the z-axis by distance ***d***, ***k*** is wavenumber and the total field radiated by the two elements is given by [7]

$$E_t = \hat{a}_\theta j\eta \frac{kI_o le^{-jkr}}{4\pi r} \sin\theta \left\{ 2\cos\left[\frac{1}{2}\left(kd\cos\theta + \beta \right) \right] \right\} \tag{2.1}$$

the array factor of two-element array of constant amplitude is given by [7]

$$AF = 2\cos\left[\frac{1}{2}\left(kd\cos\theta + \beta \right) \right] \tag{2.2}$$

By varying the separation ***d*** and/or the phase ***β*** between the elements, the characteristics of the array factor and total field of the array can be controlled.

Now we generalize the method for N-elements in z direction. Let us assume an array of identical elements along z-axis, which has equal magnitude and each with a progressive phase is referred to as a uniform array. The array factor is given by [7]

$$AF = \sum_{n=1}^{N} e^{j(n-1)\psi} \qquad (2.3)$$
$$where, \psi = kd\cos\theta + \beta$$

If we want to scan the maximum radiation at a certain angle θ_o, the phase excitation ***β*** between the elements have to be adjusted such that

$$\beta = -kd\cos\theta_o \qquad (2.4)$$

The maximum directivity of linear broad side array can be approximate to

$$D_o = 2N\left(\frac{d}{\lambda}\right) \qquad (2.5)$$

Now we will consider broadside arrays with uniform spacing but nonuniform amplitude distribution. Three main excitations which are uniform, binomial, and Tschebyschef will be discussed. Uniform amplitude arrays give the lowest half-power beamwidth followed by the Dolph-Tschebyscheff and binomial arrays. On the other hand, binomial arrays give the lowest side lobes followed by the Dolph-Tschebyscheff and uniform arrays. Designers has to tradeoff between side lobe level and beamwidth. Uniform arrays usually provide the largest directivity.

A major practical disadvantage of binomial arrays is the wide variations between the amplitudes of the different elements of an array. Particularly, when the number of elements is large. This leads to very low efficiencies for the feed network and makes it undesirable in practice. For example, the relative amplitude coefficient of the end side elements of a 4-linear array is 1 while that of the center elements is 3 which is 3 times more than the two side end elements. It would be difficult to obtain and maintain such large amplitude variations among the elements. They would also lead to very inefficient antenna systems.

To solve this problem, we can use the Dolph-Tschebyscheff array. The Dolph-Tschebyscheff array is mainly a compromise between uniform and binomial arrays. The order of the polynomial should be one less than the total number of elements of the array.

Linear arrays have some limitations, they can scan only in the plane of elements center. In planar arrays, designers have additional variables to control and shape the pattern of the array. They are used for applications requiring a pencil beam, and high gain. more versatile and can provide more symmetrical patterns with lower side lobes. Furthermore, they can scan the main beam of the antenna towards any point both $\boldsymbol{\theta}$ and $\boldsymbol{\varphi}$ plane in space. If we place **M** elements along the x-axis at a distance $\boldsymbol{d_x}$ and if we place **N** elements along the y-axis at a distance $\boldsymbol{d_y}$ then the array factor for the entire plane will be [7]

$$AF = \sum_{n=1}^{N} \mathrm{I}_{1n}\, e^{j(n-1)\left(kd_y \sin\theta \sin\phi + \beta_y\right)} \left[\sum_{m=1}^{M} \mathrm{I}_{m1}\, e^{j(m-1)\left(kd_x \sin\theta \cos\phi + \beta_x\right)} \right] \tag{2.6}$$

where, $\mathbf{I}_{m1}$ and $\mathbf{I}_{1n}$ are the excitation coefficient of each element in *x, y* directions.

When the spacing between the elements is equal or greater than λ/2, multiple maxima of equal magnitude can be formed. To avoid grating lobes, the spacing between the elements must be less than λ/2. The phases $\boldsymbol{\beta_x}$ and $\boldsymbol{\beta_y}$ are independent of each other and if we need only one beam along $\boldsymbol{\theta}$ and $\boldsymbol{\varphi}$ then the phase can be represented as [7]

$$\begin{aligned} \beta_x &= -kd_x \sin\theta_o \cos\phi_o \\ \beta_y &= -kd_y \sin\theta_o \sin\phi_o \end{aligned} \tag{2.7}$$

The maximum directivity of planar array can be approximate to

$$D_o = \frac{4\pi}{\lambda^2} A_p = 4\pi N_x \frac{d_x}{\lambda} N_y \frac{d_y}{\lambda} \tag{2.8}$$

2.2 Connected Antenna Array (CAA)

An array of 2 or more antennas which are electrically connected is called a connected antenna array (CAA). In this type of arrays, high mutual coupling is a drawback and there is a trend to make it as small as possible because high mutual coupling can lead to narrow bandwidth and low efficiency. CAAs were invented by Baum in 1970 [8]. He used TEM horn antennas for such a configuration. He mentioned that it is a timed array radiating a short pulse along the array in an end-fire direction. Figure 2.1 shows the TEM horn antenna CAA.

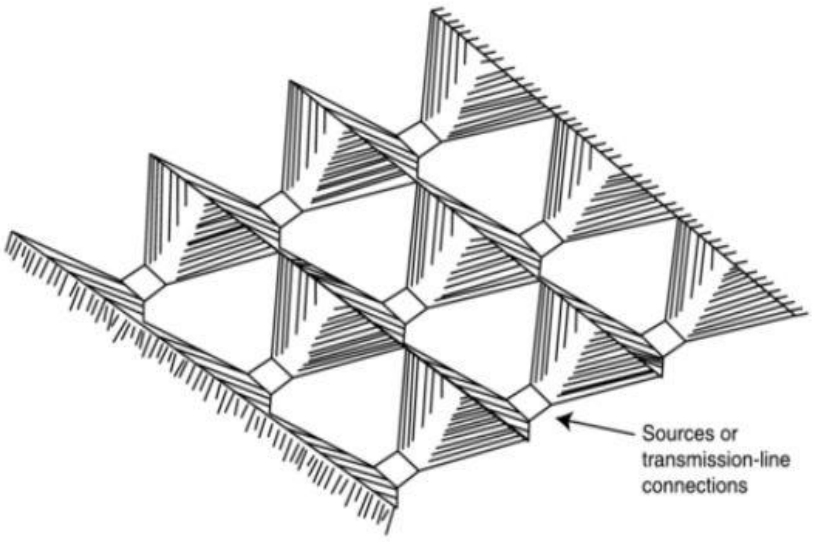

Figure 2.1 Connected antenna array of TEM horn antenna [8]

In 1979, Inagaki invented the self-complimentary antenna. Figure 2.2 shows a bowtie type linear CAA. Inagaki showed that the input impedance of this antenna is $60\pi\ \Omega$ which is one half of the free space impedance [8].

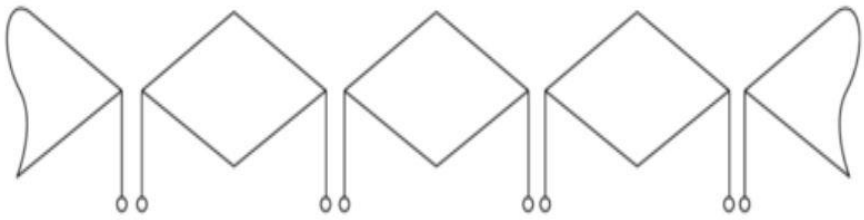

Figure 2.2 Linear connected antenna array [8]

In CAA, the array of dipoles and/or slots are connected electrically so that they will act like a single antenna rather than multiple antenna elements. They provide wideband characteristics as the connections between adjacent elements yields nearly constant currents where narrow-band unconnected dipoles are sinusoidal and frequency dependent as shown in Figure 2.3 (a), (b) [9].

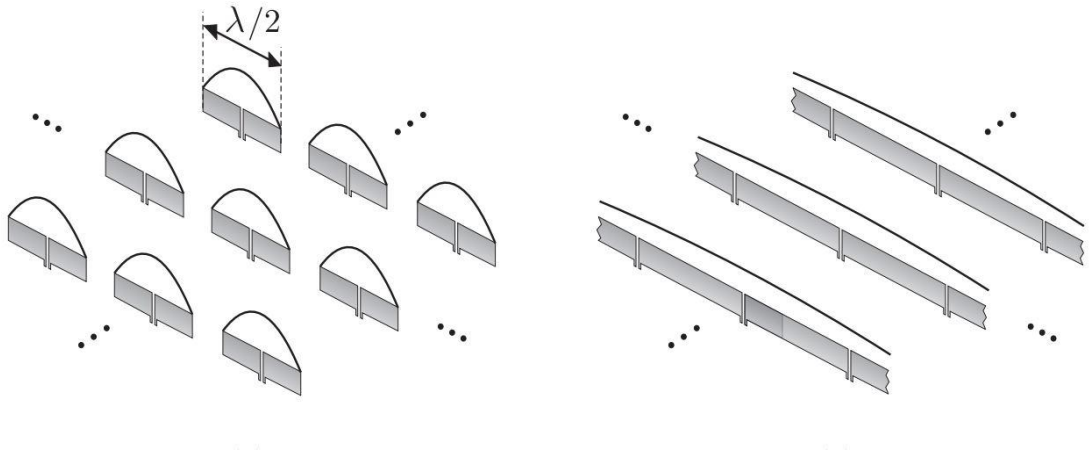

(a) (b)

Figure 2.3 Current distribution on dipole elements in array configuration (a) unconnected dipoles and (b) connected dipoles [9]

By connecting the dipoles, depending on the feeds spacing the current curves illustrates like Figure 2.4. For each of the dipoles, it is apparent that the current is near zero at the ends with peaks in the middle can be seen in Figure 2.4 (a). When the dipoles are connected, and the feeds with λ/2 spacing at broadside exhibits a surprising current distribution. Over the entire wire every other dipole has very small current as in Figure 2.4 (b), the current peaks are one wavelength apart. When twice the number of feeds is used with λ/4 spacing, current distribution is significantly changed, as in Figure 2.4 (c). Now, each dipole has a roughly sinusoidal distribution, and the dips are modest. This phenomenon will help to get wide bandwidth [8].

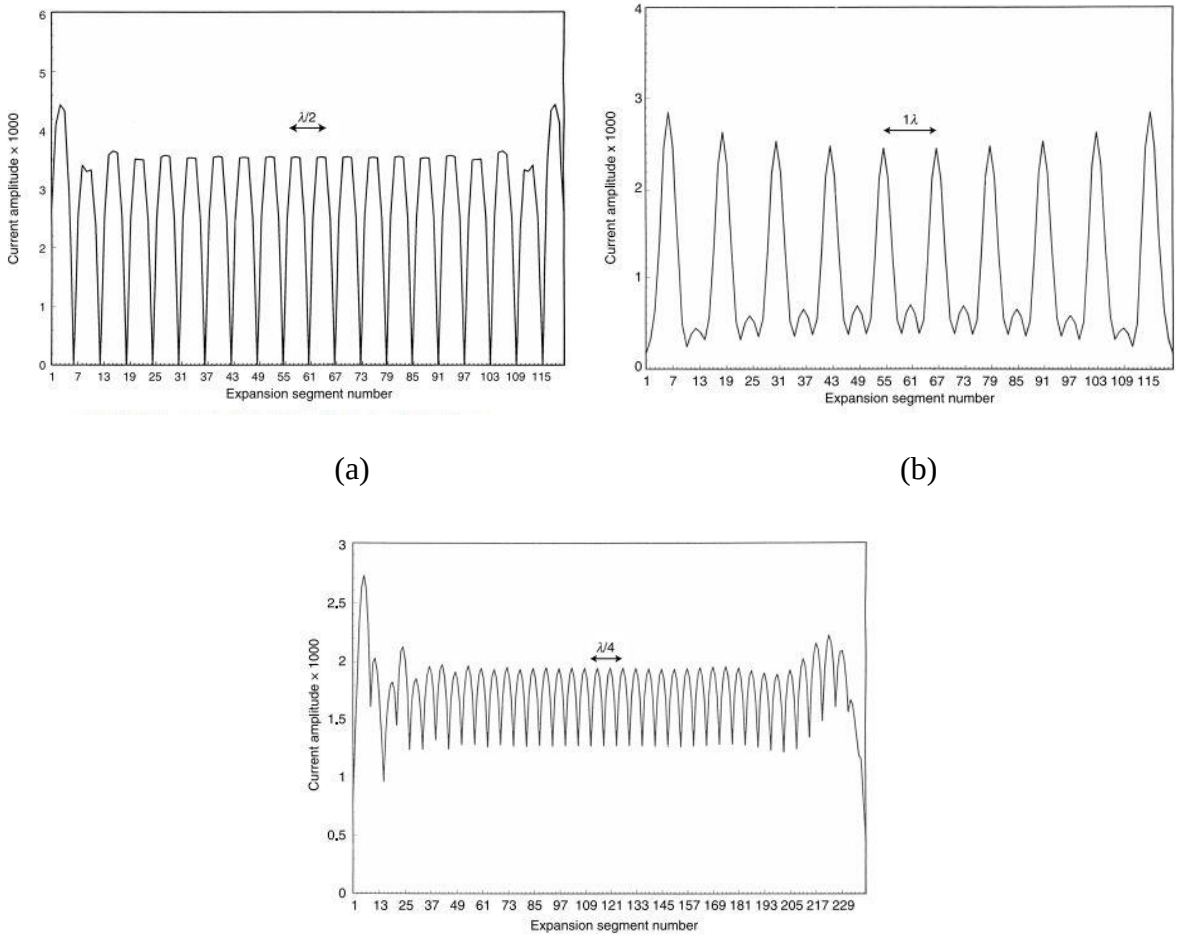

Figure 2.4 Current amplitude for different feed spacing of CAA (a) λ/2 Dipole array, (b) feed with λ/2 spacing, and (c) feed with λ/4 spacing [8]

CAA will also occupy less space as compared to other antenna types, thus allowing for more integration and higher array densities. Another attractive feature of CAA is their capability to achieve good polarization purity, in virtue of the planarity of the radiating currents.

2.3 Single long slot with multiple feed elements

An infinitely long slot fed by a single delta source is shown in Figure 2.5 (a) and an equivalent unknown surface current distribution in Figure 2.5 (b), where the slot is replaced by an equivalent magnetic current distribution $\boldsymbol{m_s(x,y)}$. A functional separability dependence of $\boldsymbol{m_s(x,y)}$ along the transverse (across the slot) and longitudinal is assumed, i.e., $\boldsymbol{m_s(x,y) = v(x).m_t(y)}$. The transverse y-dependence of the magnetic current is required to satisfy the quasistatic edge-singularities. The voltage across the slot can be represented as [11]

$$v(x) = \frac{1}{2\pi}\int_{-\infty}^{\infty} \frac{I_e(k_x)}{D(k_x)} e^{-jk_x x} dk_x \tag{2.9}$$

where, I_e represents the Fourier transform (FT) of impressed distribution along $\boldsymbol{x}$ and $\boldsymbol{D}$ is given by the convolution between the Green's function in absence of the slot and the transverse magnetic current distribution and expressed in the spectral domain.

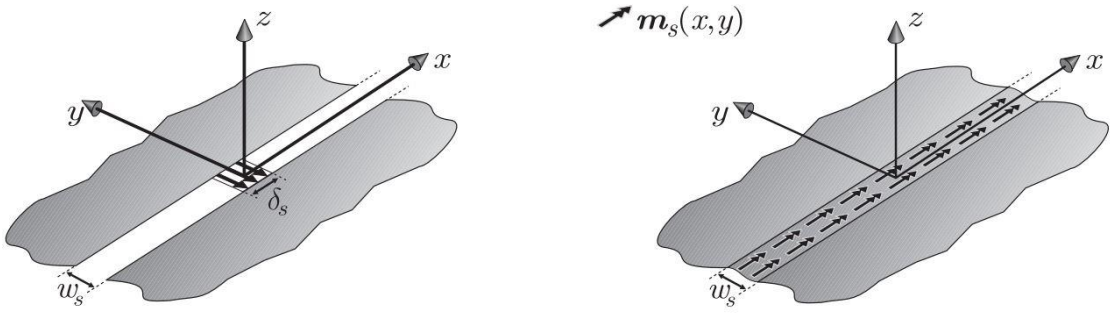

(a) (b)

Figure 2.5 (a) Infinite long slot in free space excited by a delta source; (b) equivalent unknown surface current distribution [9]

Now let us consider a single long slot excited by multiple feed elements as shown in Figure 2.6. This single long slot can be seen as a linear array of connected magnetic dipoles and by duality theorem it acts like a linear array of connected electric dipoles [8]. The results can be derived with an analogous procedure using the spectral Green's function (GF) applicable to the electric dipoles in free space as in [10]. The derivation of the Green's function of an infinitely long slot fed by a

single delta source is summarized in [11]. Here they derived the GF of a single slot in free space, between two different dielectrics and in the presence of a backing reflector. In the case of single long slot induced by a finite or infinite number of impressed electric currents ($\boldsymbol{I_e}$), the expansion of the periodic current source ($\boldsymbol{n_x}$) (array factor) is now summed by N number of sources for finite case and are infinite for infinite case, in equations 2.10 and 2.11 respectively. Here, $\boldsymbol{k_x}$ represents the wave number in *x*-direction.

$$I_e\left(k_x\right) = I_o \sin c\left(k_x t/2\right) \sum_{n_x=-N/2}^{N/2} i\left(n_x\right) e^{jk_x n_x d_x} \tag{2.10}$$

$$I_e\left(k_x\right) = \frac{2\pi}{d_x} \sum_{m_x=-\infty}^{\infty} \delta\left(k_x - k_{xm}\right) \tag{2.11}$$

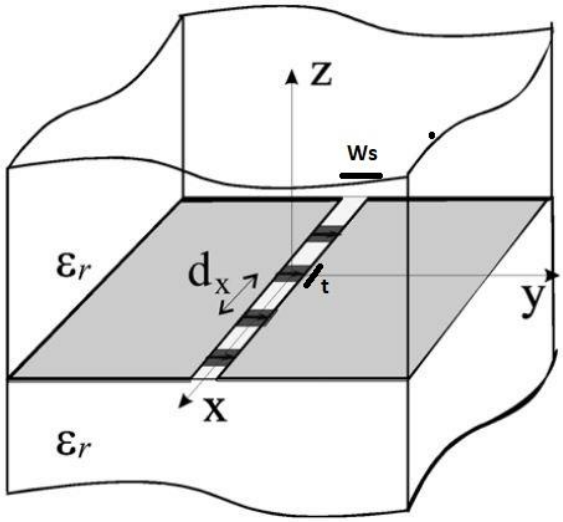

Figure 2.6 A single long slot with multiple feed elements [11]

The magnetic current distribution in free space by an infinite array of current sources ($\boldsymbol{m_x}$) can be derived by using equation (2.11) in (2.9) derived in [11]

$$v_o\left(x\right) = \frac{K_o \zeta_o}{d_x} \sum_{m_x=-\infty}^{\infty} \frac{I_o \sin c\left(k_{xm} t/2\right) e^{-jk_{xm}x}}{\left(k_o{}^2 - k_{xm}{}^2\right) J_o\left(k_{zm}\frac{w_s}{4}\right) H_o{}^2\left(k_{zm}\frac{w_s}{4}\right)} \tag{2.12}$$

$where, k_{zm} = \sqrt{k_o^{\,2} - k_{xm}^{\,2}}$ and J_o and H_o^2 is the zero-th order Bessel and Hankel functions, respectively.

The magnetic currents are continuous on the entire slot and as a result the mutual coupling between the feeds is high.

From the real and imaginary parts of the voltage we can evaluate the active input impedance. It is defined by the ratio between the voltage across the slot and the unit current at each feed point when they are all excited. the final expression is given by [11]

$$z_{in} = \frac{K_o \zeta_o}{d_x} \sum_{m_x=-\infty}^{\infty} \frac{\sin c^2\left(k_{xm} t/2\right)}{k_{zm}^{\,2} J_o\left(k_{zm}\frac{w_s}{4}\right) H_o^{\,2}\left(k_{zm}\frac{w_s}{4}\right)} \tag{2.13}$$

By introducing an ideal transmission line of characteristic impedance ($\boldsymbol{z_l}$) equal to the impedance of the slot at resonance one can calculate its reflection coefficient.

$$|\Gamma| = \frac{z_{in} - z_l}{z_{in} + z_l} \tag{2.14}$$

For low frequency approximation, considering the dominant mode, $\boldsymbol{m_x}$=0 [11].

$$z_{in} \approx \frac{K_o \zeta_o}{d_x} \frac{\sin c^2\left(k_{xo} t/2\right)}{k_{zo}^{\,2} J_o\left(k_{zo}\frac{w_s}{4}\right) H_o^{\,2}\left(k_{zo}\frac{w_s}{4}\right)} \tag{2.15}$$

2.4 2-D long slot array

A single long slot with multiple feeds presents large value of input impedance at lower frequency. This drawback can be resolved by 2-D long slots array (Figure 2.7). In a 2-D long slot array, the slots are now placed in both x and y axis and practically has infinite bandwidth. They combine coherently in a given direction to create a plane wave which in free space are characterized by impedances that are constant with respect to frequency. Now the contribution from the y axis will add up in the magnetic current $\boldsymbol{m_s}$ and the spectral function $\boldsymbol{D}$. The mathematical formulations are in [11].

2.4.1 2-D long slot array in free space

The active impedance of a 2-D long slot array is given by [11]

$$z_{in\infty}^{fs} = \frac{d_y}{d_x}\frac{K_o\zeta_o}{2}\sum_{m_x=-\infty}^{\infty}\frac{\sin c^2\left(k_{xm}t/2\right)}{\left(k_o{}^2 - k_{xm}{}^2\right)\sum_{m_y=-\infty}^{\infty}\frac{J_o\left(k_{ym}\frac{w_s}{2}\right)}{k_{zm}}} \qquad (2.16)$$

$$where, k_{zm} = \sqrt{k_o{}^2 - k_{xm}{}^2 - k_{ym}{}^2}$$

the difference here with respect to equation (2.13) is that the Hankel function is substituted with a summation of Floquet Mode (FM) like terms. All FM's are actually plane waves.

2.4.2 2-D long slot array with backing reflector

By placing a backing reflector, the waves radiated in lower half space can be redirected in the upper half space originally presented in [12]. The active impedance is given by

$$z_{in\infty}^{br} = \frac{K_o\zeta_o d_y}{d_x}\sum_{m_x=-\infty}^{\infty}\frac{\sin c^2\left(k_{xm}t/2\right)}{\left(k_o{}^2 - k_{xm}{}^2\right)\sum_{m_y=-\infty}^{\infty}\frac{J_o\left(k_{ym}\frac{w_s}{2}\right)\left(1-j\cot\left(k_{zm}h\right)\right)}{k_{zm}}} \qquad (2.17)$$

2.5 Scanning performance of backed connected arrays

The scan performance of Connected antenna arrays is governed by two number of factors [9],

a. The array sampling (***d**x* and ***d**y*).
b. The distance from the ground plane (***h***).

The slot arrays under consideration are shown in Figure 2.7 together with the relevant reference system and characterizing parameters.

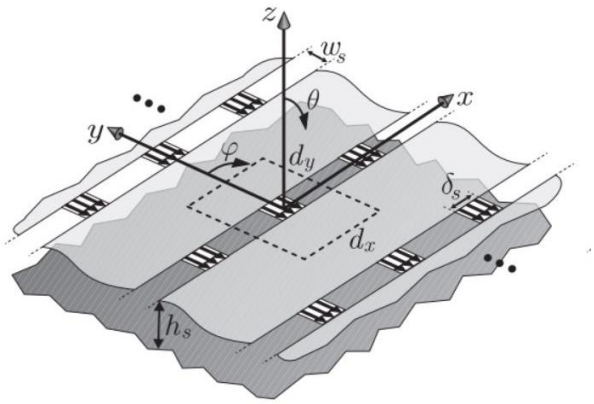

Figure 2.7 2D periodic connected array of slots with backing reflector [9]

the active input impedance with backing reflector of an array element is expressed in equation (2.17)

$$where, k_{xm} = k_o \sin\theta_o \cos\phi_o - \frac{2\pi m_x}{d_x}, k_{ym} = k_o \sin\theta_o \sin\phi_o - \frac{2\pi m_y}{d_y}, k_{zm} = \sqrt{k_o{}^2 - k_{xm}{}^2 - k_{ym}{}^2}$$

By considering only the first mode ($\boldsymbol{m_x} = \boldsymbol{m_y} = 0$) (low frequency), the equation (2.17) becomes,

$$\mathbf{z}_{in\infty}^{br}\Big|_{m_x=m_y=0} = \frac{\zeta_o d_y}{d_x} \frac{\cos\theta}{\left(1-\sin^2\theta\cos^2\varphi\right)\left(1-j\cot\left(k_o h\cos\theta\right)\right)} \qquad (2.18)$$

for broadside radiation ($h = \lambda/4$), the resonance of the impedance is given by the condition $k_o h\cos\theta = \pi/2$. Under this condition, if we assume a square periodic cell ($\boldsymbol{d_x} = \boldsymbol{d_y}$), the impedance will be $z_{in\infty}^{br} = \zeta_o$. The active impedance is twice as large as the asymptotic value for low frequency of a connected array of slots without backing reflector ($\zeta_o/2$).

The array scanning gives two important effects [9].

1. The input resistance is increased by a factor of sec θ when scanning in the E-plane and dropped by a factor of cos θ when scanning in the H-plane.
2. The matching of the arrays as a function of the scanning results from the shift of the resonance frequency. As the scan angle grows, for example to 45º, the electrical length ($k_0 h \cos\theta$) becomes smaller, and the resonance shifted 40% higher with respect to broadside as shown in Figure 2.8(b).

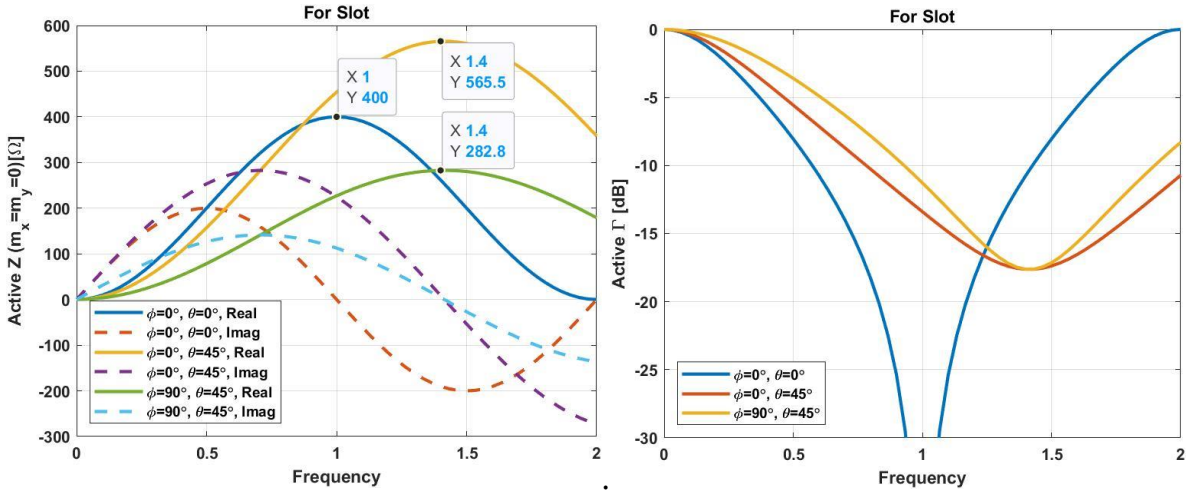

(a) (b)

Figure 2.8 (a) active impedance and (b) active reflection coefficient, with respect to 400Ω transmission line when dx=dy=0.4 λ and h=0.25 λ

2.5.1 Array sampling

The array is sampled to $\boldsymbol{d_x}$=0.5 λ, $\boldsymbol{d_y}$=0.4 λ and $\boldsymbol{h}$=0.25 λ. Form Figure 2.9(a), the input resistance of the connected arrays for Broadside (φ=0º and θ=0º) direction is now decreased to 320Ω. The same phenomena have been observed when scanning in the E-plane (φ=0º and θ=45º), H-plane (φ=90º and θ=45º) compared to Figure 2.8. Form Figure 2.9(b), It is observed that the resonant frequency of the active reflection coefficient shifted 40% to higher frequency when scanning in the E-plane and H-plane compared to the Broadside. But here the active reflection coefficient of E-plane increases, and active reflection coefficient of H-plane decreases as $\boldsymbol{d_x}$ is changed. The bandwidth (>-10dB) is decreased and is around 30%.

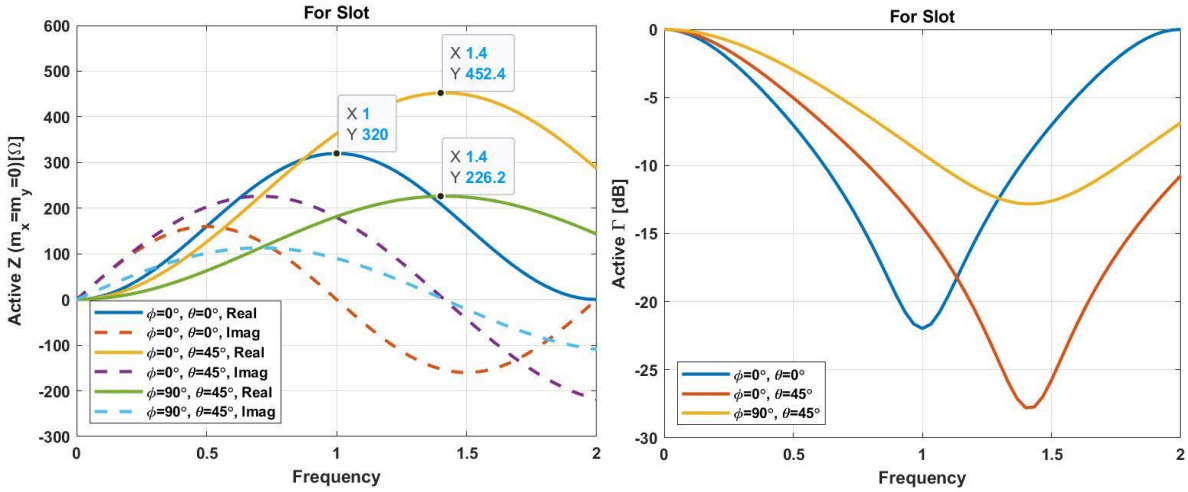

(a) (b)

Figure 2.9 (a) active impedance and (b) active reflection coefficient, with respect to 320**Ω** transmission line when dx=0.5 λ, dy=0.4 λ and h=0.25 λ

Now the array is sampled to $\boldsymbol{d_x}$=0.4 λ, $\boldsymbol{d_y}$=0.5 λ and $\boldsymbol{h}$=0.25 λ. Form Figure 2.10(a), the input resistance of the connected arrays for Broadside (φ=0^o and θ=0^o) direction is now increased to 500Ω. The same phenomena have been observed compared to Figure 2.9. Form Figure 2.10(b), the resonant frequency of the active reflection coefficient shifted 40% to higher frequency when scanning in the E-plane and H-plane compared to the Broadside. But here the active reflection coefficient of E-plane and H-plane both improved by the change of $\boldsymbol{d_y}$. The bandwidth (>-10dB) shows an improvement and is around 56%. The summary of the analysis has been listed in Table 2.1. From equation (2.18) we can observe that if $\boldsymbol{d_x}$ increases, impedance will decrease as it is in the denominator and if $\boldsymbol{d_y}$ increases, impedance will increase as it is in the nominator as in Table 2.1.

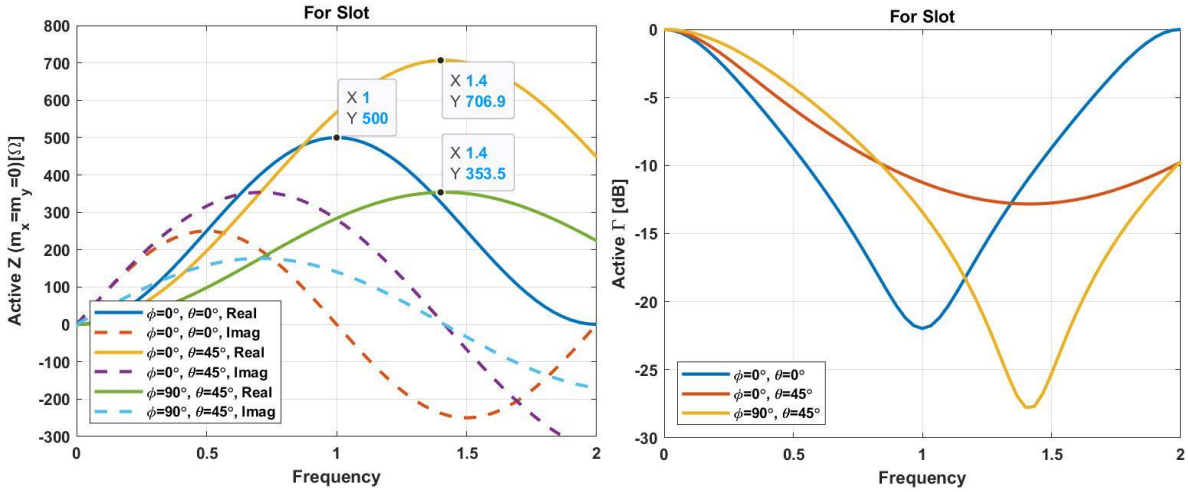

(a) (b)

Figure 2.10 (a) active impedance and (b) active reflection coefficient, with respect to 500Ω transmission line when dx=0.4 λ, dy=0.5 λ and h=0.25 λ

Table 2.1 Summary of the array sampling effects when scanning

	Active Resistance (Ω)	**Bandwidth (>-10dB)**
	d*$_x$**=0.4 λ, ***d*$_y$**=0.4 λ and ***h=0.25 λ	
Broadside	400	~47%
E-plane	565.5	
H-plane	282.8	
	d*$_x$**=0.5 λ, ***d*$_y$**=0.4 λ and ***h=0.25 λ	
Broadside	320	~30%
E-plane	452.4	
H-plane	226.2	
	d*$_x$**=0.4 λ, ***d*$_y$**=0.5 λ and ***h=0.25λ	
Broadside	500	~56%
E-plane	706.9	
H-plane	353.5	

2.5.2 Distance from the ground plane

Connected arrays of slots backed by reflector (Figure 2.7) at a distance ***h*** can support leaky waves. This ***h*** can influence the position and the nature of the poles occurring from the longitudinal dispersion equation in [9]. These leaky wave poles are linked with waves propagating along the array. When the backing reflector is placed away from the radiating slots, the propagating mode of the slot is quasi-TEM, travelling almost parallel to the slot direction. The mode field distributions are increasingly affected when ***h*** becomes smaller. Therefore, the poles pose an increasingly larger imaginary part and smaller real part. from Figure 2.11, for smaller ***h***, the resonances are shifted toward higher frequencies and will narrow the useful band when scanning in the E-plane.

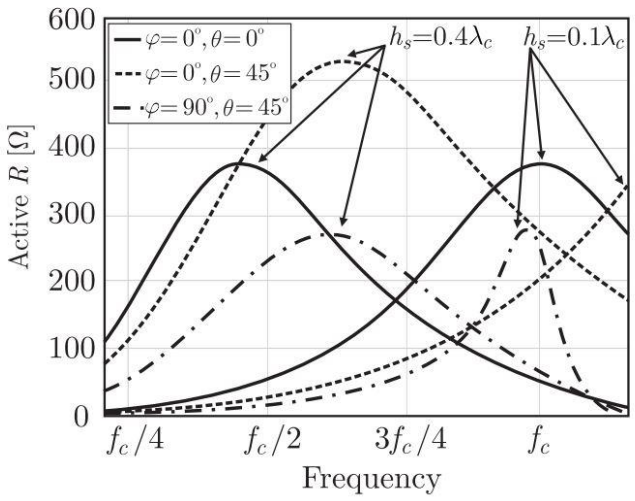

Figure 2.11 Active resistance of a connected slot array for h=0.4λ and 0.1λ [9]

2.6 Finite Array considerations

Until now we discussed the infinite array consideration, however when finiteness is considered the impact of edge effects can dominate the array performance designed for wide bandwidth. High mutual coupling between the elements in wideband arrays facilitates the propagation of edge-born waves. The connections of connected arrays allow currents to remain nearly constant, these connection supports guided waves and can be very strong at the edge of the array. As a result, the overall performance of the finite array can be significantly different with respect to the infinite array analysis. In [9], extensive analysis of finite array has been done. At first, he derived the full

GF formalism for infinite-array current and then the edge current. The currents are considered as the superposition of infinite array and edge-born waves. The intensity of the edge-born wave can be reduced by the source/load impedances.

2.7 Conclusion

In this chapter, the theoretical background of antenna arrays is discussed. For linear arrays, the uniform and nonuniform excitation is discussed. Uniform amplitude arrays give the lowest half-power beamwidth followed by the Dolph-Tschebyscheff and binomial arrays. On the other hand, binomial arrays give the lowest side lobes followed by the Dolph-Tschebyscheff and uniform arrays. The problem with the binomial can be solved by the Dolph-Tschebyscheff array. Uniform arrays usually provide the largest directivity. Later, the array factor of planar case is shown. The connected antenna array concept and how it achieves wideband performances is also discussed. The 2-D long slot array with and without backing reflector and its scanning performance are shown. Finally, finite array consideration is discussed.

CHAPTER 3 LITERATURE SURVEY

The transition from the current 4G mobile network to the 5G is already in development and expected to be fully developed within the next decade. Many developed countries like USA, Canada, China, European Union, and South Korea have initiated extensive research propelled by its enduring demand for superior speed and capacity to launch 5G wireless technology in the coming years. Both sub-6 GHz and mmWave have been preferred for 5G development, but mmWave have been gaining much attention from governments, industry, and academia. The Federal Communication Committee (FCC) announced high-band spectrum a priority, up to 11 GHz of spectrum above 24 GHz for high-band and more than 600 MHz of spectrum in sub-6 GHz for mid-band [14]. This announcement gives much-needed clarity for 5G research and development.

This chapter will cover the literature review for antenna systems for portable wireless handsets. This will be followed by the reconfigurable and feeding techniques and, consequently, the effects of components for mobile antennas. At last, co-location of both microwave and mmWave antennas and Antenna in Antenna concept will be discussed.

3.1 Metal rimmed antennas for handsets

The physical appearance of the headsets is now more important for headset users, and they are concerned about the physical appearance of the phone. Therefore, metal-rimmed handset design gained much attention in recent years from both the academic and industrial sectors, because of its enhanced mechanical strength and esthetic appearance. Because of that, the integration of antennas into a metal-rimmed handset is rigorous and creates a big challenge during the design environment, not to mention if multiband antennas along with beamsteering capabilities are required.

The use of metal-rimmed antennas as slots have been used in mobile antennas to achieve multiband operation [15,17,21,23,25]. In [15], a large metal ground and an unbroken metal rim was used (see Figure 3.1) to achieve multiband operations as 4G (820–960 and 1710–2690 MHz) and 5G (3400–3600 MHz). They used Taconic RF-30 substrate with relative permittivity of 3.0 and loss tangent of 0.0014 with a board size of 150×74×1 mm^3. A multiband antenna was presented in [16] which includes the effects of the metal ring. It covers multiple bands including the GSM (890–960 MHz), DCS (1710–1880 MHz), PCS (1850–1990 MHz), UMTS (1920–2170 MHz), and some LTE bands

(FDD-LTE band 1–6, 8–10 and TDD-LTE band 19, 20, 33–37). In [17], a reconfigurable open slot antenna was proposed to cover a wide bandwidth of 698–960 and 1710–2690 MHz for 4G smartphone applications. Here they used a 0.8 mm thick FR4 substrate with a relative permittivity of 4.4 and a loss tangent of 0.02 and the system circuit board size was same as [15]. The surrounded metal rim was 7 mm of height and 1 mm thick copper. A low-profile 2× 2 MIMO antenna for LTE low 699–960 MHz mid and high 1710–2690 MHz band was presented for real-life metallic smartphone platforms [18]. The antenna was on the longitudinal edges of the ground plane and the metal rim was utilized to devise a reconfigurable coupled loop antenna topology. The overall size of the main circuit board is 148×68×1 mm^3 and FR4 was used. The height and thickness of the metal rim was 5 and 1 mm, respectively. In [19], a planar folded monopole, surrounded by L-shaped metal rim extended ground stubs was proposed, they achieved multiple resonances consisting of 1.6 to 3.6 and 4.1 to 6.1 GHz.

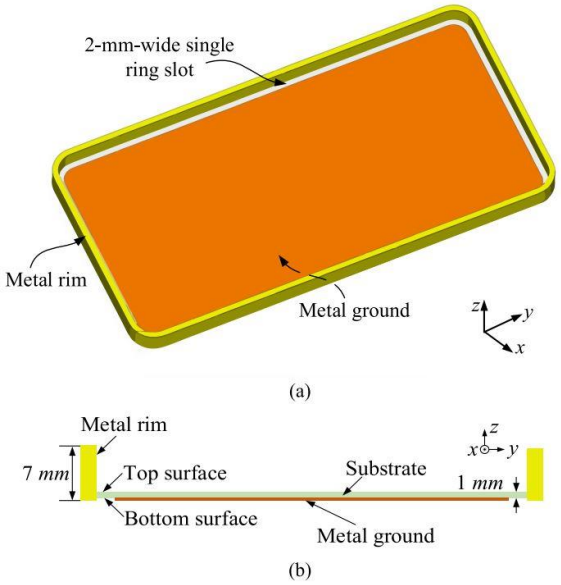

Figure 3.1 Metal-rimmed handset (a) 3-D view and (b) Side view [15]

In [20], a two set beam steering arrays on each side of a metallic casing having eight elements was studied. The design achieved approximately 27.5–30 GHz measured 10 dB return loss bandwidth in the mmWave band. In [21], a combination of bow-tie array and slot array was presented as endfire mm-wave array to cover the n258 (24.25–27.5 GHz) and n261 (27.5–28.35 GHz) 5G mmWave bands and it is embedded in the handset metal frame. Choi at el. [22] proposed a 1×4

PFSA subarray with a multi throw topology demonstrated frequency adjustment from 27.95 to 28.65 GHz. PFSA features a 2.6-time enhanced impedance bandwidth and an average peak gain of 6.3 dBi. Dual-polarized end-fire chain slot antenna array was reported in [23] across the entire band from 24.5 to 29.5 GHz. Another dual polarized end-fire antenna for mobile devices was shown in [24, 25]. In [25], a dipole antenna operated at mm-wave band (23 to 29 GHz) through a 20×3.5 mm2 window were proposed. The proposed multi-layer substrate. A reflector was placed at a distance of $\lambda/4$ for maximum directivity of the antenna elements. The peak realized gain was reported 6 dBi. It has a beam-steering capability up to $\pm 40^{o}$ using three-element array. Other dual function antenna that are in the literature will be discussed in the integrated microwave and mmWave section (3.6).

A complete analysis of the effects of an unbroken metal rim on the performance of a handset was presented in [16]. Here, they showed some undesired coupling because of unbroken metal rim (as they are in close proximity of internal antenna) can downgrade the antenna performances. They also had induced current which exhibits their own resonances. So, authors came with an equivalent circuit model for metal rim and guides it to act as an external antenna for handset. To overcome the effects of metal rims some other antenna designs was proposed in [26, 27]. In which the authors of [26] applied the characteristic modes theory to investigate the property of the metal rim.

3.2 Types of antennas

During the development of modern mobile communication, variety of antennas for handset applications was proposed during the past two decades. The classification of types of antennas used in handset is Slot, Loop, PIFA, Bowtie/Quasi-Yagi, Monopole, Dipole and Vivaldi. Some of them are briefly discussed here. Similar types of antennas are ignored because of brevity.

A single ring slot-based antenna for 4G/5G metal rimmed smartphone was proposed in [15]. They used grounded stub via shorting pin to create slots (opening in between the ground stubs) and loops (creates on the edges of the board from the feed to the ground stubs) in the ground plane as in Figure 3.2. A 2 mm wide single slot was etched out from the edge of the ground plane then by properly optimizing the grounded stubs they generate multiple resonant modes. Two loops and three slots were designed for 4G as in Figure 3.2(a) and four element MIMO slot antennas were designed for 5G bands, fig 3.2(b).

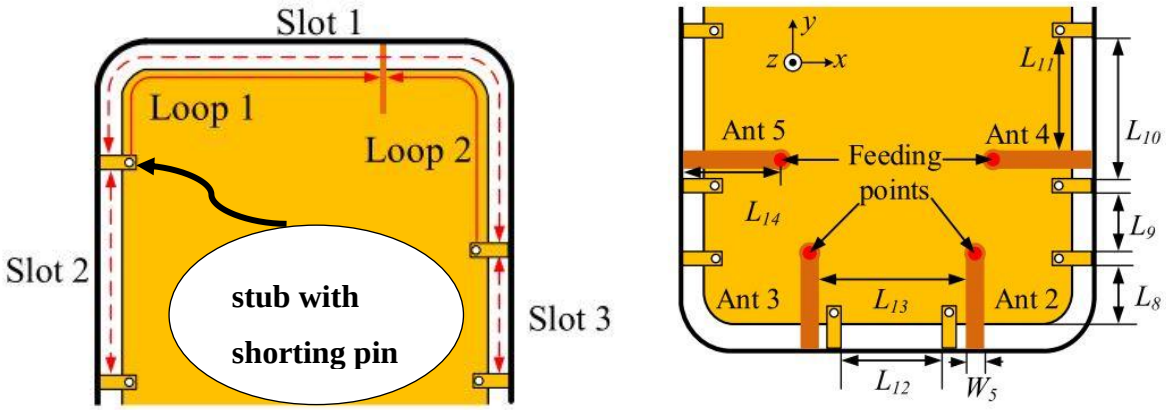

(a) (b)

Figure 3.2 Loop and slot antenna for (a) 4G and (b) 5G [15]

The internal antenna used in [16] was composed of two folded inverted-L monopoles and one ground arm on a plastic carrier with around 80% total efficiency as in Figure 3.3, a popular choice of mobile antenna system.

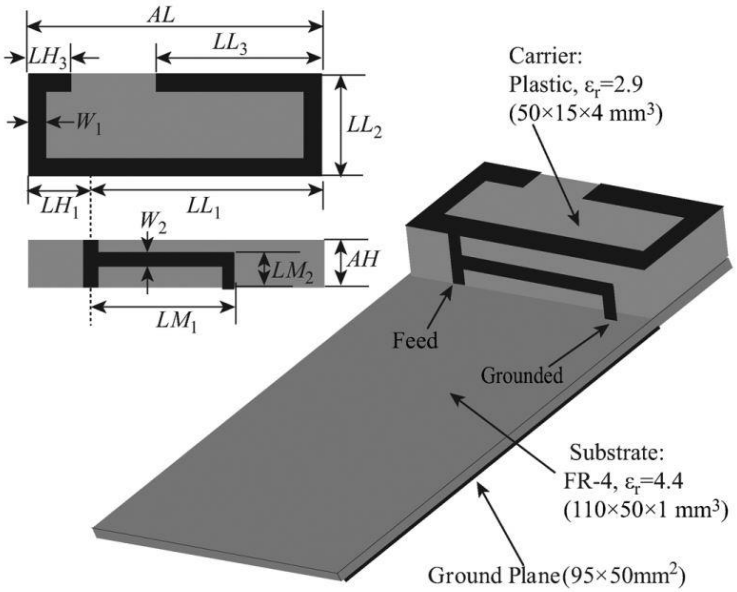

Figure 3.3 Inverted L-monopoles antenna [16]

In [17], a novel reconfigurable open slot antenna was proposed with a minimum of 50% efficiency in the desired bands. A coupled loop antenna design was proposed in [18] for the 4G application

in a 2 × 2 MIMO system as in Figure 3.4. The antenna was placed at the right and left long side edges of the main circuit board. At the front surface of the board the ground plane was printed, and the antenna had a vertical metallic arm. two sets of identical antennas were implemented, where in antenna 1, part of the metal rim was connected to the feeding strip through a chip capacitor. For antenna 2, part of the metal rim was used by implementing a LC matching circuit.

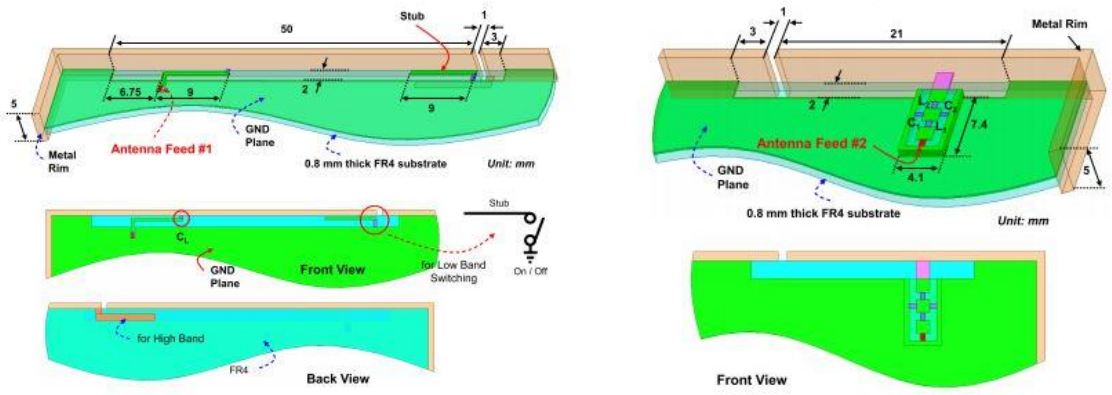

Figure 3.4 Integrated coupled loop 2×2 MIMO antenna [18]

Two-set of arrays with eight elements on each side of a metallic casing was shown in [20]. Here, each array element was a cavity-backed slot type, and the eight-element phased array was fabricated on the metallic back casing of the handset. For wider scanning angle, the slots were filled with low-loss polycarbonate ($\varepsilon_r = 3$). In [21], microwave and mmWave phased array using bowtie and sot antenna was used but they suffer some degradation in antenna performance because the antenna they used is actually used for sub-3 GHz antenna. To overcome this, they suggested vertical slots in the metal chassis of the phone and got 1.2 dBi more gain as in Figure3.5. This slots in the rim also solve their blockage radiation problem for the bowtie antenna. The volume covered by the antenna was 21.7×7.75×0.64 mm^3 on a Rogers RO4350B substrate of thickness 0.254 mm and dielectric permittivity of 3.48. The total efficiency of the mmWave array was 92%. For the beamsteering they used two set of combination one was 2 active elements and the other one was 4 active elements.

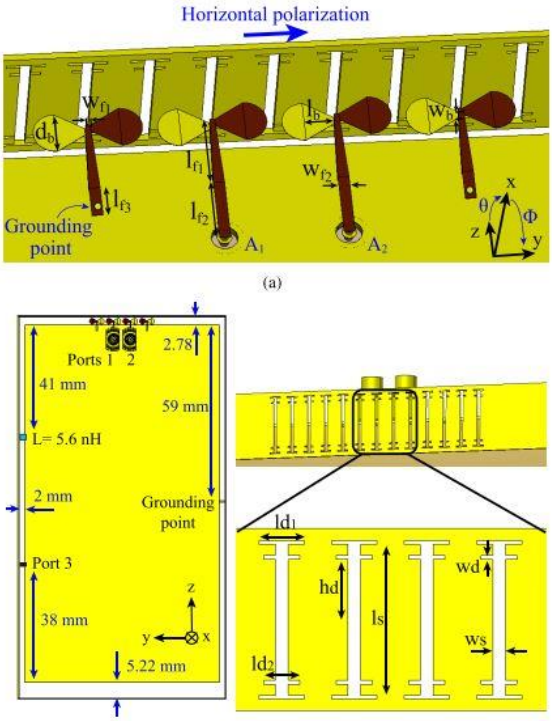

Figure 3.5 mmWave phased array consist of bowtie and slot [21]

In [23], a 4-element chain slot array was placed within a mobile rim. The reported realized gain was between 8 and 12.6 dBi for both polarizations and the total efficiency of a single element is better than −2 and −3 dB across the entire band. They used a back-reflector behind the slot to direct energy outwards. A dual-function slot antenna operated at both microwave and mm-wave band was proposed in [28]. Their design consists of a slot printed on the edge of the ground plane. The designed slot has dual functionality, it works as a tunable slot antenna at 4G microwave band and operates as a wideband antenna array at 5G mmWave band using the principle of CAA.

A compact building block composed of a slot antenna and a loop antenna was proposed in [29]. Although the slot and the loop overlapped completely, it exhibits better than 19 dB of isolation without any external decoupling structure. The antenna proposed in [30] was mainly composed of two parallel slots acting dual loop implanted on the ground plane. In [31], the wideband decoupling property of the dual-antenna pair is realized by the combination of the orthogonal monopole/dipole modes in the lower band and the orthogonal slot/ open-slot modes in the higher band. The antenna presented in [32] architecture consists of five quasi-Yagi antennas printed on the short edge of a Roger RO3003 substrate, pointing in different directions. A conventional Vivaldi antenna with

slot-line transition was presented in a linear four-element array [58]. The slot-line transition was inserted to reduce the antenna size.

Recently, extensive works have been done for designing high-gain antenna arrays for 5G mobile network at mm-wave with novel antenna geometries [33-37]. The other internal antenna also includes planar inverted-F antenna (PIFA) [38, 39], the inverted-F antenna (IFA) [40, 41], the planar monopole antenna and dipole [42, 43], etc.

3.3 Reconfigurable techniques

Reconfigurable techniques are adapted in antenna for two main reasons. First, to achieve wide impedance bandwidth to cover all the required bands and second, to achieve reconfigurable beams.

In [15], a varactor diode was used in the feedline to achieve frequency reconfigurability. By varying the reverse bias voltage, the capacitance value varies which eventually changes the resonant frequency. Their structure is only reconfigurable for the 4G bands. Simple varactor diodes were used in [17] to cover the lower band frequencies. Two varactor diodes were arranged in series in back-to-back configuration as shown in Figure3.6. The proposed configuration overcomes the problem of the RF modulating. When RF voltage rises, the capacitance on one diode increase and the other diode decrease the tuning voltage as the effect is canceled out. As the RF voltage rises, the capacitance on one diode will increase and the other diode will decrease. It also reduces the capacitance of the single diode as the capacitances from the two diodes were placed in series with each other. So, the equivalent varactor diode capacitance of this configuration is half.

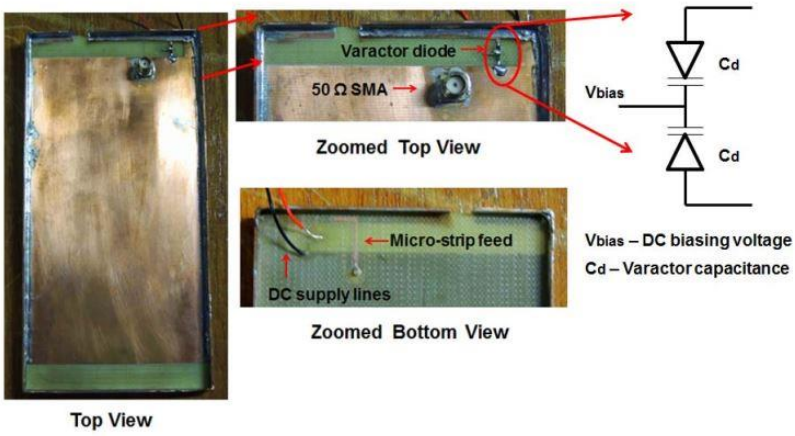

Figure 3.6 Reconfigurable open slot antenna [17]

Other antenna designs that appointed varactor diode to achieve reconfigurability are reported in [28]. To achieve broadband, band switching using ON/OFF switching (see Figure 3.13) was utilized to the end of the antenna. When the switch is ON, the stub on the ground plane was connected and the frequency shifted to low band frequency similar to the shunt matching of the capacitor. on the other hand, when the switch was OFF the stub become floating and the effect of the shunt matching was removed at low band. They demonstrated the high band can be adjusted by connecting the stub to the metal rim because the resonance length of the loop was varied. Similar topology was applied in [44] and [45]. A reconfigurable narrow-frame coupled-loop antenna for metal-rimmed smartphone applications was proposed in [46]. The proposed antenna can achieve the miniaturization by employing a PIN diode. When the PIN diode is OFF, the right portion of the ungrounded metal rim combining the left arm of the T-style strip forms a coupled loop and provide coverage for GSM850/DCS/PCS/UMTS2100/ LTE2300/2500 operations. When the PIN diode is ON, the corresponding physical length of the coupled loop became short, and the obtained bands are GSM900/DCS/PCS/UMTS2100/LTE2300/2500.

A radiation-pattern reconfigurable phased array using PIN diodes for 5G handsets was proposed in [47]. They use dipole and directors to achieve mmWave band. When the PIN diodes were OFF, the strip line feeding is activated as a director. Therefore, strong current observed as a result the radiation direction changes. On the other hand, when the PIN diode were in ON stage, there was no such current therefore radiation direction did not change. By ON and OFF stage authors showed both broadside and endfire radiations. A wideband beam switchable antenna array was shown in [32] without the need of phase shifters as shown in Figure 3.7. The design consists of a switchable array of five high gain quasi-Yagi antennas placed on the short edge of the PCB with different orientation. Switching to the feed of each element, it is possible to scan an area of 180^{o} at 28 and 38 GHz.

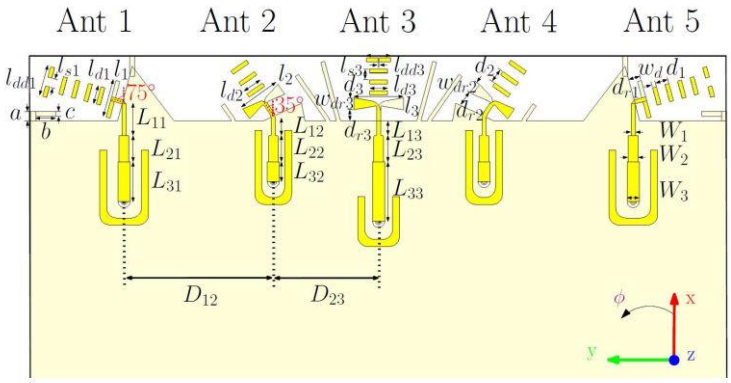

Figure 3.7 Beam switchable quasi-Yagi antennas for 5G handsets [32]

The most common types of RF switches are PIN diode switches [48], field-effect transistor (FET) switches and microelectromechanical systems (MEMS) switches [49, 50].

3.4 Feeding techniques

Different types of feed techniques have been developed over the years for antenna. Two of the mostly used feeding techniques in literature are microstrip feedline and coupled feedline. Some of the feeding techniques used in handset model are briefly discussed here.

In [15], the microstrip feeding line was adapted to cover multiple bands with a dc controlling circuit, consist of varactor diode, inductor, and capacitor. A DC voltage was applied at the point U mentioned in Figure 3.8. this DC voltage can be varied therefore the capacitance of the varactor diode will change. For the practical design point of view, they used a single pole double throw (SPDT) switch to select different inductance values for matching purpose.

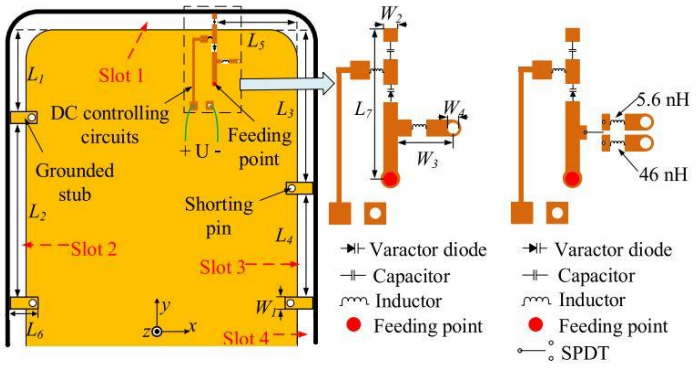

Figure 3.8 Microstrip feeding network with DC controlling circuit [15]

A simple microstrip feedline was used in [16]. A open slot antenna fed by an L-shaped microstrip feed line capable of supporting octa-band operations was proposed in [17]. The feeding strip introduces a capacitive loading effecting the resonances. It can be controlled by changing the length of the feeding strip. They also showed how capacitance loading effects by the position of feed location. In [18], they used an inverted-L feedline along with a chip capacitor to generate required resonant modes. Another inverted-L stub was designed with a ON/OFF switch for band switching in low band. For the high band, a cross-shaped matching network consist of inductor and capacitor was embedded in the feeding strip to greatly enhance the bandwidth. Another L-shaped coupled feedline with matching networks was reported in [30].

A dual polarized mm-wave transmission line that introduces low common mode capacitance without degrading sub-6 GHz antenna operation was presented in [23]. The horizontal and vertical polarization coupler is shown in Figure3.9. The series capacitance at mmWave frequencies generally compensated with series or parallel inductances or combination of both. Therefore, the mm-wave signal can propagate along the line without significant attenuation.

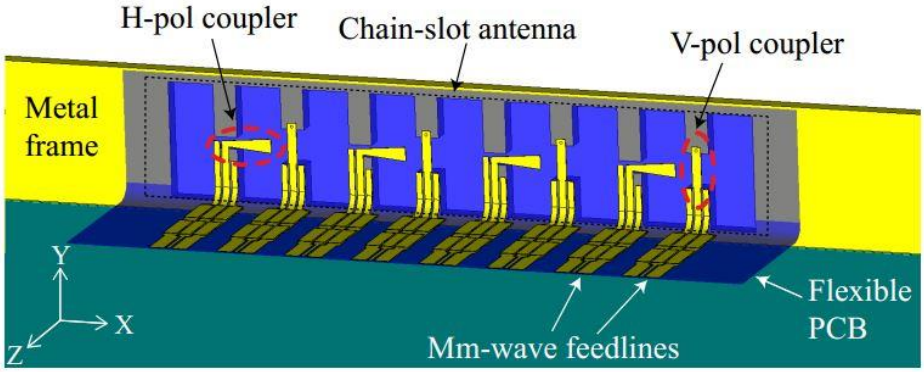

Figure 3.9 Feeding of chain-slot antenna in [23]

In order to feed both microwave and mmWave bands the authors in [28] come up with dual feed antenna structure. For microwave band, a simple microstrip feedline was introduced. But for the mmWave band as it was an antenna array, a 1×8 T-junction power divider was designed at 28 GHz to feed the slot as a CAA can be seen in Figure3.13. A commercial differential balun chip Anaren BD3150N50100AHF was used in [31] to excite two different modes for the metal rim antenna. Distributed Feeding based on switching was proposed in [48] for a metal rim MIMO handset antenna. First, they analyzed the antenna by using antenna cluster model. The design method uses

a multiport antenna simulation model built from a large number of small unit antenna elements where short and open circuits were needed. To get the proper excitation ideal switches was used. Later these ideal switches were replaced with PIN diodes for fabrication. Apart from that they also used DC block capacitors and RF choke inductors to provide relatively low and high impedances, respectively, at the operating frequencies.

A theoretical analysis and design rules for a capacitively-loaded feed line was studied in [51] as in Figure3.10. The electrical behavior allows the mm-wave (24.25–29.5 GHz) antennas to be integrated in the metal frame without short-circuiting other antennas at sub-6 GHz (0.7–5.9 GHz) band. The designed feed line behaves like a transmission line at the mm-wave band while a small common mode capacitive loading can be seen in the sub-6 GHz antenna. They also implement their concept into practice and measured to verify the theoretical analysis and simulated performance with insertion loss of 1 dB. After that, the effect of the introduced capacitive load was found only 0.19 pF on the sub-6 GHz antenna performance which is in tolerable rage.

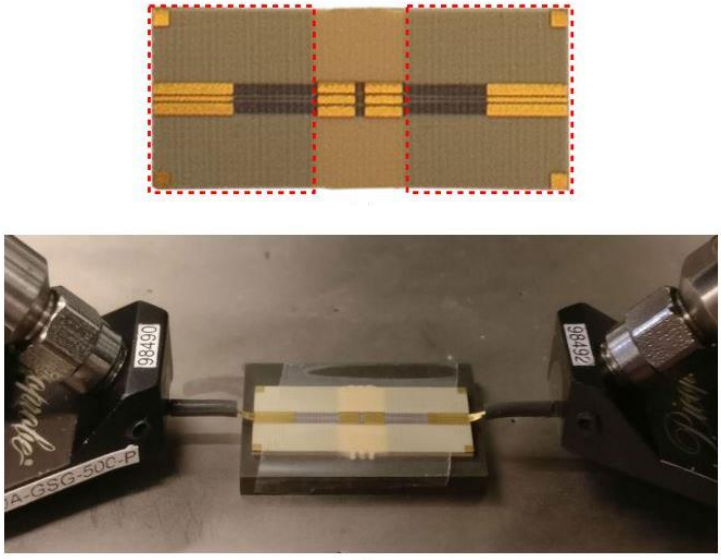

Figure 3.10 Capacitively-loaded feed line for mmWave and sub-6 GHz [51]

3.5 Analysis of smartphone components

The placement of the handset components is also crucial in antenna design. Normally antennas were designed considering they were operating in the free space but in the mobile phone

environment some modifications and adjustments are needed. All these components are assumed to be perfect electric conductor (PEC) for the modeling.

Guo and his team in [16] showed the effects of the components namely the large-size touch screen LCD, battery, camera, speaker, buttons and connects, that a modern smartphone usually contains illustrated in Figure3.11. The primary effect of the components was on the return loss. To conquer this effect, they optimized the dimensions of the internal antenna to improve its performance. According to their results, the presence of handset components generates new resonance and has an impact on impedance bandwidth. From [17], it can be seen that there is a slight offset in total efficiency performance due to the presence of LCD screen, speaker and USB connector. To minimize this, authors optimized the location of feeding strip.

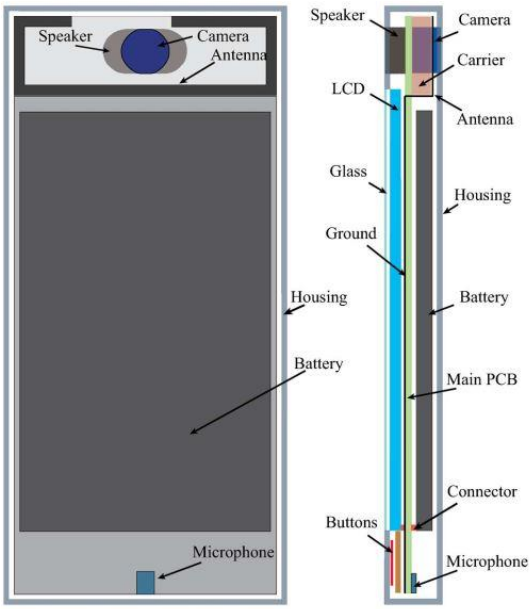

Figure 3.11 Smartphone with its components [16]

Only the LCD and the window glass were incorporated for the full-wave simulation in [18]. Authors discovered approximately 7%–10% degradation of total efficiency when a 2 mm gap was secured between LCD and antenna. The window glass they used had a relative permittivity of 4 and a conductivity of 0.02. In [23], authors implemented the components all together during the design. They placed an RFIC 5G transceiver module to feed the coupling elements as in Figure

3.12. They did not show the influence of these components separately. The effects of the components on antenna performances was also studied in [27],[52].

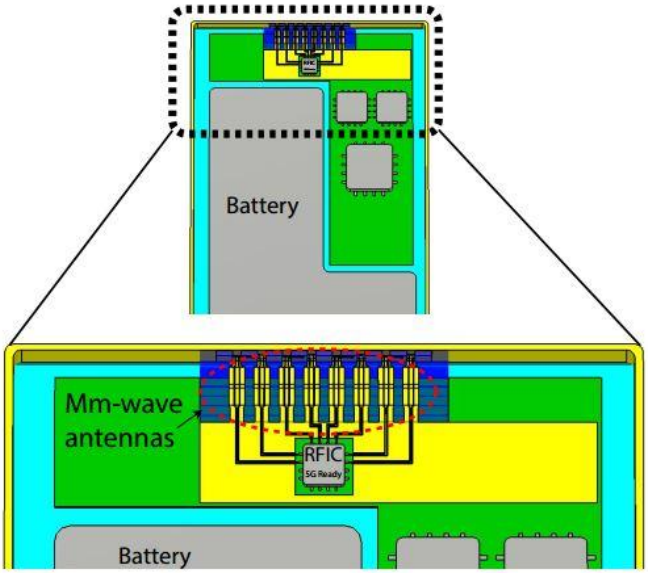

Figure 3.12 mmWave antenna connection with the RFIC inside the smartphone [23]

3.6 Integrated microwave and mmWave antennas

The introduction of 5G devices operating at mm-wave frequencies has raised significant challenges for communication industry, particularly for handheld devices. The high path loss of mm-wave bands can be minimized by using antenna arrays with increased gain [33]. Another challenge is the colocation of the microwave and mmWave antennas due to the limited space available in the handset chassis To address the challenges of co-operating with existing 4G infrastructure, several promising designs were proposed to cover both microwave and mmWave bands [52-59]. However, all the above-mentioned designs have their own restrictions. In [52] Sharawi et al. and Ikram et al. in [53] were able to achieve 4G and 5G bands, but their designs were unable to cover mmWave bands. In [55] and [57], two designs were presented with good performance at microwave and mmWave bands. But they were built on multi-substrates which is complicated and less cost effective. Moreover, both were reported with relatively low gain at the mmWave band, and both uses two different structures for the two bands. Dual-functional connected slots were presented in [53] and [56] for 4G and 5G applications. Where connected slots were used both as an isolation enhancement structure between microwave antennas and an antenna array at mmWave band. Those

designs used two different structures to cover microwave and mmWave bands therefore they occupied relatively large amount of the board eventually making them less suitable for handsets.

In [28], a dual-function slot antenna operated at both microwave and mm-wave band was proposed. Their design consists of a slot printed on the edge of the ground plane as shown in Figure 3.13. The designed slot has dual functionality, it works as a tunable slot antenna at 4G microwave band and operates as a wideband antenna array at 5G mmWave band using the principle of CAA. The tunable slot antenna has bandwidth from 2.05 to 2.70 GHz with 45-70% efficiency and 4.5 dBi of peak realized gain. The wideband CAA has bandwidth from 23 to 29 GHz with 12.5 dBi realized gain and 80-90% measured efficiency. They also used a compact high-pass filter (HPF) in the feeding structure to isolate the two ports. Two orthogonally positioned slots were implemented to form MIMO configuration. The whole 70×60×0.381 mm^3 structure was printed on Rogers 5880 substrate. The envelope correlation coefficient and isolation were minimum 0.01 and more than 20 dB among the feeding ports.

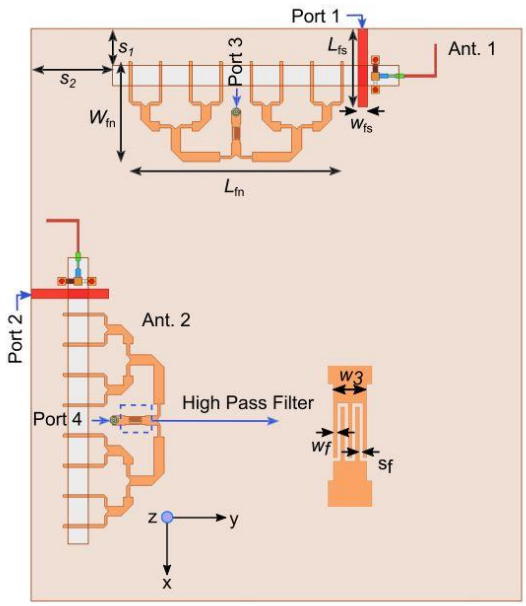

Figure 3.13 Geometry of MIMO using CAA antenna reported in [28]

An aperture-sharing methodology was proposed in [58], they presented a four linear array antenna at 28 GHz array along with a 3.5 GHz dipole antenna that are using the same aperture to resonant. A double sided parallel strip line (DSPSL) was used to feed the double sided dipole antenna as

shown in Figure 3.14, by using this method they incorporated the mm-wave antenna array. Microstrip balun was also adapted to achieve the transition from DSPSL to grounded coplanar waveguide (GCPW). At mm-wave band, a double-sided interdigital coupling (IDC) structure was introduced into each DSPSL to achieve broad bandwidth by implementing indirect coupling. The overall structure size was 33.9×43×0.254 mm^3 and the reported gain of the mm-wave array and 3.5 dipole antenna varies from 5.8 to 7.5 dBi and 6.1 to 6.9 dBi over the BW, respectively. They achieved a very good 10 dB measured impedance bandwidth which is approximately 20% in both bands. The beamsteering capabilities of the structure was limited to 0^o and 25^o in the E-plane because they used two different fixed feeding networks for the 28 GHz array antenna. As it is a double sided antenna structure, it may suffer some difficulties when implementing in the mobile phone structure.

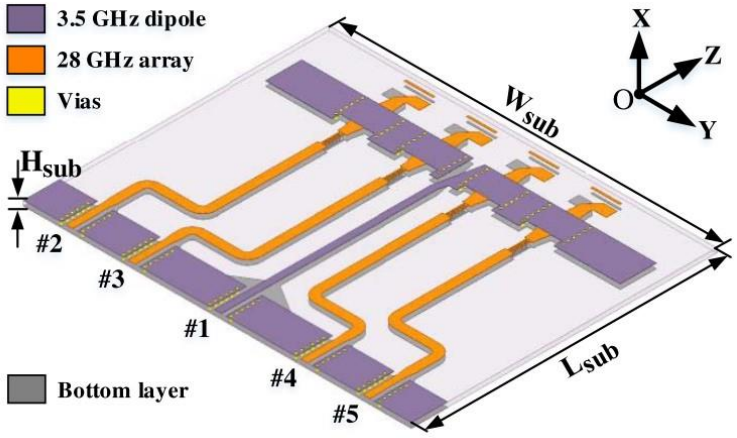

Figure 3.14 Configuration of the aperture sharing dual band antenna in [58]

Another aperture sharing broadside antenna was investigated by Ding and his team by March 2022 [59]. A substrate-integrated DRA (SIDRA) with a 2×4 configuration at 26 GHz and a segmented patch antenna at 3.5 GHz was utilized in an aperture shared way shown in Figure 3.15. The segmented patches wide bandwidth capabilities with low antenna profile. has They reported three benefits: compact size, size adaptation of SIDRA with the patch antenna and high integrity level. It is a mm-wave beamsteering capable multi-layer structure. To improve isolation between the two bands, they used metalized grooves surrounding the SIDRAs to isolate the microwave antenna. Separate feeding network was applied to accomplish independent excitation and radiation pattern. They reported a 12.3% BW at microwave band and a 13.1% at mm-wave band with 5.3 and 15.4

dBi peak gain respectively. Their measured beamsteering capabilities are also limited to 0^o and 25^o because they also use power divider as a result, they had to make two prototypes. Although it has good results, but the multilayered structure and use of DRA make it complex antenna for 5G mobile phone.

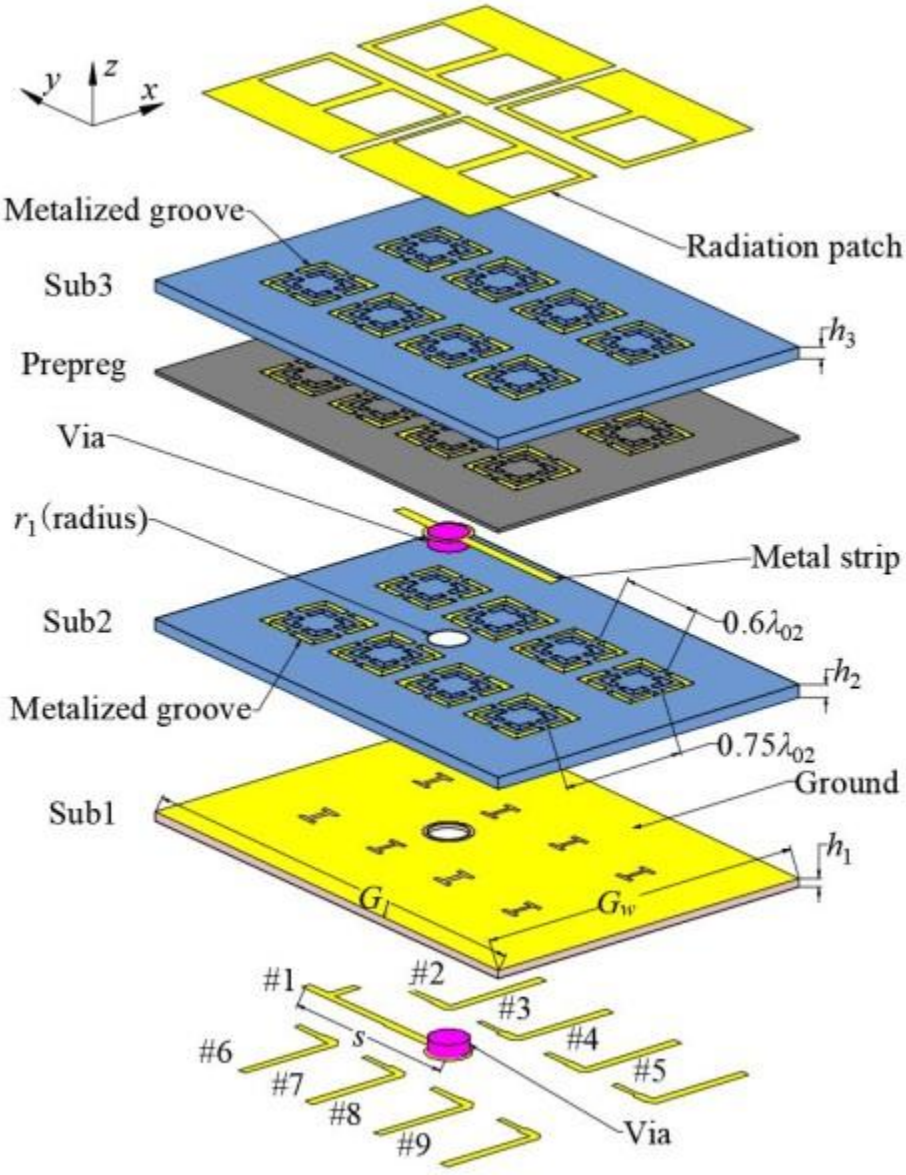

Figure 3.15 Structure of the aperture sharing dual band antenna in [59]

Table 3.1 show a comparison summary between the previous work with respect to frequency band, bandwidth, peak realized gain, size of the board, and number of antenna elements.

Table 3.1 Comparison summary of previous work

Ref.	**Published Year**	**Frequency (GHz)**	**Bandwidth**	**Peak Realized Gain**	**Size (mm^3)**	**Antenna Types**	**Beamsteering Capability**
[28]	2019	2/24/28	Frequency reconfigurable 650 MHz/1.5 GHz (24GHz) & 2.6 GHz (28 GHz)	4.5 dBi/12.5 dBi	35×12.28×0.38	Single slot/CAA: 8 elements	No
[58]	2020	3.5/28	510 MHz (3.5 GHz)/5.44 GHz (28 GHz)	7.07 dBi/11.31 dBi	33.9×43×0.254	Dipole/Dipole 5 elements	±25^o
[59]	2021	3.5/26	430 MHz (3.5 GHz)/3.4 GHz (26 GHz)	5.3 dBi /13.9 dBi	35×25×2.74	2×6 Patch/SIDRA	±40^o (sim.) ±25^o (mea.)

3.7 Antenna in Antenna (AiA)

A relatively new concept has been developed because of the space availability for the antenna in smartphone devices. In antenna in antenna (AiA) concept, two antennas are incorporated in such a way that one antenna structure operated in a frequency band is used for the second antenna that is operated in a different frequency band.

A dual-band mmWave antenna array working at 28 GHz and 39 GHz for the 5G was proposed in [60]. They used two interconnected slots of different length to enable the integrated design with a metal rim of a handset and claimed it as a promising solution of antenna in antenna (AiA) concept especially when the metal rim serves as non mmWave antennas. A 5-element antenna array was designed on smartphone metal rim. A metal wall as a reflector was placed behind the antenna array for better front-to-back ratio. As shown in Figure 3.16, the dual-band antenna consists of a common feeding (red dot) and grounding (blue dot) points. The simulation results showed bandwidth from 27.4 to 29.6 GHz and from 36.9 to 40.2 GHz to cover the 5G mmWave bands of n260 and n261. When the array performed the beam scanning, the peak realized gains of the array were 11.3 dBi and 12.0 dBi and the lowest antenna array efficiencies are -0.42 dB and -0.33 dB at 28.0 GHz and 39.0 GHz, respectively. The maximum scan angles are ±60°.

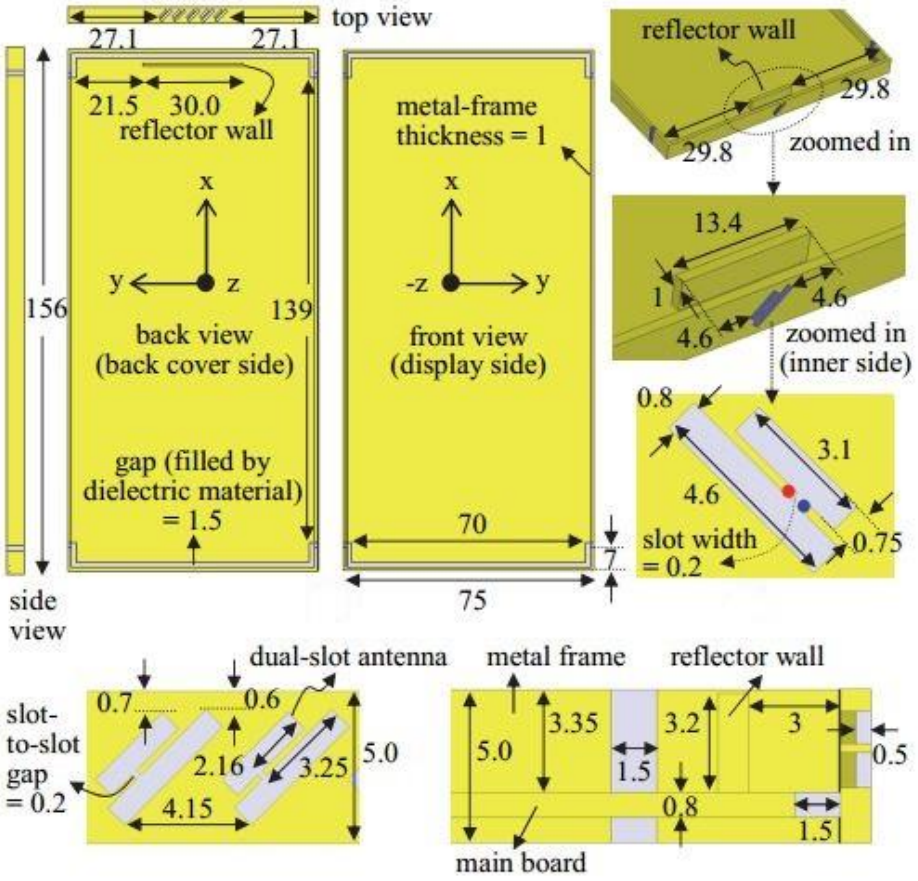

Figure 3.16 Dual band dual slot metal rim antenna [60]

The following year Wang and his team proposed another antenna with similar AiA concept [61]. But this time, one antenna resonant at microwave and the second one resonant at mmWave bands. The dual-band mm-Wave antenna was composed of two square patches, the top small one for the 5G mmWave high band and the bottom large one for the 5G mm-Wave low band. The top small square patch was directly fed by two truncated metal vias to excite the V-pol. through the P5 and the H-pol. through the P6, as shown in Figure 3.17. The two feeds are placed on the orthogonal centerlines from the two edges of the top small patch for similar levels of dual-polarizations in dual bands and for good port isolation. The bottom large square patch is not directly fed by the two truncated vias; instead, it is coupled by the top small patch. The gray part was filled with a material (dielectric constant of 2.2 and loss tangent of 0.009). The LTE mid band was coming from the metal rim itself, feeding with matching components. All the bands achieved realized gain higher than 11 dBi.

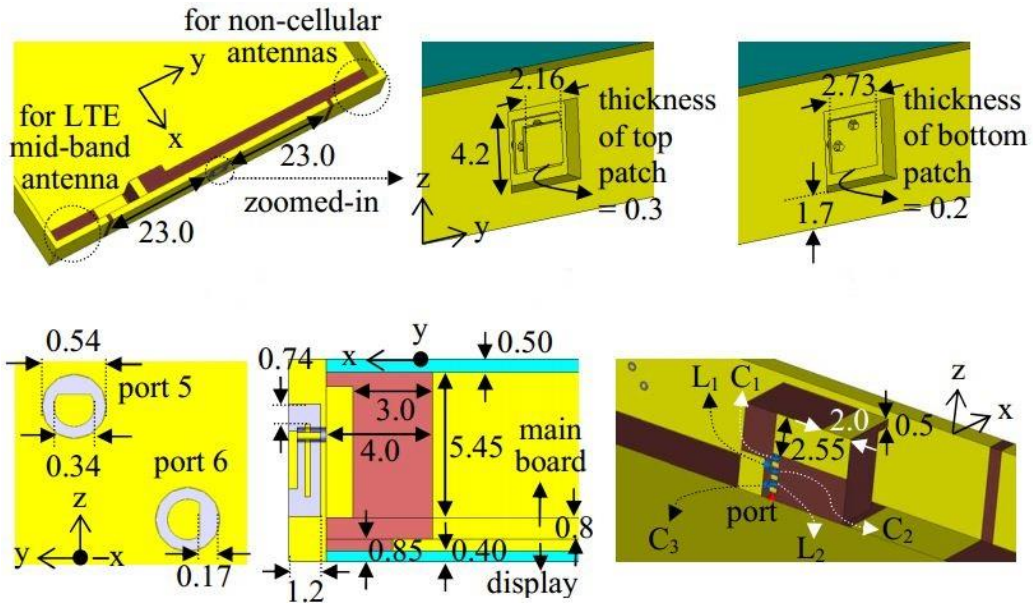

Figure 3.17 Dual-band mmWave antenna composed of two square patches with LTE antenna [61]

Other ways are using one antenna with two different feeding structures to operate at two different frequency bands. This type of antenna is discussed in section 3.6.

3.8 Conclusion

In this chapter, a comprehensive review of the works conducted by other researchers previously is presented. At first, general overview of metal rimmed antenna, and classifications based on operating frequency are discussed. Next, the types of antennas used in smartphone antenna design and its performance are reviewed. Different techniques of reconfigurable and feeding of the antenna have been reviewed on recently published research works. It is observed microstrip coupled feedline is more promising and easier to fabricate. Then the effects of smartphone components are also discussed, and their presence impacts much on gain and efficiency. Lastly, a new concept based on AiA has been reviewed in other to achieve both microwave and mmWave frequency bands. So, the emphasis is grown on designing compact, low profile metal rim antenna for portable handset devices.

CHAPTER 4 IN-RIM CSAA ANTENNA SYSTEM

This chapter contains the results and discussion of in-rim slot antenna using connected antenna array. First, a single slot antenna is designed at mmWave band (28 GHz) and analyzed with backing reflector using CST microwave studio simulation software. After that, the principle of CAA applied on it with 4 antenna elements. Moreover, the beamsteering of the connected slot antenna array (CSAA) is presented with proper phase shift to demonstrate the capabilities of the proposed antenna in handset environment. Finally, a presentation of Antenna in Antenna (AiA) concept is shown in order to achieve both microwave and mmWave bands for future work.

4.1 Single slot antenna without backing reflector

A single slot is cut in the middle of a metal structure. This metal structure represents a standard metal frame of a smart handset. To reduce the simulation time, only a portion of the metal rim frame is considered. The metal rim is 40 mm in length, 7.4 mm in width and 1 mm in thickness. A standard iPhone 12 smartphone in the market has the same width and thickness. To feed the slot antenna, a microstrip feedline is used. A dielectric substrate is placed beside the metal rim and a portion of the PCB circuit board is also considered to feed it in the fabricated prototype. The rogers RO3003 substrate is used and has a relative permittivity of $\varepsilon_r = 3$, loss tangent of $\tan\delta=0.001$ and thickness of 0.13 mm (1/2 oz. ≈ 17 μm copper). A slot can be feed by two methods: center feed (λ/4) and offset feed (λ/20). Both feeding methods are investigated. The primary target is to resonant at 28 GHz with 2 GHz bandwidth. The calculated wavelength at 28 GHz is:

$$\lambda = \frac{3\times10^{8}}{28\times10^{9}} = 10.714$$

The terminal resistance at the center of a resonant λ/2 slot in a large sheet is about 500 Ω and the characteristic impedance of transmission lines is usually much less, an off-center feed may be used to provide a better impedance match. For a 50 Ω coaxial cable, the distance from the edge of the slot to feed point should be about λ/20 [62]. As shown in Figure 4.1, in order to resonant we need to decrease the antenna length to make the reactance part zero.

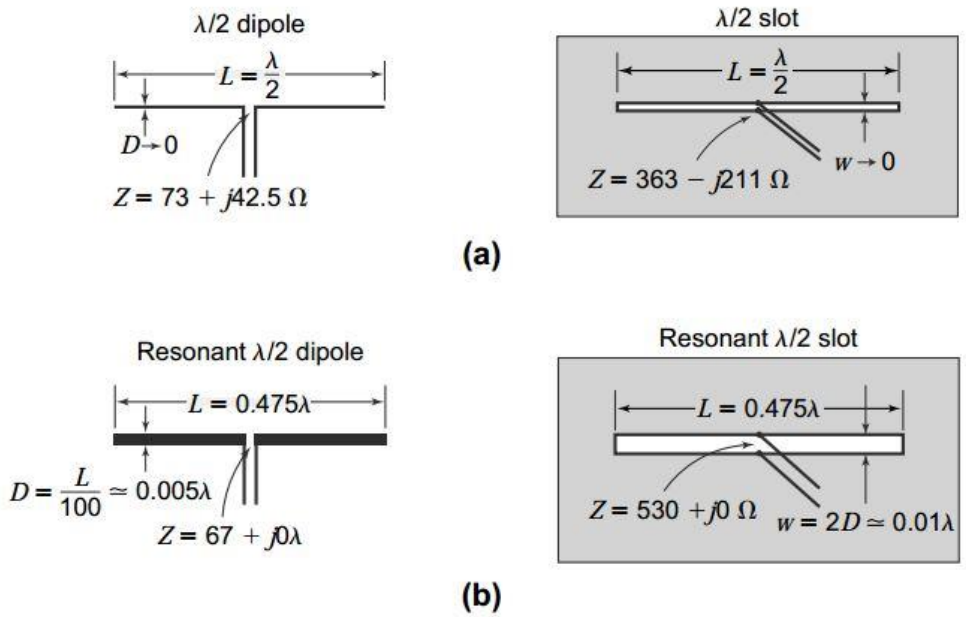

Figure 4.1 (a) Nonresonant and (b) Resonant, dipole and slot antenna [62]

Using Quarter-Wave Transformer [63]:

$$Z_o = \sqrt{Z_{in} Z_L} = \sqrt{(50 * 530)} = 162.7\Omega \tag{4.1}$$

To feed the antenna at center, matching with high impedance like 530Ω is required. A transmission line with a characteristics impedance of 162.7Ω is needed to match the input impedance of 50Ω. For 162.7Ω, the width of the microstrip feedline is 0.0196 mm which is not suitable for practical use. Fabrication of this width is very difficult on such a substrate.

The voltage reaches its maximum at the center of slot (λ/4 from the edges), and it is minimum at the edges. In contrast, the current is negative at one edge, reaches zero at the center, and it is positive at the other edge or vice-versa in polarity. So, moving from the center and find the suitable place where the impedance of the slot is around 50Ω, then the slot antenna have the better impedance matching namely offset feed.

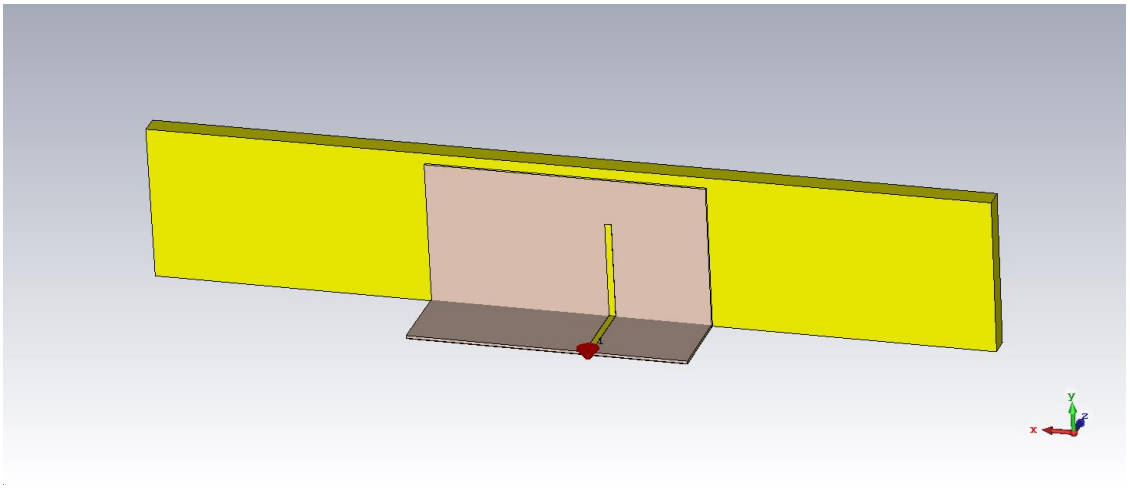

(a)

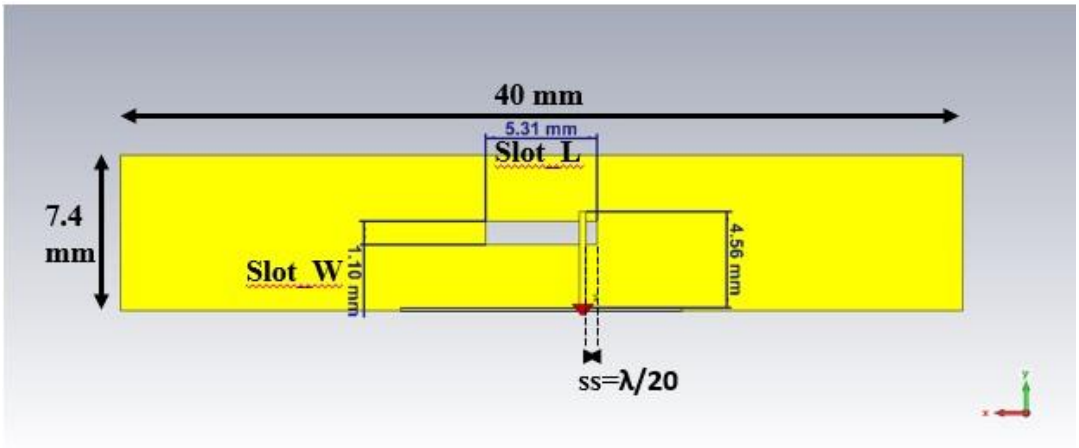

(b)

Figure 4.2 Structure of single slot antennas using offset feed (a) prospective view and (b) front view

Figure 4.2 shows the structures of in-rim single slot antenna for offset feed case. The dimensions of the structures are shown in the figure. The simulation results of the reflection coefficient (S_{11}) are shown in Figure 4.3. The simulated structure exhibits bandwidth ($S_{11} < -10$ dB) of 2.52 GHz (26.55–29.08 GHz) when excited at the center and bandwidth ($S_{11} < -10$ dB) of 3.12 GHz (26.46–29.61 GHz) when excited with offset feed, both are centered at 28 GHz. Better matching can be observed from the offset feeding method, with a 600 MHz additional bandwidth.

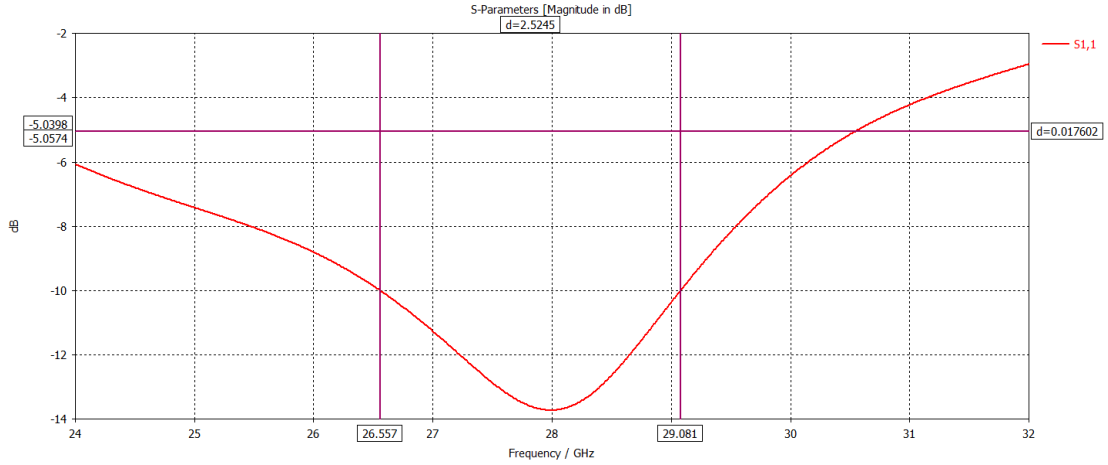

(a)

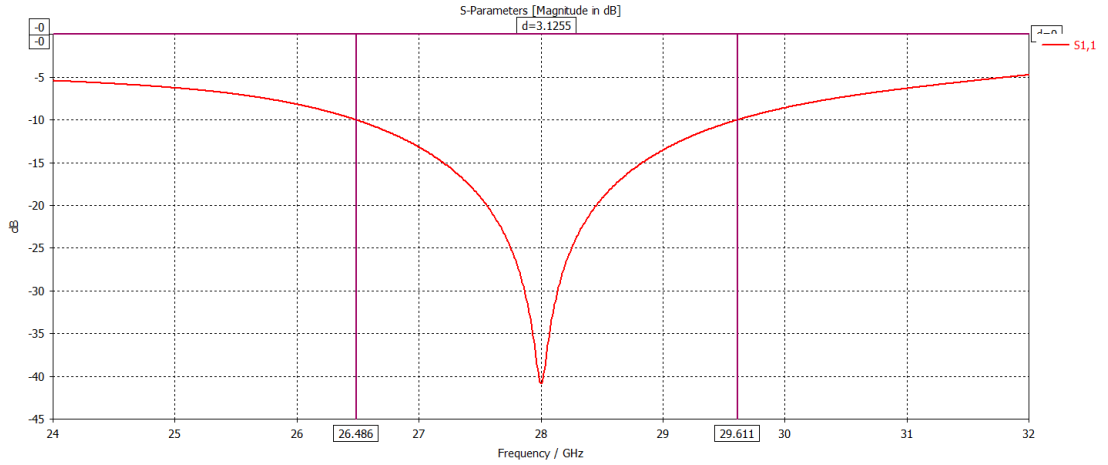

(b)

Figure 4.3 Reflection coefficients of the in-rim slot antenna (a) Center feed with quarter-wave transformer and (b) Offset feed

Almost similar radiation efficiency can be observed which is 96% from both feeding method. But the total efficiency of center feed method is 91% where offset feeding exhibits 96%. The reason of this 5% is the mismatch losses coming from the quarter wave transformer of center feed method. The radiation pattern of the single slot antenna is illustrated in Figure 4.4. A dumbbell shaped pattern is observed with 5.05 dBi realized gain for center feed and 5.41 dBi for offset feed. The main lobe of the offset feed antenna is tilted by two degrees.

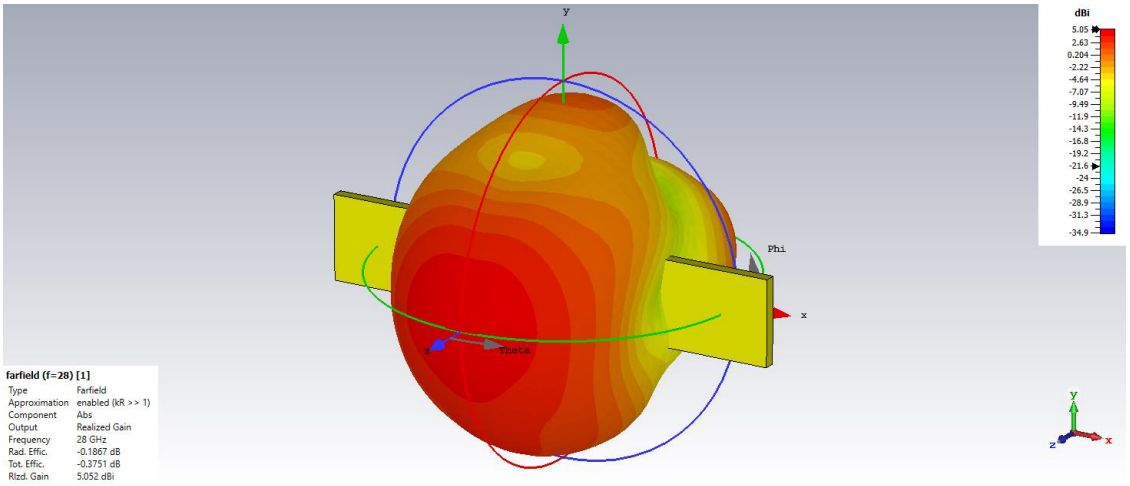

(a)

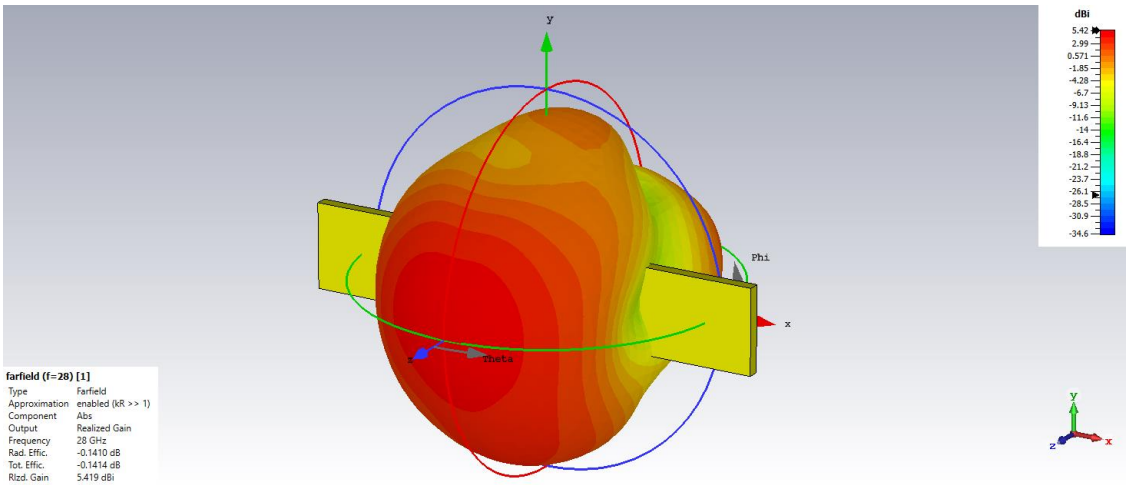

(b)

Figure 4.4 Radiation patterns of single slot antenna (a) Center feed and (b) Offset feed

After careful investigation, in both cases wide bandwidth can be achievable by properly tuning the impedance matching of the slot antenna. But based on the results from above offset feeding method is chosen for further investigation. The summary of results is listed in Table 4.1.

Table 4.1 Results for one slot antenna with two types of feeding

	Center feed	**Offset feed**
Rim length (mm)	40	40
Rim width (mm)	7.4	7.4
Rim thickness (mm)	1	1
PCB board extension (mm)	4	4
Slot length (mm)	4.75	5.31
Slot width (mm)	1.1	1.1
Distance from the edge of the slot to feed point (mm)	N/A	λ/20=0.5357
Feedline width (mm)	0.3091 for 50Ω 0.0197 for 162.7Ω	0.3091 for 50Ω
Feedline length (mm)	1.42 for 50Ω 2.7 for 162.7Ω	4.56
Bandwidth	2.52 GHz	3.12 GHz
Center Frequency	28 GHz	28 GHz
Radiation Efficiency (%)	95.79	96.8
Total Efficiency (%)	91.72	96.79
Directivity (dBi)	5.43	5.55
Realized Gain (dBi)	5.05	5.41
Main lobe direction	0^o	2^o

To investigate the effects of the parameters on the in-rim slot antenna, parametric sweep of the feed point distance from slot edge named **ss (**λ/ss**)** has been done. The results of variables are shown in Figure 4.5. If the feed point is moved away from the edge of the slot, the resonant frequency shifts towards higher frequency and vice versa. The impedance matching is also affected by that.

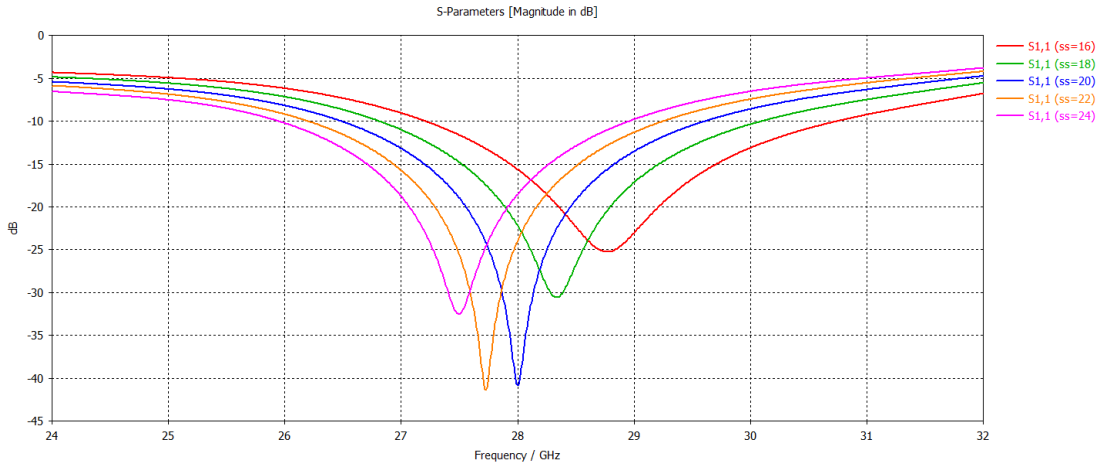

Figure 4.5 S_{11} of single slot antenna for ss variations

If the slot width (Slot_W) is increased the bandwidth of the slot antenna will increase because of the feedline matching as shown in Figure 4.6. Here, feedline length is fixed. This can be explained by the quality factor Q of the structure. If we increase the slot width the distance between the two edges of the slot will increase as a result capacitance will decrease. From equation (4.2), as capacitance C decrease Q will decrease. As the relation between the bandwidth (BW) and quality factor is proportional so bandwidth will increase [63].

$$Q = \omega_o RC \tag{4.2}$$

where, R is resistance and C is capacitance

$$BW = \frac{1}{Q} \tag{4.3}$$

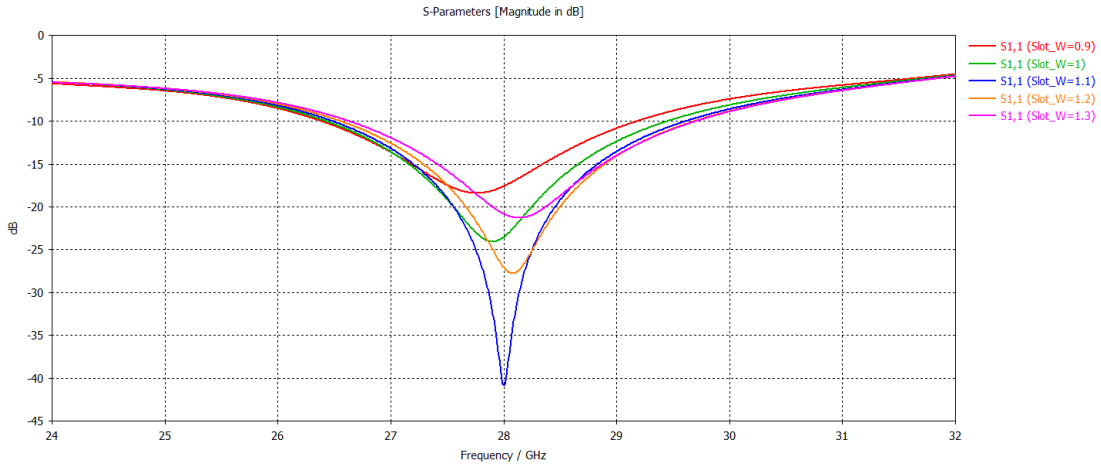

Figure 4.6 S_{11} of Slot antenna Offset feed for different slot width

4.1.1 Single slot antenna with backing reflector

In this stage, a backing reflector (BR) is placed behind the single slot antenna. No medium is used between the slot and BR, and the material of the BR is chosen PEC. A box is created to mimic the actual environment inside the smartphone as in Figure 4.7 where display, battery and other ICs will be placed. The backing reflector is placed λ/4 (2.67 mm) apart from the slot antenna.

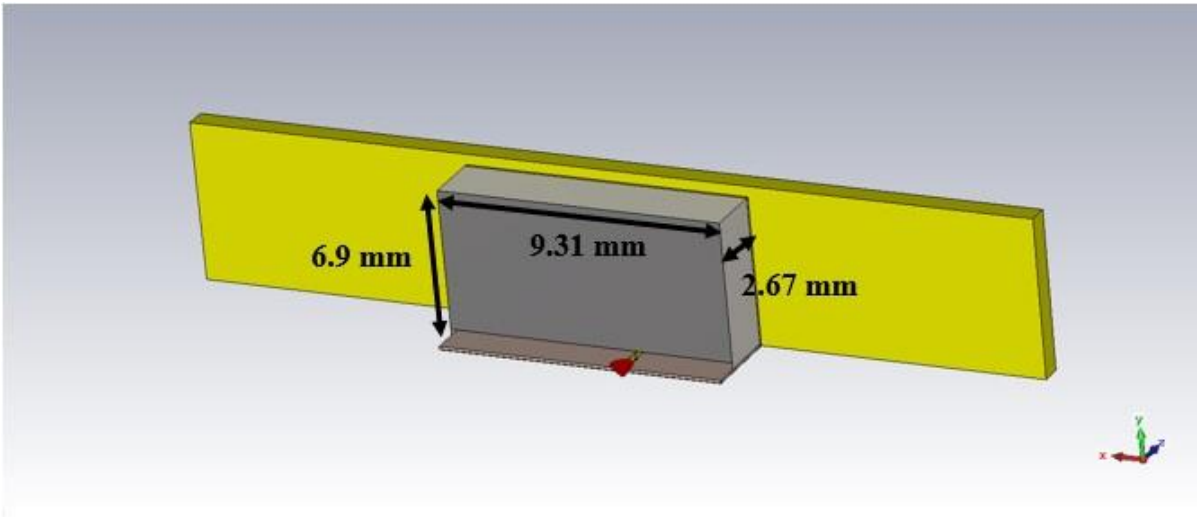

Figure 4.7 Structure of single slot antenna with BR

Flat metal reflectors are often used to achieve uni-directional radiation properties from bidirectional or omni-directional antennas. The presence of the conductor can improve the antenna gain by

redirecting the energy in the back lobe into a forward direction. When a perfect electric conductor (PEC) reflector is placed near a radiator, the image current of the antenna tends to cancel out, resulting in degraded radiation patterns. This is because a PEC reflector has a reflection phase of 180°. Another disadvantage of using a closely spaced metal reflector is that it makes impedance matching only possible over a narrow bandwidth. In order to avoid these problems metal reflectors are typically placed λ/4 away from the radiator.

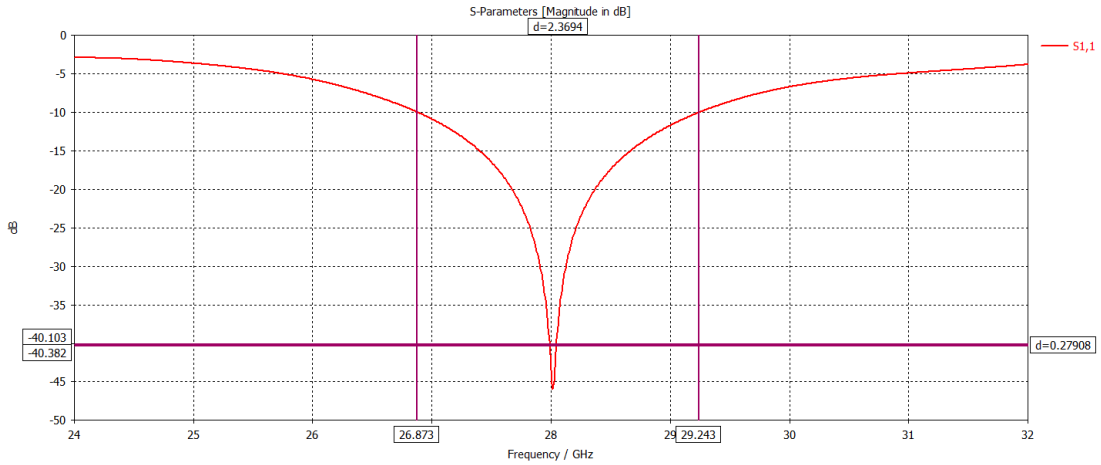

Figure 4.8 S_{11} of single slot antenna with BR

The matching is optimized by changing the feedline length. The simulation result of the reflection coefficient (S_{11}) is shown in Figure 4.8. The simulated structure exhibits bandwidth ($S_{11} < -10$ dB) of 2.37 GHz (26.87–29.24 GHz). Because of the reflector, the bandwidth is decreased and is about 750 MHz. But better matching is observed which leads to identical radiation and total efficiency (96%).

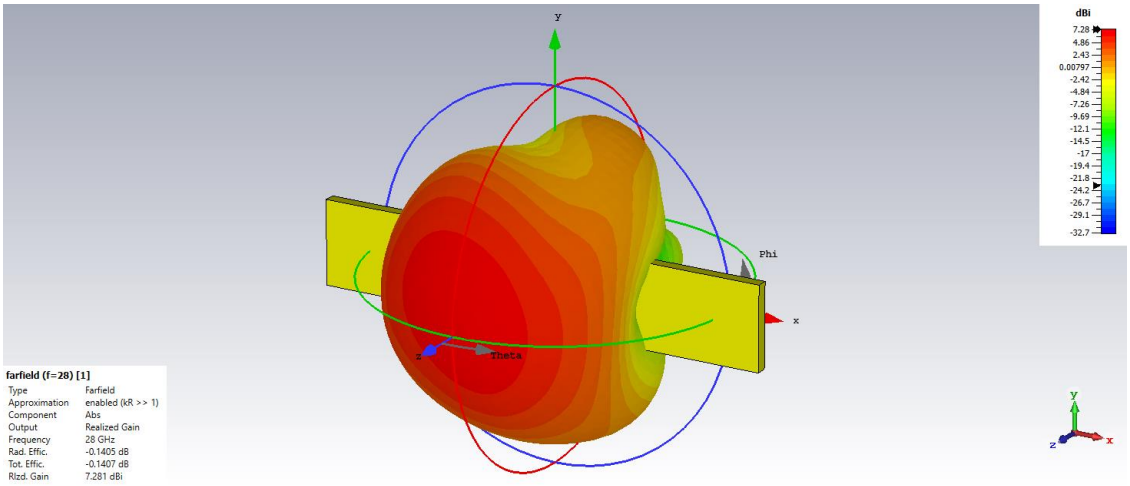

Figure 4.9 Radiation patterns of single slot antenna with BR

From the radiation pattern plotted in Figure 4.9, we can see the back radiation is pushed to forward direction by the backing reflector. A 7.22 dBi of realized gain is observed at 28 GHz. The pattern is not symmetrical because of the PCB board extension. The summary of the single slot antenna with and without BR is listed in Table 4.2.

Table 4.2 Summary of Slot antenna with and without BR at 28 GHz

	Without BR	**With BR**
Slot length (mm)	5.31	5.37
Slot width (mm)	1.1	1.1
Distance from the edge of the slot to feed point (mm)	λ/20=0.5357	λ/21.54=0.4974
Feedline width (mm)	0.3091 for 50Ω	0.3091 for 50Ω
Feedline length (mm)	4.56	4.68
Distance of BR (mm)	N/A	λ/4=2.6785
Bandwidth	3.12 GHz	2.37 GHz
Radiation Efficiency (%)	96.8	96.82
Total Efficiency (%)	96.79	96.81
Directivity (dBi)	5.55	7.36
Realized Gain (dBi)	5.41	7.22
Main lobe direction	2^{o}	4^{o}

4.2 Single Slot Connected Antenna Array System

A single slot is cut in the middle of a metal structure. This metal structure represents a standard metal frame of a smartphone handset. To reduce the simulation time, only a portion of the metal rim frame is considered. The metal rim is 50 mm in length, 8.4 mm in width and 1 mm in thickness. A standard iPhone 12 smartphone in the market has the same width and thickness. To feed the slot antenna, a microstrip feedline is used. A dielectric substrate is placed besides the metal rim and a portion of the PCB circuit board is also considered to feed it in the fabricated prototype. The slot antenna is designed implementing the concept of connected antenna array (CAA) for 1×4 elements with four microstrip feedlines. Figure 4.10 shows the structure of four element single slot CAA. A stage view is also shown to have a full understanding of the structure. It can be seen as a four elements linear array. As can be seen, all the four slots are connected so that current can be continuous and provide wide bandwidth discussed in chapter 2. The rogers RO3003 substrate is used and has a relative permittivity of $\varepsilon_r = 3$, loss tangent of $\tan\delta=0.001$ and thickness of 0.25 mm. The inter element spacing between the feedlines is kept $\lambda/2$ (5.357 mm). The microstrip feedline is 3.9 mm in length. A backing reflector (BR) is placed behind the single slot CAA. No medium is used between them, and the PEC used here is turned into a sheet. A box is created to mimic the actual environment inside the smartphone where display, battery and other ICs normally placed. The backing reflector is placed $\lambda/4$ (2.67 mm) apart from the slot antenna. The overall PCB board has a dimension of $17.13\times50\times0.25$ mm^3 with the slot size is only 17.77×2 mm^2 and the rim slot is filled with air. The substrate is bend to 90^o in order to accommodate in the mobile phone frame. The structure is compact, low profile and suitable for modern wireless handsets. The feedline is extended in the board to place the mini-SMP connectors (Pasternack's PE44489), and four nylon screws are placed to hold the board into the metal rim. Vias are also used to make a strong ground connection. A fabricated prototype of the single slot connected antenna array system is shown in Figure 4.11.

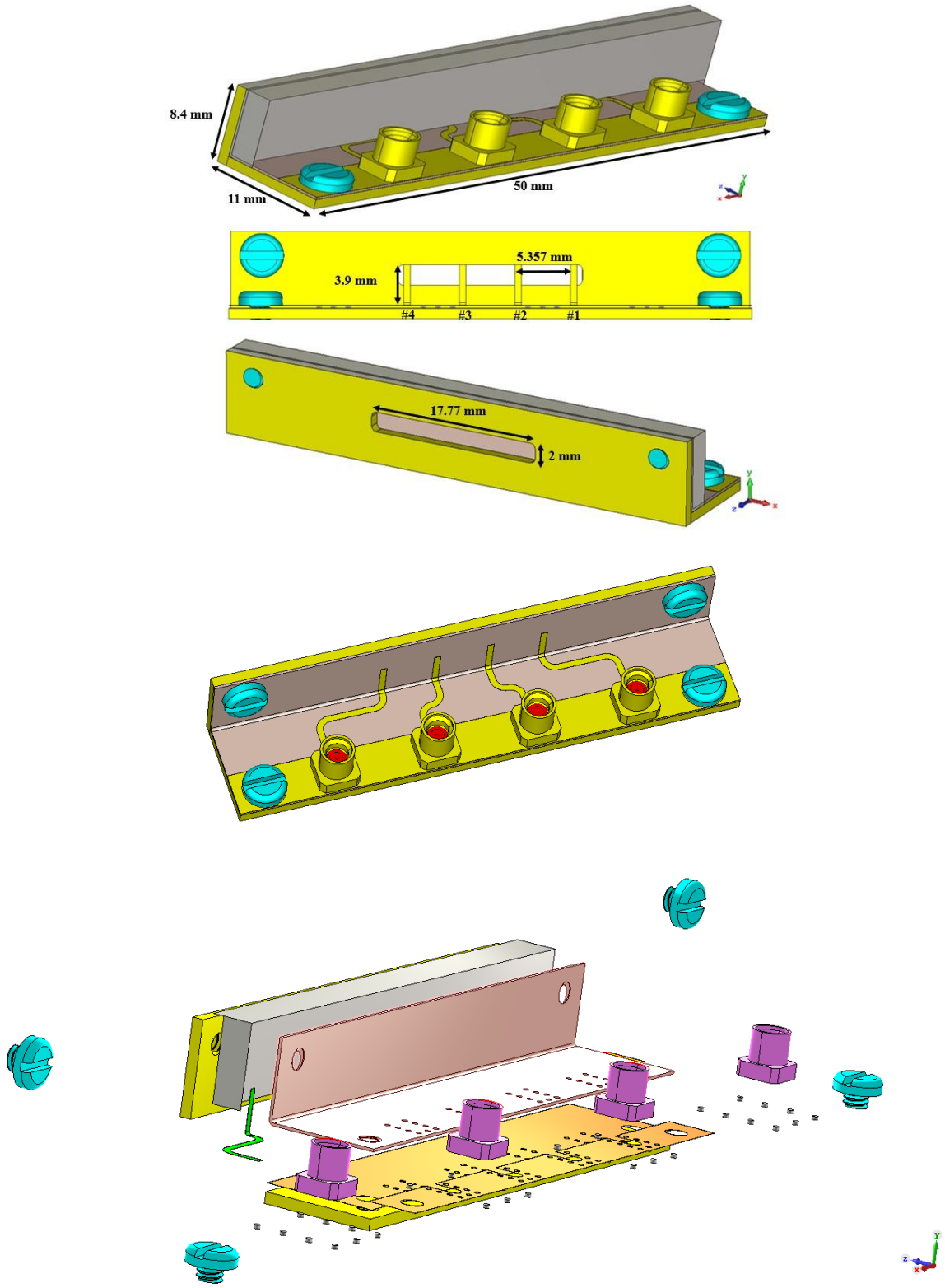

Figure 4.10 Geometry of four element single slot CAA

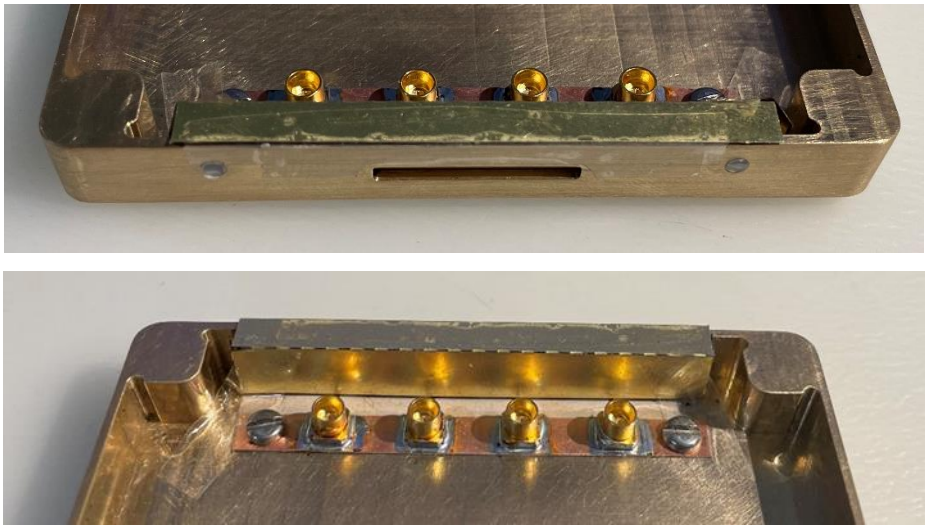

Figure 4.11 Fabricated prototype of single slot CAA

4.2.1 S-Parameters

The proposed single slot CAA system was modeled and simulated using CST Microwave Studio 2019. The simulation and measured results of the S-parameters (S_{ij}) are presented in Figure 4.12. The simulated structure exhibits bandwidth ($S_{ij} < -10$ dB) of 3.76 GHz (26.09–29.85 GHz). Due to CAA principle, the bandwidth is increased from 2.37 to 3.76 GHz. S_{22} is giving more bandwidth than S_{11} because the current is continuous in feed no. #2 but truncated in #1 due to finiteness of the structure. As element 1&4 and 2&3 are identical, only the S_{11} and S_{22} are plotted for brevity. The radiation efficiency of four feed single slot CAA antenna is 94.46% but the total efficiency is 83.05% at 28 GHz. The change between radiation and total efficiency is contributed from the matching of feed no. #2 and #3. Observing from the feed no. #1 and #4, impedance is well matched for 50Ω using offset feed but on feed no. #2 and #3 they are seeing a high impedance different from 50Ω. For the measurement, port #1 is active and others are left open. Consequently, port #2, #3 and #4 are also measured. The measured S-parameters (S_{ij}) shows similar curves but because of fabrication tolerances and mounting issues the matching is not good, and the resonant frequencies shifted in the case of measured S_{22}. The misalignment of the PCB board with the metal frame slot and the air gap in between them are affecting the measured results. Also, the placement of the backing reflector with proper ground connection is also responsible for this mismatch.

For the measurement, a coaxial cable (086 KM model) is used to connect from VNA to 2.92mm female to mini SMP female adapter (SM8921). After that, the adapter is connected to the mini-SMPs.

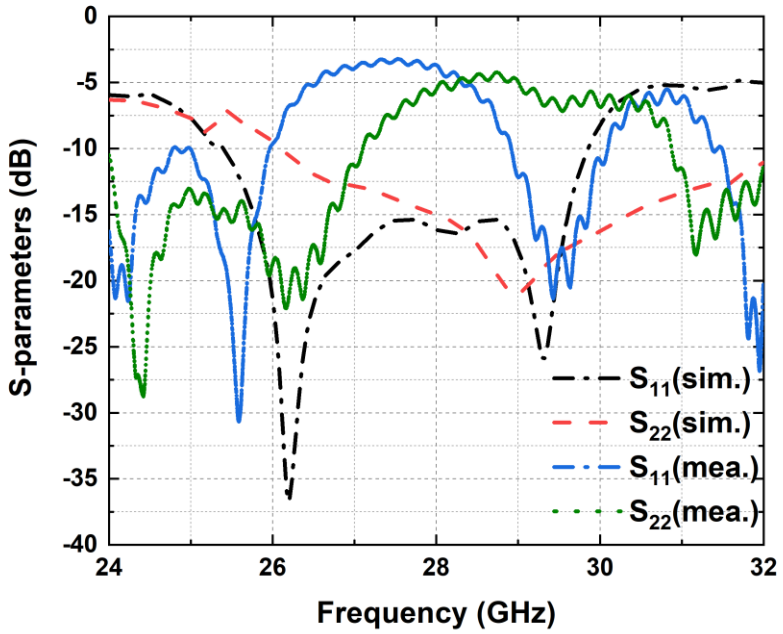

Figure 4.12 Simulated and measured S-parameters of four element single slot CAA

The isolation curves of single slot CAA are shown in Figure 4.13. The worse case isolation is around -11 dB at 28 GHz. The principle of CAA is to make the antenna elements connected because of that low isolation is expected in this structure.

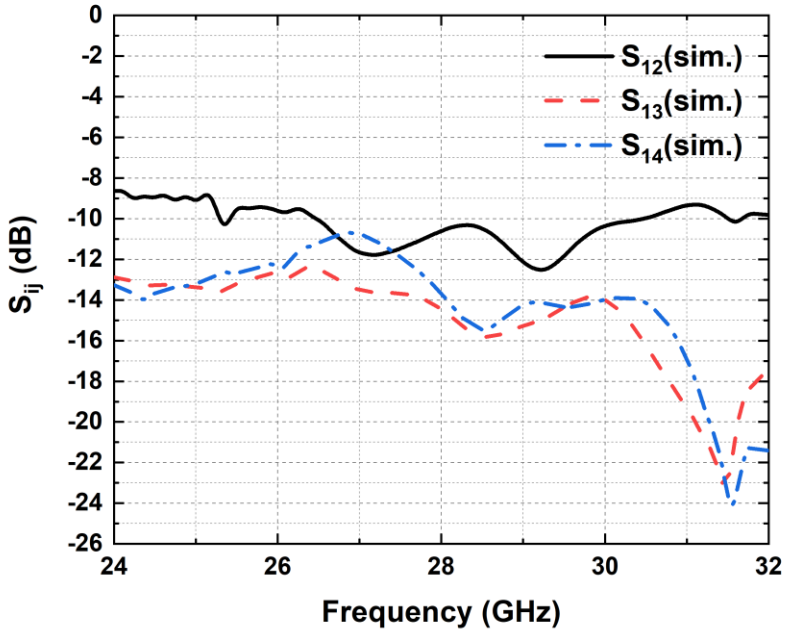

Figure 4.13 Isolation curves of four element single slot CAA

4.2.2 Tuning the design and backing reflector

To minimize the effect of BR and improve the proper connectivity with the metal frame, the BR of the structure is redesigned as shown in Figure 4.14. The BR length is now shortened (38 mm), and an arm is extended on both sides so that it can be placed tight with the existing screw the structure already has. This will increase the stability and the proper ground connection from the top side with the frame. All the other parameters are unchanged.

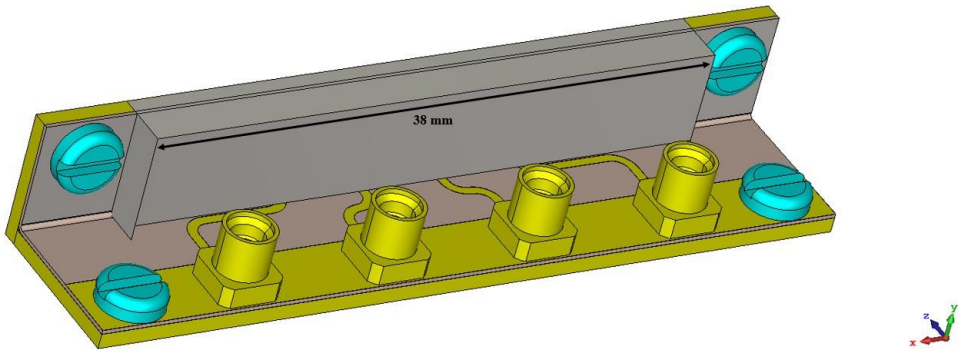

Figure 4.14 Geometry of four element single slot CAA with new BR

Further to investigate the alignment issue of PCB board with the metal frame slot, the parameter study is conducted. The important parameter that is affecting the results because of misalignment is the feedline length. In the finalized design feed length is optimized to 3.9mm but in the fabricated prototype there is slight misalignment. The results of feedline length (Feed_L) change are shown in Figure 4.15. From the fig, the dashed line when the feed length is 3.70 mm is close to the measured results which proves the misalignment issue.

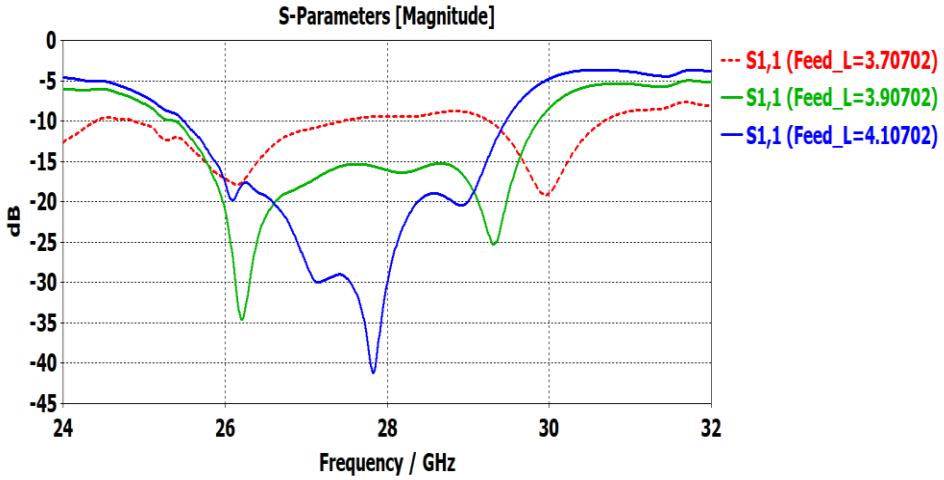

Figure 4.15 Parameter study of feed length of single slot CAA

4.2.3 Second measurement attempt

The simulation and measured results of the new structure are presented in Figure 4.16. For the measurement, port #1 is active and others are left open. Consequently, port #2, #3 and #4 are also measured. The simulated structure exhibits bandwidth (S_{ij} < −10 dB) of 4.23 GHz (26.23–30.46 GHz) as in Figure 4.16(a). But the measured results still have the matching issues for port #1 and #4, as discussed in the previous section, this is contributing from the alignment and air gap between metal frame and PCB board. The results of port #1 and #4 should be identical but it shows matching difference which explains the alignment and air gap in port #4 is better compared to port #1. The results can be improved further with proper alignment with the metal frame and good ground connection. With the new BR design the measured results significantly improved, it exhibits bandwidth (S_{ij} < −7.5 dB) of 6.42 GHz (25–31.42 GHz) as seen in Figure 4.16(b). The new fabricated prototype is shown in Figure 4.17.

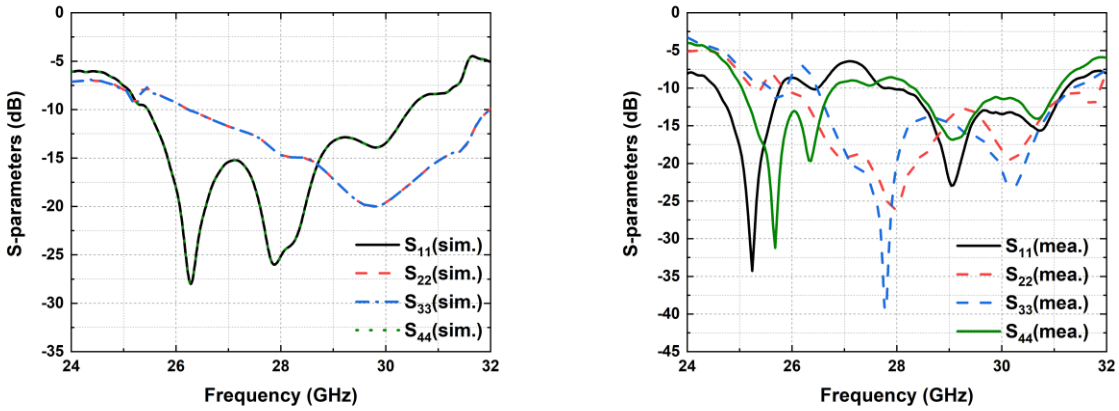

(a) (b)

Figure 4.16 S-parameters of single slot CAA with new BR (a) simulated and (b) measured

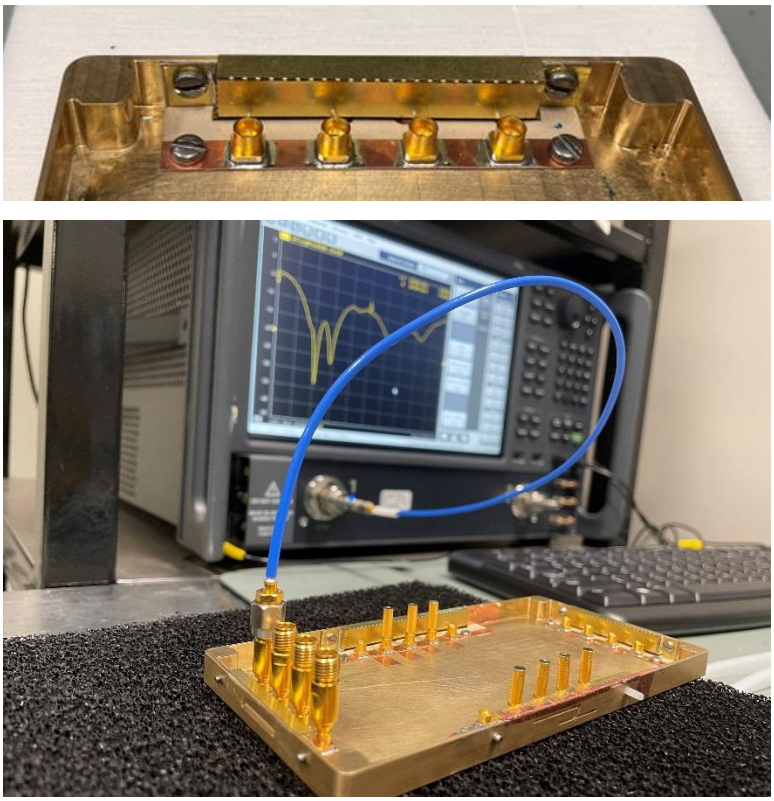

Figure 4.17 Fabricated and measurement setup of single slot CAA with new BR

4.2.4 Radiation Patterns

The radiation patterns of the structure are given in Figure 4.18. All the four elements have uniform amplitude and are equally spaced. The results of each element are combined with phase shift caused by the increased line. It has a fan beam radiation pattern with 8.94 dBi realized gain and -8.4 dB of SLL at 28 GHz. The high SLL can be explained by the thick ground plane of the mobile phone base and the slot placement is not symmetric.

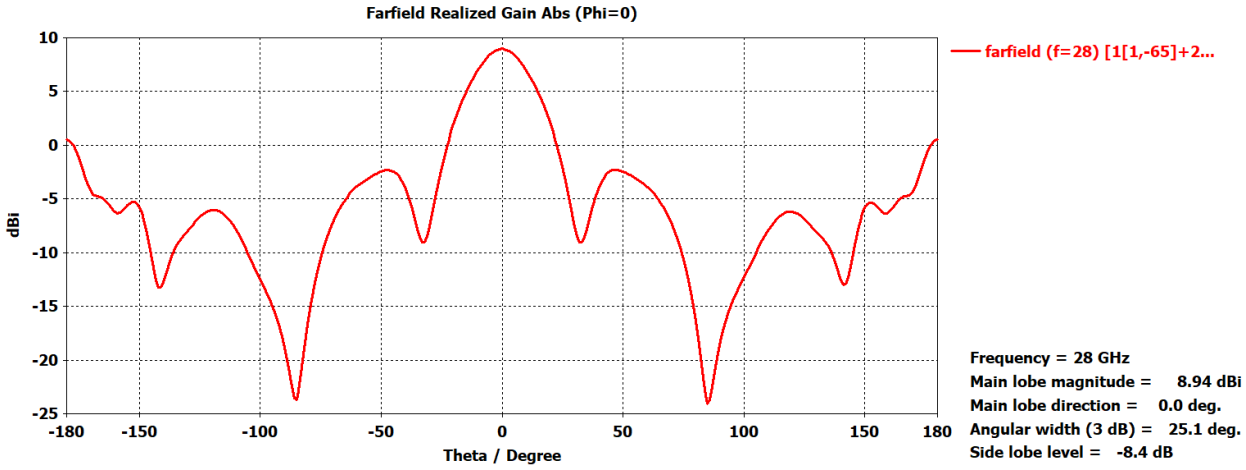

Figure 4.18 Radiation patterns of four element single slot CAA at 28 GHz phi 0^o cut

4.2.5 Beamsteering of single slot CAA

One of the vital characteristics of the mmWave antenna in 5G technology is beamsteering capabilities. In this section, the beamsteering of four element single slot CAA is investigated. The radiation pattern is normal to the antenna axis, so it is broadside array ($\beta=0^o$). The antenna is placed in the x-axis and the main beam is in the z-axis as in Figure 4.14. As, it is in x-axis, so $\beta = -kd\sin\theta_o$ as there is no ϕ dependence. To get desired beam angle θ, proper phase shift is given in to the feed elements using equation (2.7) and given in Table 4.3.

Table 4.3 Progressive phase shift for the single slot CAA at each feeding point

Desired beam towards	**Element 1**	**Element 2**	**Element 3**	**Element 4**
$\theta=0^o$	0	0	0	0
$\theta=\pm10^o$	0	-30.62	-61.24	-91.86
$\theta=\pm20^o$	0	-61.23	-122.46	-183.69
$\theta=\pm30^o$	0	-90	-180	-270

The feedline length of feed #1 and #4 are equal and feed #2 and #3 are equal. But the length of feed #1 and #4 is 16.3 mm and feed #2 and #3 is 11.5 mm. So, the phase of the feedlines needs to calculate and compensate to get desired beam steering. The calculated phase of feed #1 and #4 is 138^o and for feed #2 and #3 is about 73^o. To make the calculation simple, the feed #2 and #3 are kept 0^o and feed #1 and #4 to 65^o. For element 4, -65^o has to add with the calculated phase. The desired angle and the progressive phase shift in each element and the output of it are presented in Table 4.4 for 28 GHz.

Table 4.4 Beam steering for four element single slot CAA

Progressive Phase Shift	**Desired θ**	**Element 1**	**Element 2**	**Element 3**	**Element 4**	**Obtained θ**	**Realized Gain (dBi)**	**SLL (dB)**
β	0^o	-65	0	0	-65	0^o	8.94	-8.4
β	$+10^o$	-65	-30.62	-61.24	-156.86	$+4^o$	7.81	-6.7
	-10^o	-65	+30.62	+61.24	+26.86	-4^o	7.81	-6.7
β	$+20^o$	-65	-61.23	-122.46	-248.69	$+25^o$	7.16	-5
	-20^o	-65	+61.23	+122.46	+118.69	-25^o	7.16	-5
β	$+30^o$	-65	-90	-180	-335	$+31^o$	6.94	-6.3
	-30^o	-65	+90	+180	+205	-31^o	6.94	-6.3

The beam patterns for left side are illustrated in Figure 4.19. The beam patterns for right side are not shown for brevity. From the Figure, we can observe that the beam can be steered up to 31°. After that, the realized gain drops dramatically, and the SLL also increases. This can be explained by the pattern multiplication, when the array factor scans with phase it changes but the element pattern remains fixed. As the beam is steered the peak of the total pattern follows the element pattern shape. The element pattern is unaffected by scan angle.

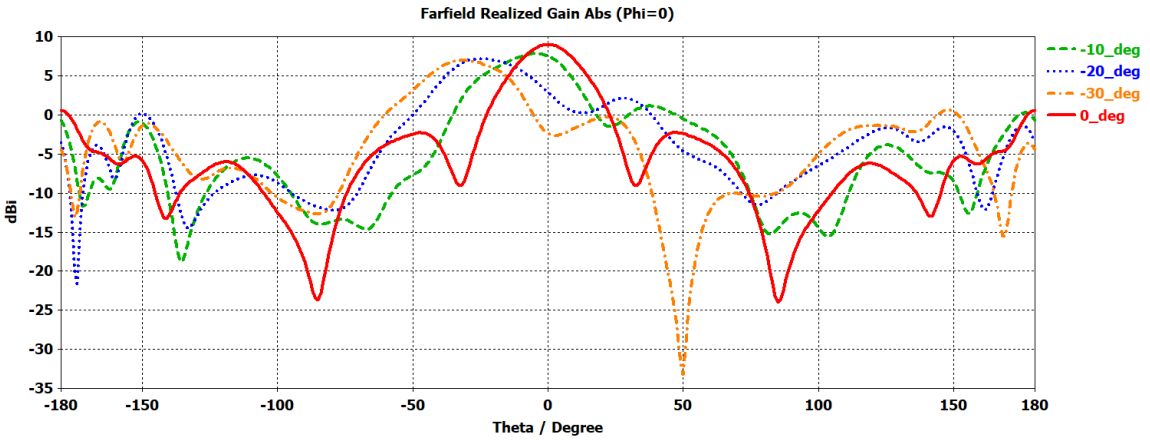

Figure 4.19 Beam steering of single slot CAA for left side

4.3 AiA in Connected slot Antenna Array System

5G mobile network has two allocated frequency bands, sub-6 GHz and mm-wave bands. Antenna-in-antenna concept is a new approach to achieve these two bands. Section 4.2 demonstrates the performance of single slot in the mm-wave band. Now, let's move from there, to resonant at sub-6 GHz, a very long slot has to cut in the upper side of the metal rim. To resonant at 3.5 GHz, the slot should be 37.5 mm long which will use a large aperture of the metal rim as in Figure 4.20. Practically, it is not viable to use such an antenna. Instead of a large slot, the aperture of existing mm-wave slot can be used along with additional slot to resonate at sub-6 GHz. The proposed structure is shown in Figure 4.21. The large slot required to resonant at 3.5 GHz is cut into half and by making a connecting slot, the mm-wave slot is connected to the sub-6 GHz slot. Now the whole slot will be used to resonate at 3.5 GHz where lower mm-wave slot will be resonant at mm-wave bands. To feed the 3.5 GHz slot antenna a separate microstrip feedline is used. To accommodate the new slot, feedline and mini-SMP, the length of the PCB board increased to 70 mm. By this

approach, a new AiA is proposed for 5G mobile handsets that can operate at both microwave and mm-wave bands. The shape looks like a cactus, so from now on it will be designated as cactus slot. The dimensions of the structure are given in Figure 4.21. In order to achieve better matching, a stub is used for the microwave slot. The prototype is fabricated and is shown in Figure 4.22. The whole structure of the wireless handset is illustrated in Figure 4.23. The overall size of the prototype is 147×72×8.4 mm^3 and the metal is 1mm thick.

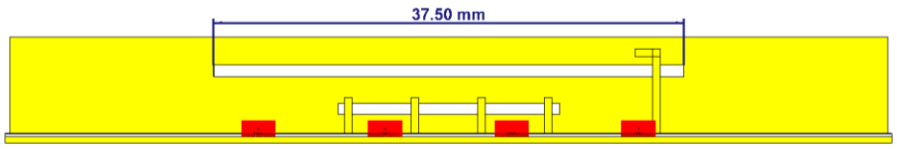

Figure 4.20 Separate slot for microwave band

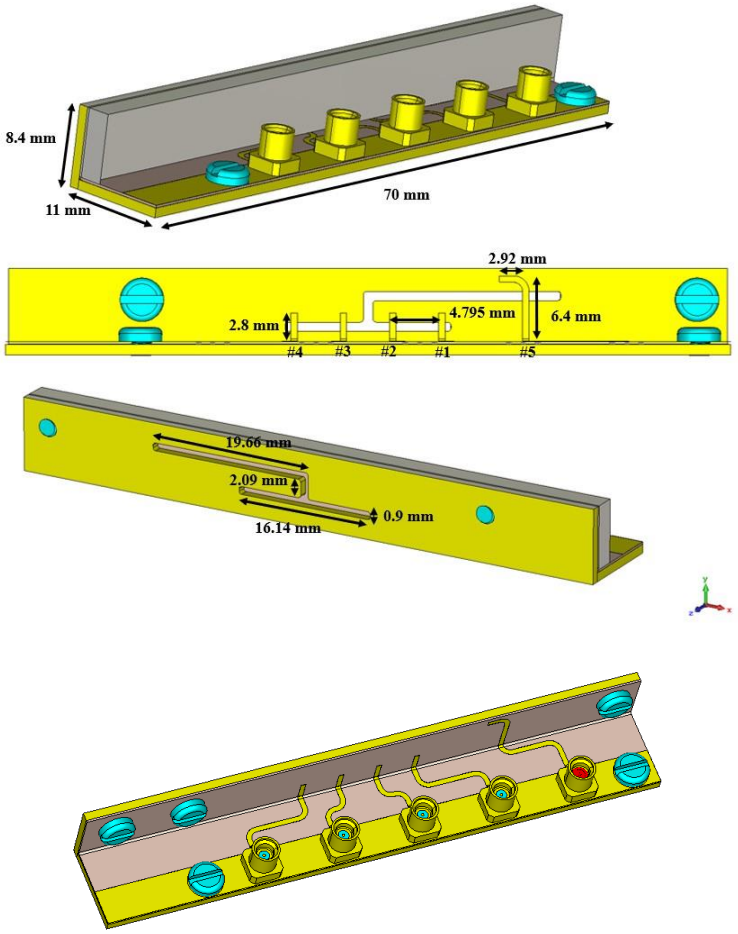

Figure 4.21 Structure of Cactus CSAA

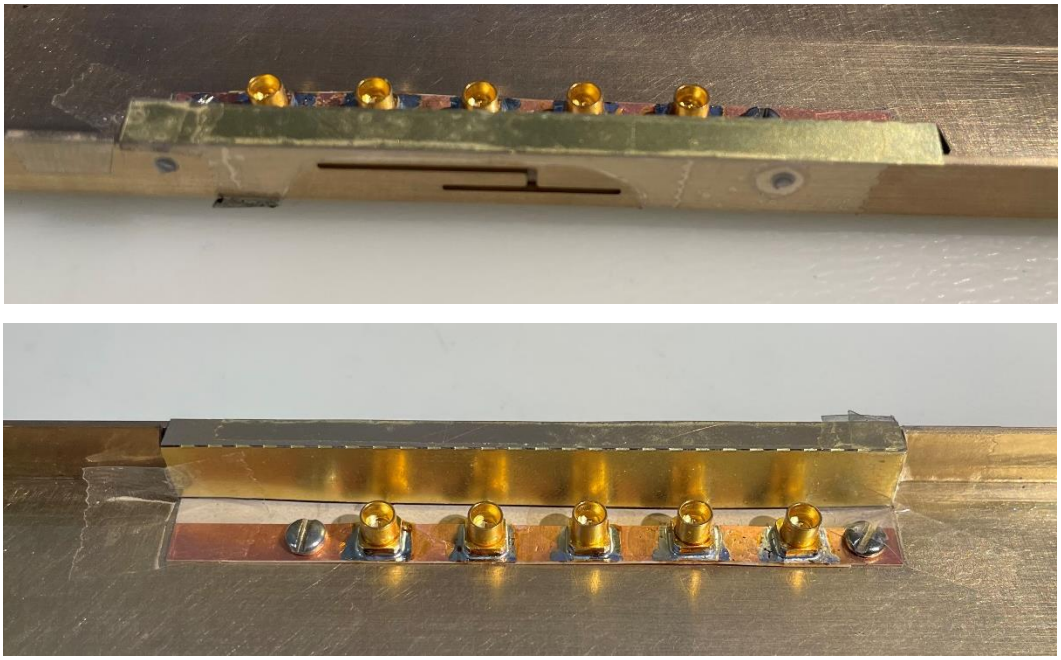

Figure 4.22 Fabricated prototype of Cactus CSAA

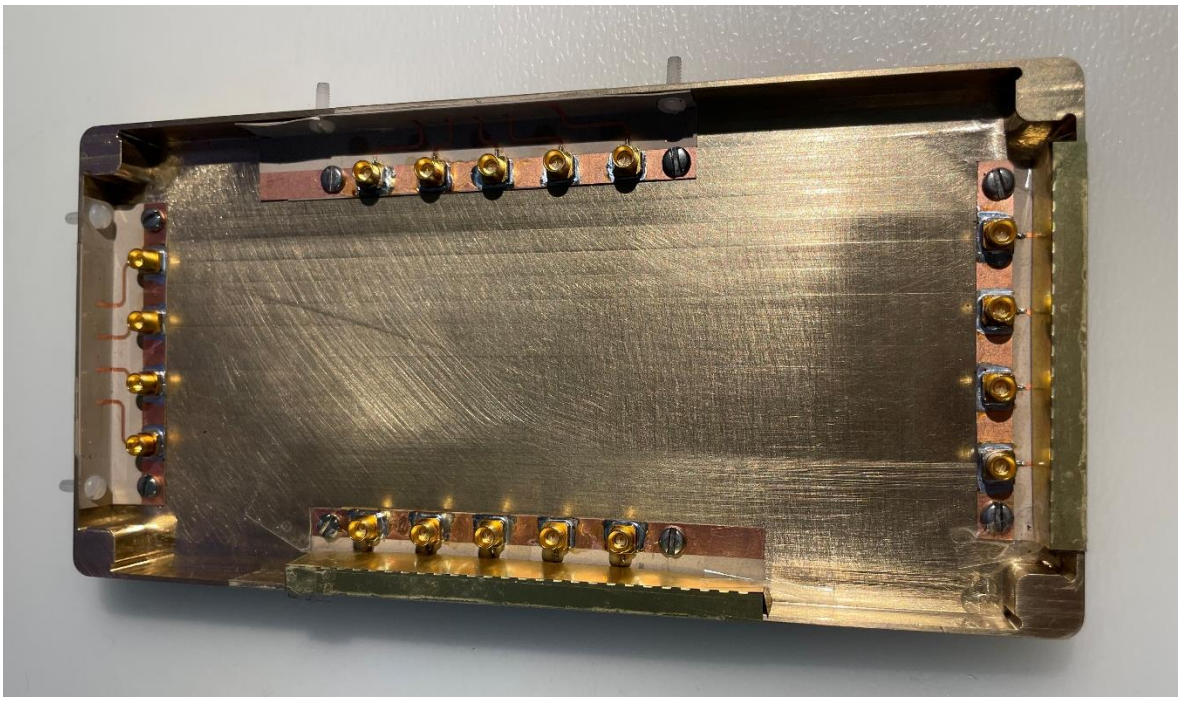

Figure 4.23 Fabricated prototype of the whole structure of wireless handset

4.3.1 mm-Wave S-Parameters

The simulation results of the S-parameters (S_{ij}) are presented in Figure 4.24(a). The simulated structure exhibits bandwidth ($S_{ij} < -10$ dB) of 3.71 GHz (26.32–30.03 GHz). The radiation and total efficiency are 93% and 75.63%, respectively at 28 GHz. For the measurement, port #1 is active and others are left open. Consequently, port #2, #3 and #4 are also measured. The measured S-parameters (S_{ij}) shows similar curves but because of fabrication tolerances and mounting issues, the resonant frequencies shifted in the case of feed #2 and #3 as in Figure 4.24(b). The same misalignment of the PCB board with the metal frame slot and the air gap in between them are affecting the measured results.

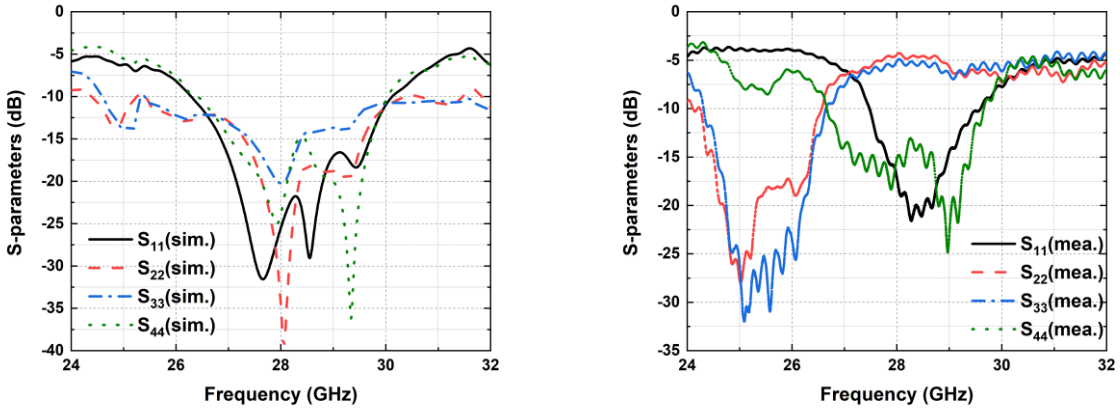

(a) (b)

Figure 4.24 S-parameters of Cactus CSAA (a) Simulated and (b) Measured

The isolation curves of Cactus CSAA are shown in Figure 4.25. The worse case isolation is around -8 dB at 28 GHz. The principle of CAA is to make the antenna elements connected because of that low isolation is expected in this structure.

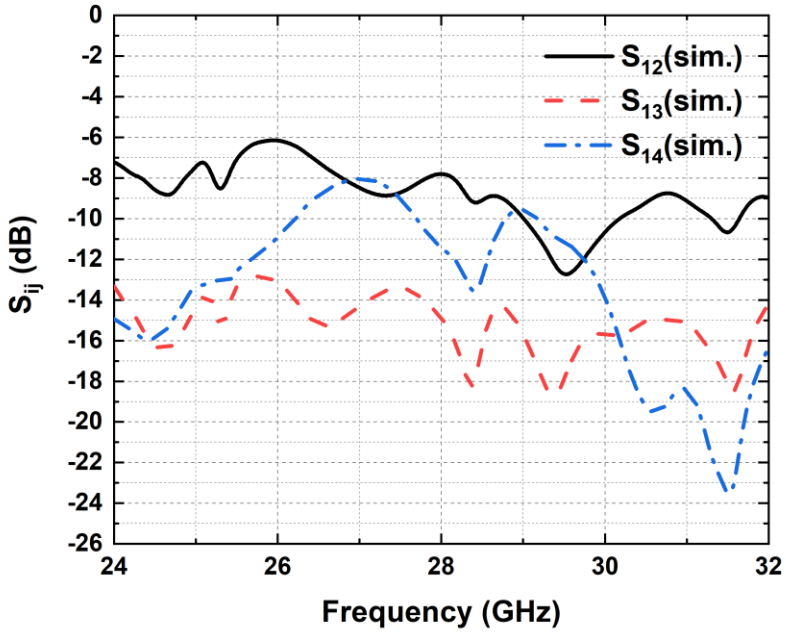

Figure 4.25 Isolation curves of Cactus CSAA

4.3.2 Tuning the design and backing reflector

To minimize the effect of BR and improve the proper connectivity with the metal frame, the BR of the structure is redesigned as shown in Figure 4.26. The BR length is now shortened (56 mm), and an arm is extended on both sides so that it can be placed tight with the existing screw the structure already has. This will increase the stability and the proper ground connection from the top side with the frame. All the other parameters are unchanged.

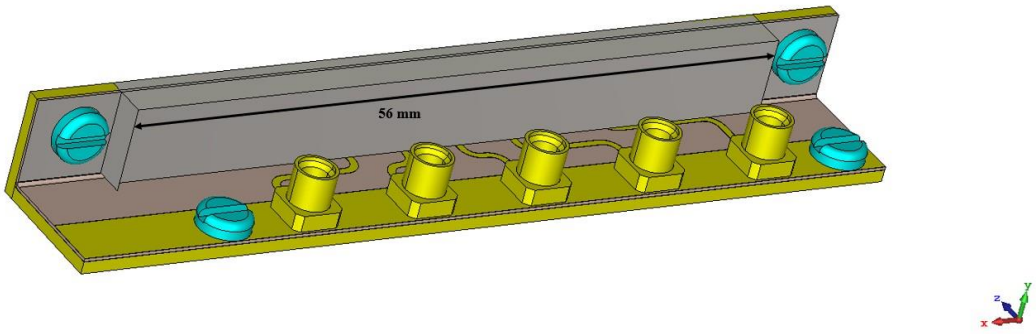

Figure 4.26 Geometry of cactus CSAA with new BR

4.3.3 Second measurement attempt

The simulation and measured results of the new structure are presented in Figure 4.27. For the measurement, port #1 is active and others are left open. Consequently, port #2, #3 and #4 are also measured. The simulated structure exhibits bandwidth (S_{ij} < −10 dB) of 3.27 GHz (26.64–29.91 GHz) as in Figure 4.27(a). But the measured results still have the matching issues for port #2 and #3, as discussed in the previous section, this is contributing from the alignment and air gap between metal frame and PCB board. The results can be improved further with proper alignment with the metal frame and good ground connection. The new fabricated prototype is shown in Figure 4.28.

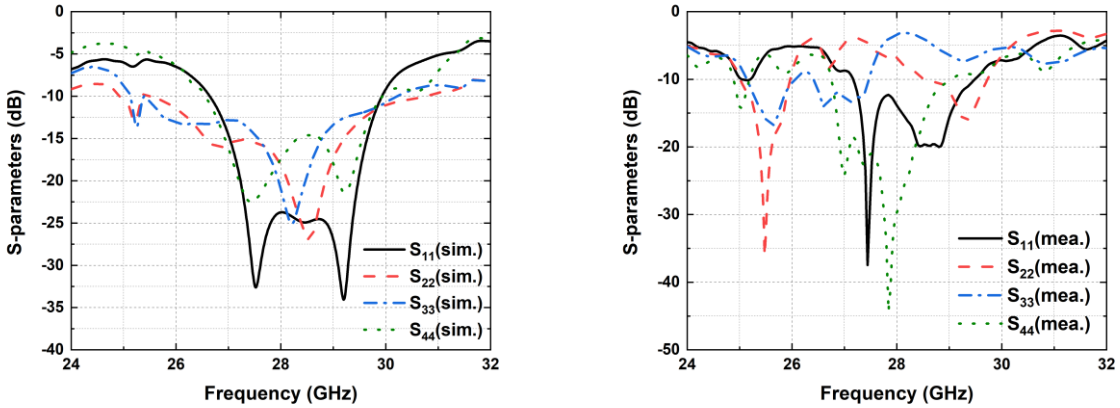

(a) (b)

Figure 4.27 S-parameters of cactus CSAA with new BR (a) simulated and (b) measured

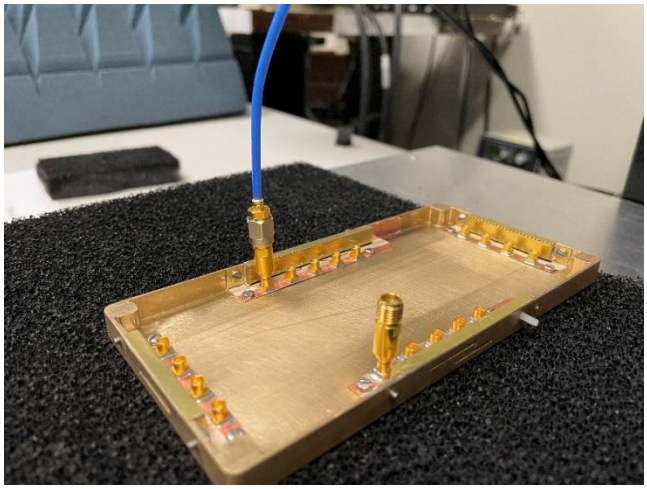

Figure 4.28 Fabricated and measurement setup of cactus CSAA with new BR

4.3.4 Radiation Patterns

From the radiation pattern plotted in Figure 4.29, similar behavior is expected as section 4.2.4. A 7.76 dBi of realized gain is observed at 28 GHz and the SLL is now -10.3 dB. There is a 1.18 dBi drop in realized gain which is coming from the introduction of new microwave antenna and the design is optimized for this case. The main beam direction is directed to 0°.

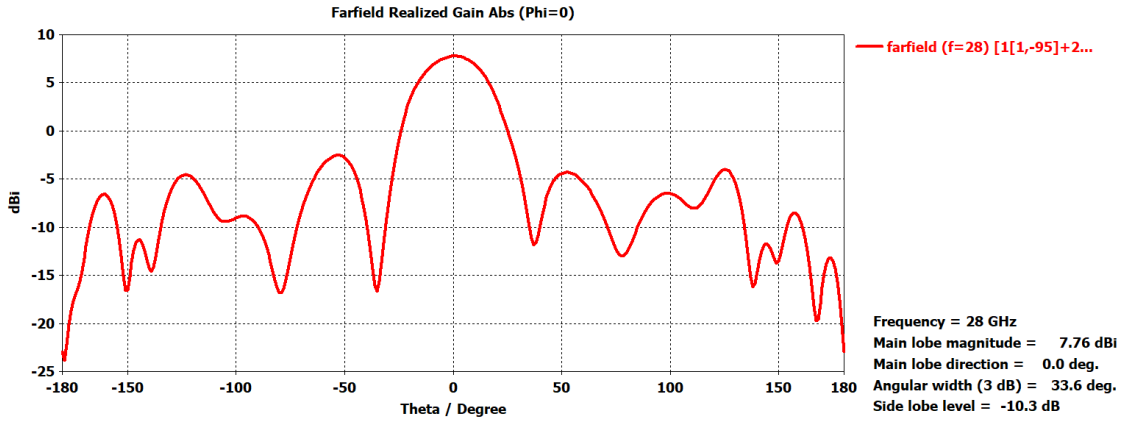

Figure 4.29 Radiation patterns of Cactus CSAA at 28 GHz phi 0° cut

4.3.5 Beamsteering of Cactus CSAA

Similar to section 4.2.5, the results obtained from the simulation are presented in Table 4.5 and 4.6. The feedline length of feed #1 and #4 are equal and feed #2 and #3 are equal. But the length of feed #1 and #4 is 16.3 mm and feed #2 and #3 is 11.5 mm. So, the phase of the feedlines needs to calculate and compensate to get desired beam steering. The calculated phase of feed #1 and #4 is 125° and for feed #2 and #3 is about 30°. To make the calculation simple, the feed #2 and #3 are kept 0° and feed #1 and #4 to 95°. For element 4, -95° has to add with the calculated phases. The presence of the connecting slot that connect the microwave and mm-wave slot, also the structure is not symmetric, which eventually affects the beam at -10°, the beam steered up to -6° and the realized gain and SLL are also affected.

Table 4.5 Progressive phase shift for the cactus CSAA at each feeding point

Desired beam towards	**Element 1**	**Element 2**	**Element 3**	**Element 4**
$\theta=0^o$	0	0	0	0
$\theta=\pm10^o$	0	-27.4	-54.8	-82.2
$\theta=\pm20^o$	0	-54.8	-109.6	-164.4
$\theta=\pm30^o$	0	-80.56	-161.12	-241.68

Table 4.6 Beam steering for cactus CSAA

Progressive Phase Shift	**Desired θ**	**Element 1**	**Element 2**	**Element 3**	**Element 4**	**Obtained θ**	**Realized Gain (dBi)**	**SLL (dB)**
β	0^o	-95	0	0	-95	0^o	7.76	-10.3
β	$+10^o$ -10^o	-95 -95	-27.4 +27.4	-54.8 +54.8	-177.2 -12.8	$+8^o$ -6^o	7.26 6.83	-8.8 -7.2
β	$+20^o$ -20^o	-95 -95	-54.8 +54.8	-109.6 +109.6	-259.4 +69.4	$+26^o$ -26^o	7.34 6.54	-7.5 -6.7
β	$+30^o$ -30^o	-95 -95	-80.56 +80.56	-161.12 +161.12	-336.68 +146.68	$+30^o$ -30^o	7.62 7.15	-6.2 -5.4

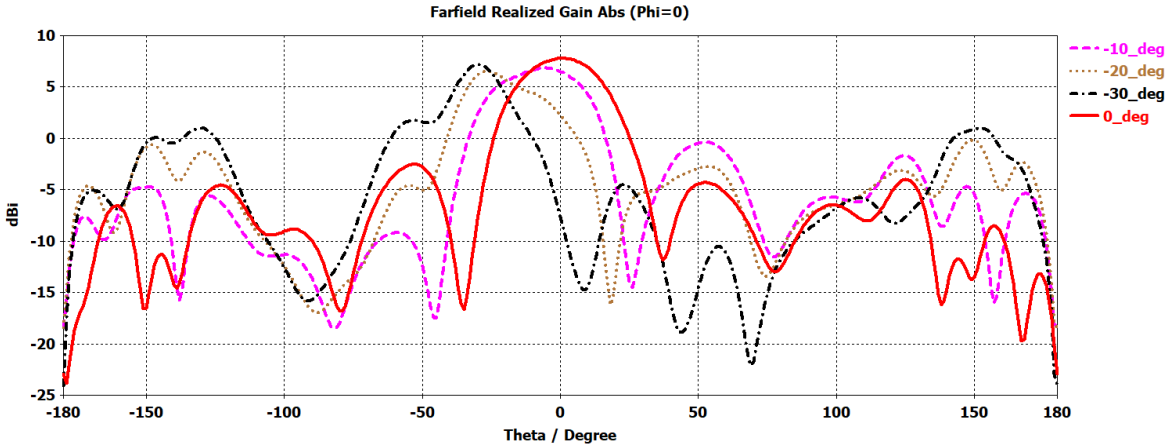

(a)

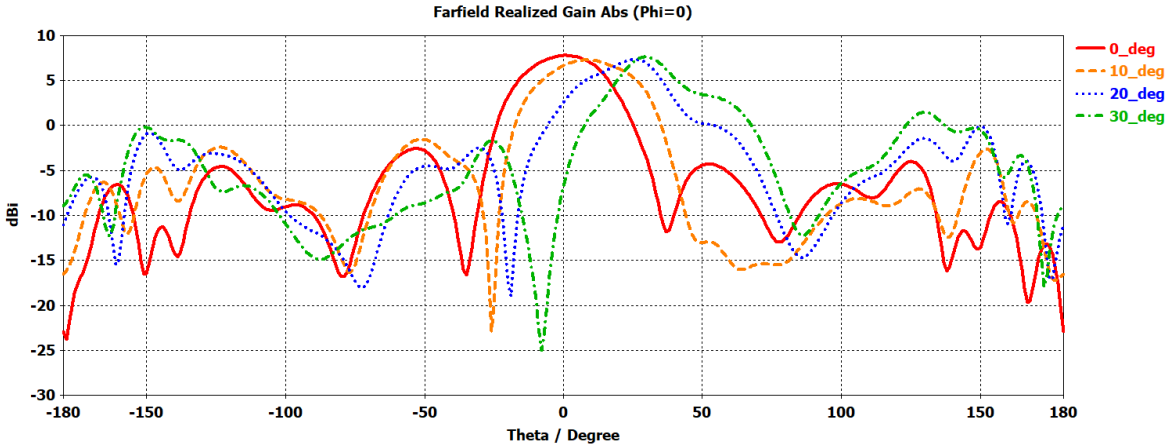

(b)

Figure 4.30 Beam steering of Cactus CSAA (a) Left and (b) Right

The beam patterns for both left and right side are illustrated in Figure 4.30. From the results, we can observe that the beam can be steered up to 30^{o}. After that, the realized gain drops dramatically, and the SLL also increases.

4.3.6 Microwave Performance of Cactus CSAA

The simulation and measured results of the S_{11} are presented in Figure 4.31. The simulated structure exhibits bandwidth ($S_{11} < -10$ dB) of 60 MHz (3.47–3.53 GHz). The radiation and total efficiency are 93.28% and 92.5%, respectively at 3.5 GHz. The measured S_{11} is not similar to the simulated

one because of fabrication tolerances and mounting issues, the matching is not good, and the resonant frequency shifted to 3.4 GHz.

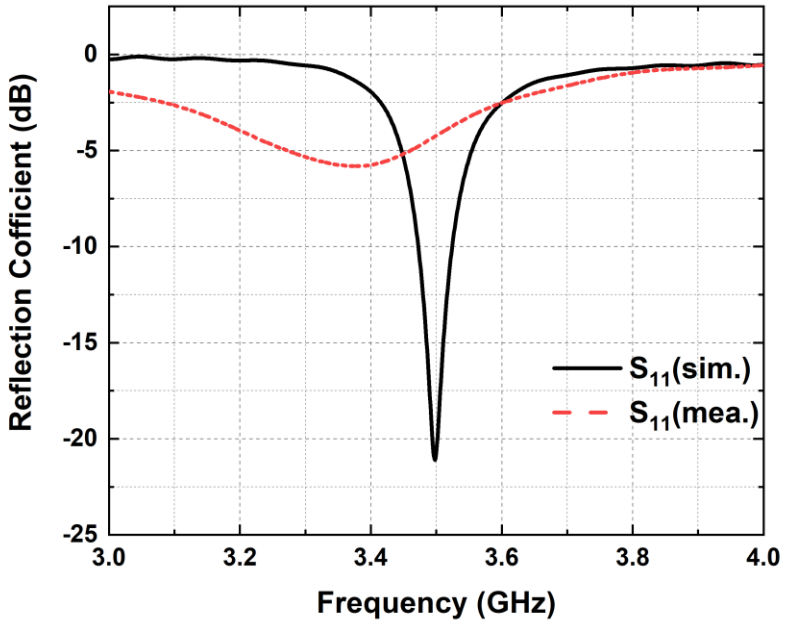

Figure 4.31 Simulated and measured S_{11} of Cactus CSAA

The current distribution of the Cactus CSAA is shown in Figure 4.32. As we can see that, when port #5 is excited, the current is circulated in all the aperture of the cactus slot. Which eventually leads to sub-6 GHz. And when port #1 to #4 are excited, the current in the upper slot is not strong rather the current is trapped in the lower slot of the structure.

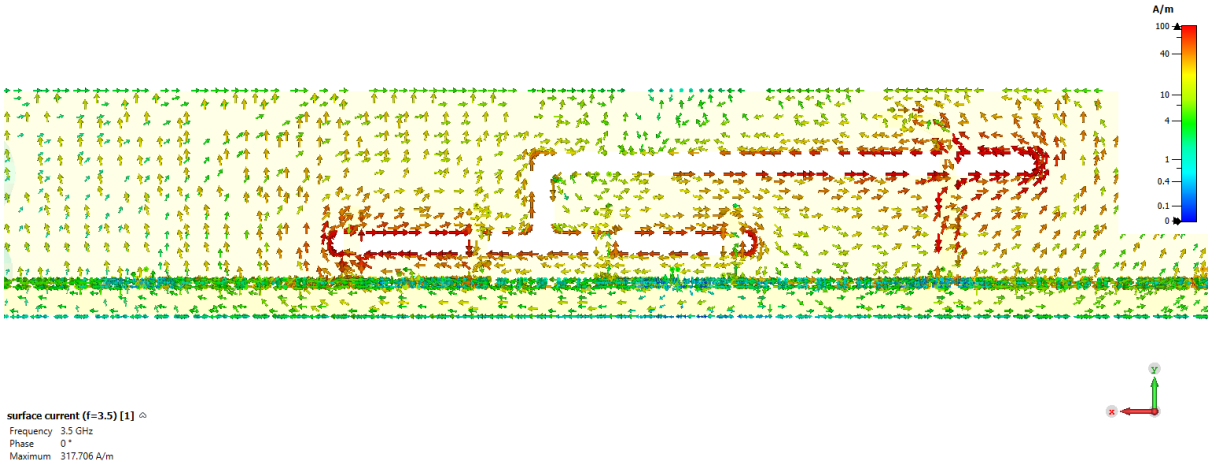

(a)

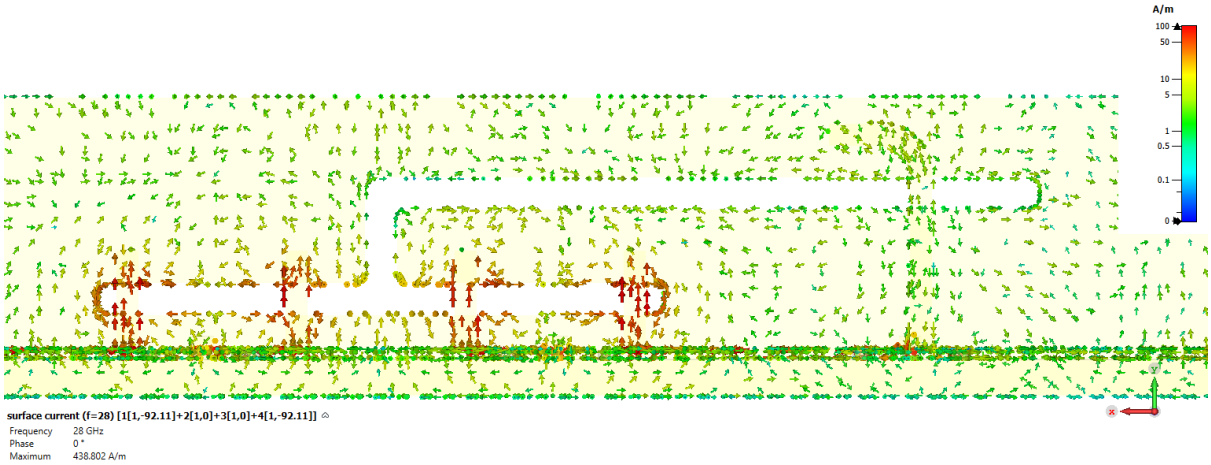

(b)

Figure 4.32 Current distribution of Cactus CSAA (a) when port #5 is active and (b) when port #1 #2 #3 #4 are active

The 3D radiation pattern of the structure is shown in Figure 4.33. The realized gain is 4.68 dBi. Here, a tilt in the beam is observed because of the ground base of the mobile frame. The BR here is designed and placed is for the mm-wave band at 28 GHz. At 3.5 GHz the wavelength is very long so it cannot see it as a BR. The tilt of the beam can be fixed by extending the upper BR plane which mimic the screen of the phone in real environment as in Figure 4.34.

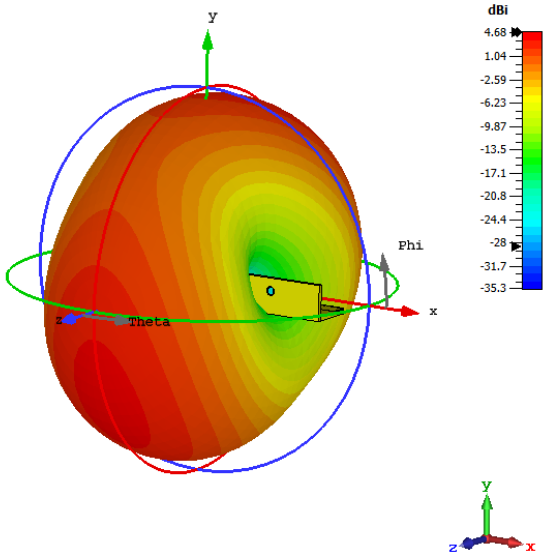

Figure 4.33 3D Radiation Pattern at 3.5 GHz

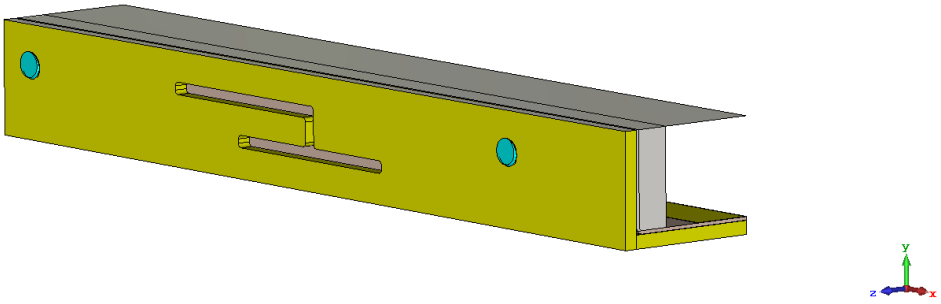

Figure 4.34 Extended BR of Cactus CSAA at 3.5 GHz

After adding the extension, the slot and feedline of the microwave structure have to optimized to resonate at 3.5 GHz. By playing with the slot length of microwave slot, it can be resonant at any frequency in the sub-6 GHz. The S_{11} of the optimized structure is plotted in Figure 4.35. Now, the simulated structure exhibits bandwidth ($S_{11} < -10$ dB) of 110 MHz (3.45–3.56 GHz). The radiation and total efficiency are 96.07% and 96.02%, respectively at 3.5 GHz.

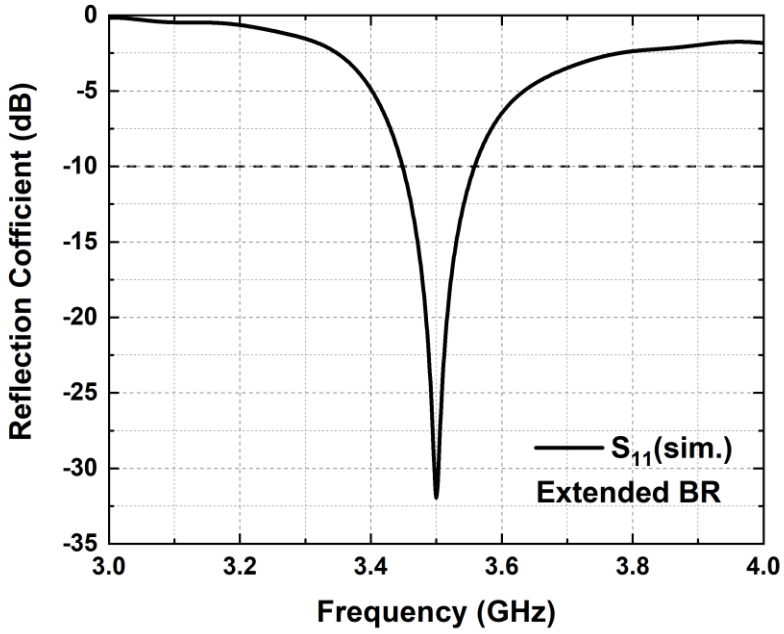

Figure 4.35 S_{11} of Extended BR of Cactus CSAA

The 3D radiation pattern of the structure after extending the BR in upper side is shown in Figure 4.36. As we can see, the main beam is now directed at +z direction without any tilt.

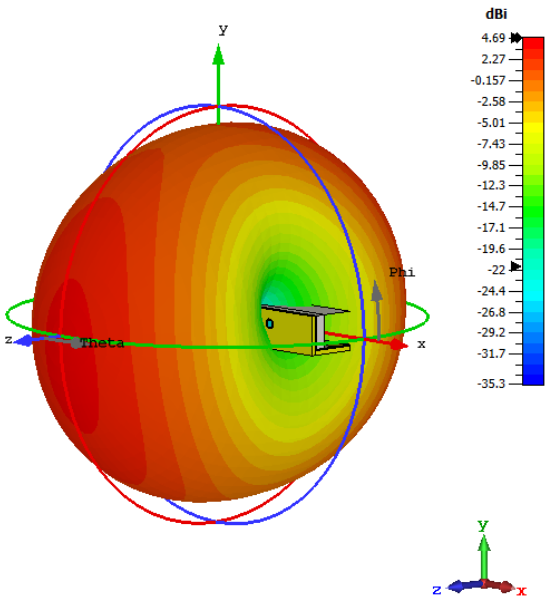

Figure 4.36 3D Radiation Pattern at 3.5 GHz after Extended BR

After the new BR as discussed in section 4.3.2, the simulated and measured results of cactus CSAA is shown in Figure 4.37. the resonant frequency is shifted to 3.34 GHz and new resonance is appeared which is above -10 dB at 3.6 GHz. The bandwidth is only 20 MHz. In the measurement, similar pattern is observed but with a shift. it is resonating at 3.69 GHz and 4.6 GHz, but the bandwidth is now 350 MHz.

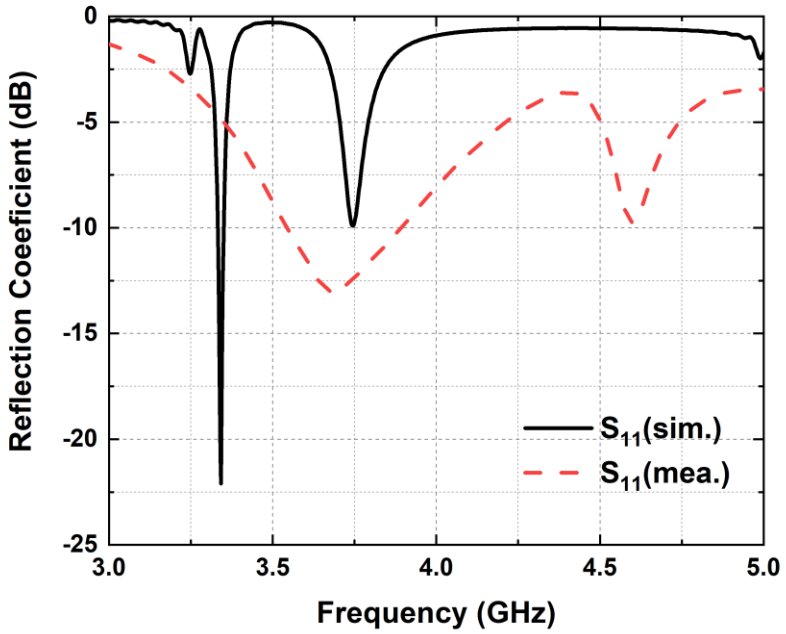

Figure 4.37 Simulated and measured S_{11} of Cactus CSAA with new BR

4.4 Conclusion

In this work, a compact connected slot antenna array is proposed. The developed system operated between 26.23–30.46 GHz using single slot and 26.64–29.91 GHz using cactus slot targets portable wireless headsets. The unique feature of the proposed system is its ability to provide wide bandwidth, high gain and beamsteering capabilities for mmWave simultaneously. A complete antenna system based on antenna in antenna concept is proposed for both microwave and mmWave bands for 5G. The system exhibits 110 MHz of bandwidth at 3.5 GHz in the microwave band. During the measurement, because of the alignment and air gap issue, the measured results is not matched with simulation at some cases. The proposed system is compact, targeting both lower and

higher frequency bands of practical wireless devices and highly suitable to be used in handheld smartphone devices.

CHAPTER 5 CONCLUSION AND FUTURE WORK

5.1 Conclusion

This work was started with the design of connected slot antenna array (CSAA) for portable wireless handsets. The slot antenna based on CAA concept has been developed with optimized dimensions, targeting 28 GHz mmWave frequency band of operation with unique feature of wide broadband, space utilization and beam steering capabilities for upcoming 5G mobile phones. Initially, four elements single CSAA on metal rim has been investigated with beamsteering capabilities up to ±40^o in broadside direction.

In the first design, a single slot is cut in the middle of a metal structure which represents a standard metal frame of a smartphone handset. The slot antenna was designed implementing the concept of connected antenna array (CAA) for 1×4 elements with four microstrip feedlines. The rogers RO3003 substrate is used, and a backing reflector (BR) is placed at λ/4 behind the single slot CAA. The overall PCB board has a dimension of 17.13×50×0.25 mm^3 with the slot size was only 17.77×2 mm^2. The substrate was bend to 90^o to accommodate in the mobile phone frame. The practical scenario was considered during the design process of the antenna. The structure exhibits bandwidth (S_{ij} < −10 dB) of 4.23 GHz (26.23–30.46 GHz) with a total efficiency of 86.1%. The worst-case isolation was below -8 dB and a realized gain of 8.94 dBi was observed in single CAA system. The beam can be steered up to 31^o in this design.

In the second design, Antenna-in-antenna (AiA) concept was implemented to achieve sub-6 GHz and mm-wave bands for 5G. The aperture of existing mm-wave slot was used along with additional slot to resonate at sub-6 GHz. The large slot required to resonant at 3.5 GHz is cut into half and by making a connecting slot, the mm-wave slot is connected to the sub-6 GHz slot. The whole cactus slot was used to resonate at 3.5 GHz where lower mm-wave slot was used to resonant at mm-wave bands. To feed the 3.5 GHz slot antenna a separate microstrip feedline was used with a stub. The structure exhibits bandwidth (S_{ij} < −10 dB) of 3.27 GHz (26.64–29.91 GHz) and the total efficiency was 75.17% at 28 GHz. The worst-case isolation was around -8 dB and the realized gain was 7.73 dBi. The beam can be steered up to 30^o in this design. For the microwave band, the bandwidth (S_{11} < −10 dB) of 110 MHz (3.45–3.56 GHz) with 4.69 dBi realized gain were achieved.

The demonstrated CSAA systems are good candidates for prospective 5G wireless handsets where both frequency bands can be used along with the beamsteering capabilities.

5.2 Future Work

In spite of the fact that design of compact, low profile integrated microwave and mm-wave antenna system is still a challenging task to the researchers, there are some research themes of the present work that could benefit a further in-depth investigation. The suggestions for the further improvements of this research are as follows:

- The bandwidth of the microwave band can be improved by utilizing the reconfigurable feeding technique for 5G applications.
- The beamsteering capabilities can be improved by design modification with more capable fabrication facility.
- The prototype can be utilized in MIMO application to meet the high data rate and reliability requirements.
- The develop model can be analyzed with the whole integrated system along with hand and head analysis.

REFERENCES

[1] Larsson, E.G. and Van der Perre, L., 2017. Massive MIMO for 5G. IEEE 5G Tech Focus, 1(1).

[2] https://www.3gpp.org.

[3] P. Rysavy, "Transition to 4G: 3GPP Broadband Evolution to IMT-Advanced," 3G Americas, Web. http://4g5gworld.com/whitepaper/transition-4g-3gpp-broadband-evolution-imt-advanced.

[4] Cavallo, D., et al. 2012. A 3-to 5-GHz wideband array of connected dipoles with low cross polarization and wide-scan capability. IEEE Transactions on A&P, 61(3), pp.1148-1154.

[5] "Cisco Annual Internet Report (2018–2023)," Cisco Visual Networking, White Paper, 2020.

[6] "5G Spectrum Public Policy Position" Huawei, February 2020.

[7] [7] Balanis, C.A., 2015. Antenna theory: analysis and design. John wiley & sons.

[8] R. C. Hansen, Phased Array Antennas, John Wiley & sons, 2009.

[9] D. Cavallo, Connected Array antennas: Analysis and design, PhD thesis, TNO, The Haguue, The Netherlands 2011.

[10] J. J. Lee, "Effects of metal fences on the scan performance of an infinite dipole array," IEEE Trans. Antennas Propag., vol. 38, pp. 683–692, 1990.

[11] Neto, A. and Lee, J.J., 2006. Ultrawide-band properties of long slot arrays. IEEE transactions on antennas and propagation, 54(2), pp.534-543.

[12] J. J. Lee, S. Livingstone, and R. Koenig, "Wide band slot array Antennas," in Proc.AP- S Symp., vol. 2, Columbus, OH, June 2003, pp. 452–455.

[13] J. J. Lee, S. Livingstone, and R. Koenig, "Wide band slot array Antennas," in Proc.AP- S Symp., vol. 2, Columbus, OH, June 2003, pp. 452–455.

[14] https://www.fcc.gov/5G

[15] Q. Chen, H. Lin, J. Wang, L. Ge, Y. Li, and T. Pei, "Single ring slot-based antennas for metal-rimmed 4G/5G smartphones," IEEE Transactions on Antennas and Propagation, vol. 67, no. 3, pp. 1476-1487, 2018.

[16] Q. Guo, R. Mittra, F. Lei, Z. Li, J. Ju, and J. Byun, "Interaction between internal antenna and external antenna of mobile phone and hand effect," IEEE Transactions on Antennas and Propagation, vol. 61, no. 2, pp. 862-870, 2012.

[17] M. Stanley, Y. Huang, H. Wang, H. Zhou, Z. Tian, and Q. Xu, "A novel reconfigurable metal rim integrated open slot antenna for octa-band smartphone applications," IEEE Transactions on Antennas and Propagation, vol. 65, no. 7, pp. 3352-3363, 2017.

[18] J. Choi, W. Hwang, C. You, B. Jung, and W. Hong, "Four-element reconfigurable coupled loop MIMO antenna featuring LTE full-band operation for metallic-rimmed smartphone," IEEE Transactions on Antennas and Propagation, vol. 67, no. 1, pp. 99-107, 2018.

[19] J. Duan, K. Xu, X. Li, S. Chen, P. Zhao, and G. Wang, "Dual-band and enhanced-isolation MIMO antenna with L-shaped meta-rim extended ground stubs for 5G mobile handsets," International Journal of RF and Microwave Computer-Aided Engineering, vol. 29, no. 8, p. e21776, 2019.

[20] B. Yu, K. Yang, and G. Yang, "A novel 28 GHz beam steering array for 5G mobile device with metallic casing application," IEEE Transactions on Antennas and Propagation, vol. 66, no. 1, pp. 462-466, 2017.

[21] R. Rodriguez-Cano, S. Zhang, K. Zhao, and G. F. Pedersen, "mm-Wave beam-steerable endfire array embedded in a slotted metal-frame LTE antenna," IEEE Transactions on Antennas and Propagation, vol. 68, no. 5, pp. 3685-3694, 2020.

[22] J. Choi et al., "Frequency-adjustable planar folded slot antenna using fully integrated multithrow function for 5G mobile devices at millimeter-wave spectrum," IEEE Transactions on Microwave Theory and Techniques, vol. 68, no. 5, pp. 1872-1881, 2020.

[23] R. M. Moreno et al., "Dual-polarized mm-Wave end-fire chain-slot antenna for mobile devices," IEEE Transactions on Antennas and Propagation, 2020.

[24] R. M. Moreno, J. Ala-Laurinaho, and V. Viikari, "Dual-Polarized mm-Wave Antenna Solution for Mobile Phone," in 2020 14th European Conference on Antennas and Propagation (EuCAP), 2020, pp. 1-5: IEEE.

[25] R. M. Moreno, J. Ala-Laurinaho, A. Khripkov, J. Ilvonen, and V. Viikari, "Dual-polarized mm-wave endfire antenna for mobile devices," IEEE Transactions on Antennas and Propagation, vol. 68, no. 8, pp. 5924-5934, 2020.

[26] C. Deng, Z. Feng, and S. V. Hum, "MIMO mobile handset antenna merging characteristic modes for increased bandwidth," IEEE Transactions on Antennas and Propagation, vol. 64, no. 7, pp. 2660-2667, 2016.

[27] Y. Yan, Y.-L. Ban, and G. Wu, "Dual-loop antenna with band-stop matching circuit for WWAN/LTE full metal-rimmed smartphone application," IET Microwaves, Antennas & Propagation, vol. 10, no. 15, pp. 1715-1720, 2016.

[28] M. Ikram, E. Al Abbas, N. Nguyen-Trong, K. H. Sayidmarie, and A. Abbosh, "Integrated frequency-reconfigurable slot antenna and connected slot antenna array for 4G and 5G mobile handsets," IEEE Transactions on Antennas and Propagation, vol. 67, no. 12, pp. 7225-7233, 2019.

[29] A. Ren and Y. Liu, "A compact building block with two shared-aperture antennas for eight-antenna MIMO array in metal-rimmed smartphone," IEEE Transactions on Antennas and Propagation, vol. 67, no. 10, pp. 6430-6438, 2019.

[30] L.-W. Zhang, Y.-L. Ban, J. Guo, and Z.-F. Yu, "Parallel dual-loop antenna for WWAN/LTE metal-rimmed smartphone," IEEE Transactions on Antennas and Propagation, vol. 66, no. 3, pp. 1217-1226, 2018.

[31] L. Sun, Y. Li, Z. Zhang, and Z. Feng, "Wideband 5G MIMO antenna with integrated orthogonal-mode dual-antenna pairs for metal-rimmed smartphones," IEEE Transactions on Antennas and Propagation, vol. 68, no. 4, pp. 2494-2503, 2019.

[32] C. Di Paola, S. Zhang, K. Zhao, Z. Ying, T. Bolin, and G. F. Pedersen, "Wideband beam-switchable 28 GHz quasi-Yagi array for mobile devices," IEEE Transactions on Antennas and Propagation, vol. 67, no. 11, pp. 6870-6882, 2019.

[33] H. A. Diawuo and Y.-B. Jung, "Broadband proximity-coupled microstrip planar antenna array for 5G cellular applications," IEEE Antennas and Wireless Propagation Letters, vol. 17, no. 7, pp. 1286-1290, 2018.

[34] S. Zhang, X. Chen, I. Syrytsin, and G. F. Pedersen, "A planar switchable 3-D-coverage phased array antenna and its user effects for 28-GHz mobile terminal applications," IEEE Transactions on Antennas and Propagation, vol. 65, no. 12, pp. 6413-6421, 2017.

[35] Q. Wu, J. Hirokawa, J. Yin, C. Yu, H. Wang, and W. Hong, "Millimeter-wave multibeam endfire dual-circularly polarized antenna array for 5G wireless applications," IEEE transactions on antennas and propagation, vol. 66, no. 9, pp. 4930-4935, 2018.

[36] S. Zhu, H. Liu, Z. Chen, and P. Wen, "A compact gain-enhanced Vivaldi antenna array with suppressed mutual coupling for 5G mmWave application," IEEE Antennas and Wireless Propagation Letters, vol. 17, no. 5, pp. 776-779, 2018.

[37] S. X. Ta, H. Choo, and I. Park, "Broadband printed-dipole antenna and its arrays for 5G applications," IEEE Antennas and Wireless Propagation Letters, vol. 16, pp. 2183-2186, 2017.

[38] D.-y. Kim, J. W. Lee, C. S. Cho, and T. K. Lee, "Design of a compact tri-band PIFA based on independent control of the resonant frequencies," IEEE Transactions on Antennas and Propagation, vol. 56, no. 5, pp. 1428-1436, 2008.

[39] H. F. AbuTarboush, R. Nilavalan, T. Peter, and S. Cheung, "Multiband inverted-F antenna with independent bands for small and slim cellular mobile handsets," IEEE Transactions on Antennas and Propagation, vol. 59, no. 7, pp. 2636-2645, 2011.

[40] C.-H. Chang and K.-L. Wong, "Printed $\lambda/8$-PIFA for Penta-Band WWAN Operation in the Mobile Phone," IEEE Transactions on Antennas and Propagation, vol. 57, no. 5, pp. 1373-1381, 2009.

[41] Y. L. Kuo and K. L. Wong, "Coplanar waveguide-fed folded inverted-F antenna for UMTS application," Microwave and optical technology letters, vol. 32, no. 5, pp. 364-366, 2002.

[42] J.-H. Chen, C.-J. Ho, C.-H. Wu, S.-Y. Chen, and P. Hsu, "Dual-band planar monopole antenna for multiband mobile systems," IEEE Antennas and Wireless Propagation Letters, vol. 7, pp. 769-772, 2008.

[43] C.-M. Peng, I.-F. Chen, and C.-T. Chien, "A novel hexa-band antenna for mobile handsets application," IEEE transactions on antennas and propagation, vol. 59, no. 9, pp. 3427-3432, 2011.

[44] Z.-Q. Xu, Y.-T. Sun, Q.-Q. Zhou, Y.-L. Ban, Y.-X. Li, and S. S. Ang, "Reconfigurable MIMO antenna for integrated-metal-rimmed smartphone applications," IEEE Access, vol. 5, pp. 21223-21228, 2017.

[45] H.-B. Zhang, Y.-L. Ban, Y.-F. Qiang, J. Guo, and Z.-F. Yu, "Reconfigurable loop antenna with two parasitic grounded strips for WWAN/LTE unbroken-metal-rimmed smartphones," IEEE Access, vol. 5, pp. 4853-4858, 2017.

[46] Y.-L. Ban, Y.-F. Qiang, G. Wu, H. Wang, and K.-L. Wong, "Reconfigurable narrow-frame antenna for LTE/WWAN metal-rimmed smartphone applications," IET Microwaves, Antennas & Propagation, vol. 10, no. 10, pp. 1092-1100, 2016.

[47] J. Zhang, S. Zhang, Z. Ying, A. S. Morris, and G. F. Pedersen, "Radiation-pattern reconfigurable phased array with pin diodes controlled for 5G mobile terminals," IEEE Transactions on Microwave Theory and Techniques, vol. 68, no. 3, pp. 1103-1117, 2019.

[48] R. Luomaniemi, J.-M. Hannula, A. Lehtovuori, and V. Viikari, "Switch-reconfigurable metal rim MIMO handset antenna with distributed feeding," IEEE Access, vol. 7, pp. 48971-48981, 2019.

[49] P. Hindle, "The state of RF/microwave switches," microwave journal, vol. 53, no. 11, pp. 20-36, 2010.

[50] G. M. Rebeiz and J. B. Muldavin, "RF MEMS switches and switch circuits," IEEE Microwave magazine, vol. 2, no. 4, pp. 59-71, 2001.

[51] J. Kurvinen et al., "Capacitively-loaded feed line to improve mm-wave and sub-6 GHz antenna co-existence," IEEE Access, vol. 8, pp. 139680-139690, 2020.

[52] M. S. Sharawi, M. Ikram, and A. Shamim, "A two concentric slot loop based connected array MIMO antenna system for 4G/5G terminals," IEEE Transactions on antennas and propagation, vol. 65, no. 12, pp. 6679-6686, 2017.

[53] M. Ikram, R. Hussain, and M. S. Sharawi, "4G/5G antenna system with dual function planar connected array," IET Microwaves, Antennas & Propagation, vol. 11, no. 12, pp. 1760-1764, 2017.

[54] C. Lee, M. K. Khattak, and S. Kahng, "Wideband 5G beamforming printed array clutched by LTE-A 4× 4-multiple-input–multiple-output antennas with high isolation," IET Microwaves, Antennas & Propagation, vol. 12, no. 8, pp. 1407-1413, 2018.

[55] J. Kurvinen, H. Kähkönen, A. Lehtovuori, J. Ala-Laurinaho, and V. Viikari, "Co-designed mm-wave and LTE handset antennas," IEEE Transactions on antennas and propagation, vol. 67, no. 3, pp. 1545-1553, 2018.

[56] M. Ikram, M. Sharawi, A. Shamim, and A. Sebak, "A multiband dual-standard MIMO antenna system based on monopoles (4G) and connected slots (5G) for future smart phones," Microwave and Optical Technology Letters, vol. 60, no. 6, pp. 1468-1476, 2018.

[57] R. Hussain, A. T. Alreshaid, S. K. Podilchak, and M. S. Sharawi, "Compact 4G MIMO antenna integrated with a 5G array for current and future mobile handsets," IET Microwaves, Antennas & Propagation, vol. 11, no. 2, pp. 271-279, 2017.

[58] J. Lan, Z. Yu, J. Zhou, and W. Hong, "An aperture-sharing array for (3.5, 28) GHz terminals with steerable beam in millimeter-wave band," IEEE Transactions on Antennas and Propagation, vol. 68, no. 5, pp. 4114-4119, 2019.

[59] X.-H. Ding, W.-W. Yang, W. Qin, and J.-X. Chen, "A Broadside Shared-aperture Antenna for (3.5, 26) GHz Mobile Terminals with Steerable Beam in Millimeter Wave Band," IEEE Transactions on Antennas and Propagation, 2021.

[60] Y. Wang, H.-C. Huang, and X. Jian, "Novel design of a dual-band 5G mm-Wave antenna array integrated with a metal frame of a cellular phone," in 2018 Asia-Pacific Microwave Conference (APMC), 2018, pp. 1582-1584: IEEE.

[61] H.-C. Huang, Y. Wang, and X. Jian, "Novel integrated design of dual-band dual-polarization mm-wave antennas in non-mm-wave antennas (AiA) for a 5G phone with a metal frame," in 2019 International Workshop on Antenna Technology (iWAT), 2019, pp. 125-128: IEEE.

[62] Kraus, J.D., Marhefka, R.J. and Khan, A.S., 2006. Antennas and wave propagation. Tata McGraw-Hill Education.

[63] Pozar, D.M., 2011. Microwave engineering. John wiley & sons.

[64] Stutzman, W.L. and Thiele, G.A., 2012. Antenna theory and design. John Wiley & Sons.